

ANALYSIS OF THE SWINGS EFFECT AND GREENSTEIN EFFECT IN
COMET P/HALLEY

by
Wayne Anthony Jaworski
B.Sc., University of Manitoba, 1985

A THESIS SUBMITTED IN PARTIAL FULFILLMENT
OF THE REQUIREMENTS FOR THE DEGREE OF

MASTER OF SCIENCE

ACCEPTED
FACULTY OF GRADUATE STUDIES

IN THE DEPARTMENT

OF
PHYSICS

DATE

April 19, 1988

DEAN

We accept this thesis as conforming
to the required standard

Supervisor: Dr. J.B. Tatum

Departmental Member: Dr. F.D.A. Hartwick

Departmental Member: Dr. J. A. Burke

Outside Member: Dr. W.J. Balfour

External Examiner: Dr. K. Dixon

© Wayne Anthony Jaworski, 1988

University of Victoria

February, 1988

All rights reserved. This thesis may not be reproduced
in whole or in part, by mimeograph or other means,
without the written permission of the author.

Supervisor: Dr. Jeremy B. Tatum

ABSTRACT

Spectra have been obtained of Comet P/Halley using the Image Photon Counting System (IPCS) on the Anglo-Australian Telescope in April 1986 by Dr. J.B. Tatum. The CN (0,0) violet system is analyzed to demonstrate the Swings resonance-fluorescence mechanism and multiple spectral images are used in creating a velocity map of the CN gas throughout the coma by application of the Greenstein effect. A new method for solving Abel's equation is developed and tested. This method is applied to a surface density profile of Comet IRAS-Araki-Alcock in order to recover the space density profile through the coma of this comet. The resultant profile is incorporated into theoretical models of the Greenstein effect.

The theoretical calculations of the Swings effect are found to be in good agreement with the observed intensities of the R-branch lines of Comet P/Halley. This validates the assertion of an optically thin coma. In addition, 13 lines interspersed throughout the R-branch are identified as lines belonging to the CN (1,1) band system and the ^{13}CN (0,0) band system. The ^{13}CN (0,0) isotope R(7) and R(8) lines are used to obtain the $^{12}\text{C}/^{13}\text{C}$ ratio in the comet. A value of 88.9 ± 1.8 is found in agreement with the solar value and past determinations with other comets. The Greenstein effect is seen observationally and velocity profiles through the coma are obtained by modeling the R(9)/R(12) ratio of the CN (0,0) band. Changes in radial velocity as large as 1.57 km/s are found to exist within spatial distances of 4,500 km. Theoretical models of the Greenstein effect show that gas jets emanating from the rotating nucleus can account for much of the observed complexity.

EXAMINERS:

[Redacted]

Supervisor: Dr. J.B. Tatum

[Redacted]

Departmental Member: Dr. F.D.A. Hartwick

[Redacted]

Departmental Member: Dr. J. A. Burke

[Redacted]

Outside Member: Dr. W.J. Balfour

[Redacted]

External Examiner: Dr. K. Dixon

TABLE OF CONTENTS

	Page
Abstract	ii
Table of Contents.....	iv
List of Tables	vi
List of Figures	vii
Acknowledgements	ix
Frontispiece.....	x
Chapter 1 Introduction	1
1.1 Background	1
1.2 Current Research	6
Chapter 2 A Solution of Abel's Equation	8
2.1 The Problem	8
2.2 The Solution	14
2.3 Numerical Tests	15
2.4 Application to Comet IRAS-Araki-Alcock (1983 VIII).....	19
Chapter 3 The Observations.....	24
3.1 Requirements	24
3.2 The Equipment Used.....	24
3.3 The Spectra Taken	28
Chapter 4 Reducing the Data	30
4.1 IRAF.....	30
4.2 The Reduction Path Taken	30
Chapter 5 The Cyanogen Molecule.....	38
5.1 Diatomic Molecular Spectroscopy.....	38
5.2 The ($B\ 2\Sigma^+ - X\ 2\Sigma^+$) Violet System of CN.....	45
Chapter 6 The Swings Effect.....	48
6.1 The Resonance-Fluorescence Model	48

6.2	Refinement and Comet Bennett.....	50
6.3	Comet P/Halley.....	55
6.4	Additional Spectral Features Found.....	61
6.5	The $^{12}\text{C}/^{13}\text{C}$ ratio.....	67
Chapter 7	The Greenstein Effect.....	74
7.1	Evidence in Comet P/Halley.....	74
7.2	Velocity Maps of the Coma.....	75
7.3	Modeling: A First Approach.....	84
7.4	Modeling with a Space Density Profile and Cyanogen Jets.....	88
7.5	Addition of a Solar Wind to the Models.....	98
Chapter 8	Summary.....	101
8.1	Present Research.....	101
8.2	Future Research.....	102
References	104
Appendix 1	Solution of the Abelian Integral Equation.....	108
Appendix 2	The Observing Records : Comet IRAS-Araki-Alcock.....	113
Appendix 3	The Observing Records : Comet P/Halley.....	114
Appendix 4	IRAF Routine Descriptions.....	117
Appendix 5	Selected Programs.....	134

LIST OF TABLES

Table	Page
1 Abel Transform Pairs	9
2 R-branch Line Intensities for Comet P/Halley	58
3 Identification of Unknown Lines in the Co-Added Spectrum.....	66
4 The $^{12}\text{C}/^{13}\text{C}$ Ratio : R(7) and R(8) Line Intensities.....	69
5 The Observed Greenstein Effect.....	79

LIST OF FIGURES

Figure	Page
1 Abel Transform Pairs	11
2 Test of the Effect of Noise	17
3 Smoothing and Noise.....	18
4 Surface Brightness Profile	20
5 Surface Density Asymmetry	20
6 Search for a Power Law Fit.....	23
7 Space Density Profile	23
8 Pincushion Distortion.....	27
9 S-Distortion	27
10 The Spectra Taken	29
11 Comparison Arc Spectrum	32
12 Artificial Ceres Spectrum	34
13 The P and R Branches of the CN (0,0) Violet System.....	37
14 An Electronic Band System	39
15 Band Creation.....	39
16 Structure of a Single Band	40
17 The $2\Sigma^+$ State	40
18 Formation of the P and R Branches.....	47
19 The Effect of Different Molecular Constants on the Swings Effect	52
20 The Effect of G on the Swings Effect	52
21 The Swings Effect for Comet Bennett	54
22 The R Branch of Comet P/Halley	56
23 Integrated Intensities versus Line Heights	59
24 The Determination of G	59
25 The Minimum Region.....	60
26 Comet P/Halley Swings Effect	60
27 Radial Velocity Best Fit	62
28 Swings Effect Best Fit	62
29 The Co-Added Spectrum	63
30 The R-Branch Lines of the Co-Added Spectrum	65
31 The Observed Greenstein Effect : R(8)/R(7)	76

32	The Observed Greenstein Effect : R(9)/R(12)	76
33	The Observed Greenstein Effect : R(13)/R(14)	77
34	The Theoretical Greenstein Effect	78
35	East-West Velocity Map of Coma Gas.....	83
36	North-South Velocity Map of Coma Gas	83
37	The Geometry of the Greenstein Models	85
38	Symmetric Radial Gas Flow	87
39	Rigid Rotational Gas Motion	87
40	Addition of a Space Density Profile	90
41	The First Jet Coordinate Map	90
42	Addition of Cyanogen Jets	92
43	Jet Size, Density, and Velocity Effects	92
44	The Second Jet Coordinate Map	94
45	Variable Jet Density and a Preliminary Solar Wind	94
46	The Third Jet Coordinate Map	97
47	An Accurate Integration Model	100
48	Addition of a Solar Wind	100

ACKNOWLEDGEMENTS

I would like to thank my supervisor Dr. Jeremy Tatum for providing me with the observational data on which major portions of this thesis are based and for instruction and guidance during the course of this research. Dr. Tatum asks me in turn to express here his own gratitude to the Director and staff of the Anglo-Australian Observatory for their courtesy and help in obtaining the observations of Halley's Comet with the Anglo-Australian Telescope. Further gratitude must be expressed to all who have provided assistance during the course of my research and to those who have helped in bringing this thesis to print. I am most thankful for the help provided by Chris Pritchett, Timothy Davidge, Polo Infante, and Dave Jaworski.

I would also like to express my gratitude to Dennis Crabtree and Daniel Durand of the Canadian Space Astronomy Data Center for use of their computers and support in reducing the data. Finally, the Natural Science and Engineering Research Council of Canada (N.S.E.R.C.) has made this work possible with financial assistance in the form of a Postgraduate Scholarship.

"I procured me a Triangular glass-Prisme, to try therewith the celebrated Phaenomena of Colours. And in order having darkened my chamber, and made a small hole in my window-shuts, to let in a convenient quantity of the Suns light, I placed my Prisme at his entrance, that it might thereby be refracted to the opposite wall."

Isaac Newton, Phil.Trans.R.Soc., 6, 3075 (1672)

CHAPTER 1 INTRODUCTION

1.1 BACKGROUND

When observable with the naked eye, comets have always attracted the attention of humanity. If observed while the comet is still at a large distance from the sun, only the head or "coma" of a comet can be seen which appears as a circular patch of brightness to the eye or telescope. Now known to consist of volatiles which evaporate from the nucleus of the comet, the coma can extend over half-a-million kilometers in diameter into the surrounding space. As the comet approaches the sun, the steady stream of particles that continually leave the solar atmosphere with velocities of approximately 400 km/s, that is, the solar wind, begins to interact with the gases in the coma leading to the formation of a comet's tail. In fact, comets have two types of tails. The dust tail is composed of dust particles which have been dragged off the nucleus and accelerated by the escaping cometary gases. The solar radiation pressure on these dust particles leads to the development of the dust tail. The ion or gas tail is composed of charged molecules which interact strongly with the charged particles of the solar wind (mainly protons and electrons) to form a tail which always points directly away from the sun (unlike the dust tail). The molecules in the ion tail are also accelerated to much higher speeds than the particles in the dust tail.

With the rapid development of spectroscopy in the 1800's, it was only inevitable that comets would soon be scrutinized much more carefully. The first comet to be observed spectroscopically was Donati's comet of 1858 (Hearnshaw (1986)). The Italian astronomer I. Porro tried to compare its spectrum with that of Arcturus. He was the first astronomer to be caught by the problem of a comet's low intensity of light and his attempt failed. Donati himself later found three bright emission bands in comet I of 1864. In 1868, two much

brighter periodic comets appeared, Brorsen's Comet and Winnecke's Comet, for which Huggins was able to confirm the presence of three bright bands which came from the coma. He showed that these bands corresponded to the same bands observed on burning hydrocarbons in the laboratory. Later, Huggins was the first person to photograph a cometary spectrum (comet 1881b) in which he found ultraviolet bands at 3883 and 3870 Å that he identified with the cyanogen bands already found in the laboratory by Liveing and Dewar. Thus, the $B\ 2\Sigma^+ - X\ 2\Sigma^+$ (0,0) band of the CN radical at 3883 Å, which is of primary importance to this thesis, had been found and identified.

It soon became apparent that this emission was one of the strongest observable features in a cometary spectrum along with the 4050 Å group of C_3 lines and the Swan bands of C_2 . As more comets were observed, the number of detected molecules increased steadily. Most of the observed molecules are free radicals. Non-radicals, that is, stable molecules, have only recently been detected. As they are thought to be the parent molecules of the observed radicals, their detection was of major importance.

As higher resolution has been applied to cometary spectra the rotational structure of several emission bands has been resolved. Under conditions of thermal equilibrium the rotational intensity distribution in an emission band of a heteronuclear diatomic molecule would show a smooth variation passing through a maximum at a value of the rotational quantum number determined by the temperature (Herzberg (1950)). Swings (1941) studied the intensity distribution of the violet (0,0) band of CN using cometary spectra of moderate dispersion and noticed marked irregularities. He interpreted these differences as due to the depletion of the available solar radiation at the wavelengths corresponding to those at which the weakened rotational lines are excited. He was able to obtain a perfect correlation between the weakened cometary lines and the Fraunhofer absorption lines in the solar spectrum, when account was taken of the Doppler shifts caused by the radial component of

the heliocentric velocity of the comet. A striking consequence of this process is the continuous variation of the rotational intensity structure with heliocentric distance as various cometary rotational lines successively pass inside the strong Fraunhofer lines due to varying heliocentric radial velocity. This process is now referred to as the Swings effect.

In addition to the Swings effect, the departure of a comet's coma from thermal equilibrium is also indicated by the widely differing "apparent temperature" of the various radicals estimated on the basis of the position of the maximum intensity of the rotational profile. This suggests that the comet's rotational profile, with exception perhaps of the innermost coma (< 100 km from the nucleus) where collisional excitation may be important, can be explained purely by fluorescent equilibrium. This assumption is further supported by the fact that the characteristic time scale for establishment of this equilibrium (≈ 4 minutes for CN at a heliocentric distance $R \approx 1$ AU (Arpigny (1964))) is much smaller than the time scale for temporal variations due to the motion of the comet.

In 1958, Greenstein (1958) studied the CN (0,0) violet system of Comet Mrkos in order to show that the Swings fluorescence mechanism could indeed explain the band structure of a comet. As well as confirming in full detail that the Swings effect mutilated the intensity distribution of the completely resolved R-branch, he also found a new second-order effect. Greenstein discovered that the intensity ratios between individual rotational cyanogen lines ($R(10)/R(9)$) changed within 4000 km on opposite sides of the nucleus. He attributed these changes to motions, dominantly radial with respect to the sun, within the coma of the comet which will cause additional heliocentric radial shifts above that of the comet. For Comet Mrkos, Greenstein found that motions of the order of 3 km/s were required in order to reproduce the observed effect. This second-order Swings effect is now called the Greenstein effect. Since the internal velocities of the radicals are typically ≈ 1 km/s, this effect is necessarily very small, but it provides us in principle with a

method of deconvoluting the internal velocity profile of a given species from the observations.

With the growing availability of electronic computers, the Swings effect was soon tested extensively through increasingly sophisticated computer models of pure fluorescent equilibrium. The models usually solve a system of equations where each equation represents the balance between both fluorescent excitations and de-excitations as well as pure rotational de-excitations for each rotational level in the molecule. The number of rotational levels involved in the model depends upon the number of R-branch lines whose relative intensities are to be predicted. In addition, the existence of the Fraunhofer lines in the exciting solar spectrum are taken into account, as well as their Doppler shifts due to the comet's radial motion, through the use of high-resolution digital solar spectra. This method has been applied to numerous comets and has succeeded very well in reproducing the observed Swings effect. The equations governing fluorescent equilibrium were first given in detail by Arpigny (1964). Prior to this work, it was customary for investigators to make the convenient assumption that the distribution of populations of the rotational levels in the ground state of the molecule considered followed a Boltzmann law at some chosen "temperature". The authors of these investigations realized that they had no justification for making this assumption since the agents that would tend to produce a Boltzmann distribution are lacking due to the fact that collisions are so infrequent in a cometary atmosphere (except perhaps very close to the nucleus). Aikman et al (1974) recast the equations of Arpigny (1964) using a different notation and different molecular constants. They found good agreement between the predicted R-branch line intensities for the CN (0,0) violet band and those they observed in Comet Bennett. It should be noted however that the first seven lines of the observed R-branch, lines R(0) through R(6), were clearly in discrepancy with their predicted intensities. Arpigny's formulation of pure fluorescent

equilibrium was used by Ishii and Tamura (1979) in the study of Comet Kohoutek. They found that the predicted relative intensity distribution of the CN (0,0) violet band agreed well with the observations (which were of lower resolution than those of Aikman et al (1974)). They also observed the Greenstein effect and put an upper limit on the internal CN motion of $\pm (4 \sim 5)$ km/s.

The effect of collisions on the observed spectra were taken into account by Malaise (1970) who computed a synthetic spectrum of the (0,0) violet band of CN at different distances from the nucleus. Besides fluorescent equilibrium, he included the effects of collisions in exciting rotational levels of the ground state. Although he found excellent agreement between theory and observations of Comet Ikeya, Malaise derived total coma densities many orders of magnitude larger than the commonly accepted values. Arpigny (1976) has pointed out that much of the effect seen by Malaise can be understood without collisions by using different values for many atomic parameters, in particular a larger oscillator strength for pure rotational transitions within the ground state. It has recently been shown that collisions do not play any role in the case of the CN radical because most of them fluoresce outside the collision sphere (Arpigny (1976); Festou (1981)). It thus seems that most aspects of the rotational structure of the CN spectrum can be understood by pure fluorescence.

The transitions observable in cometary spectra only involve the three lowest electronic states of CN: $X^2\Sigma^+$, $A^2\Pi_1$, and $B^2\Sigma^+$. The most recent advancement in modeling the Swings effect is to include not only the B - X (0,0) band of CN when computing the equilibrium established by pure fluorescence, but also the red A - X system. (The B - A system has never been observed in comets due to its very small branching ratio). In effect this introduces two more free parameters over the previous models. Zucconi and Festou (1985) have pioneered this approach. Although in general their models do not fit the data

better than those of Arpigny (1964) and Aikman et al (1974), there is one exception to this. The first seven R-branch lines, R(0) through R(6), are now much better modeled than previously. Schleicher (1983) had predicted this result noting that the primary effect of additional fluorescent channels would be to smooth out the ground state populations, resulting in a general smoothing of the rotational line intensities. He also noted however that this equalizing of the populations would occur only among the even values of N (the total angular momentum quantum number excluding spin) or the odd values, but not between these because of parity conservation. (Any two-step transition will result in the same parity as existed initially). For small values of N', the results of Aikman et al (1974) show that the calculated intensities for the odd values of N' are all too small, while the even valued lines are too large. Thus three-step transitions are needed to equalize the populations between the two parity states.

1.2 CURRENT RESEARCH

The current research is an extension of the application of both the Swings effect and Greenstein effect to new data of superior quality obtained with the Anglo-Australian Telescope (AAT) in 1986. The very high resolution data obtained of the CN (0,0) violet band system ($0.032 \text{ \AA}/\text{pixel}$) in the coma of Comet P/Halley and the multiple spectra taken enabled a much more involved study of the Greenstein effect in particular than had ever been done previously. The effect of different coma velocity profiles on the Greenstein effect was also modeled for the first time. The other purpose of this research was to examine the Swings effect in Comet P/Halley using better molecular constants and a new full-disk solar spectrum compared with the previous models of Aikman, Balfour, and Tatum (1974). The $^{12}\text{C}/^{13}\text{C}$ isotope ratio was also obtained directly from observations of both the ^{12}CN (0,0) and ^{13}CN (0,0) violet systems.

In Chapter 2 a new solution of Abel's equation is developed and extensively tested. This solution is applied to a surface brightness profile of Comet IRAS-Araki-Alcock in order to produce an estimation of the density profile of CN gas through the coma of a comet. This density profile is later used in Chapter 7 to model the Greenstein effect.

In Chapter 3 the observations of Comet P/Halley taken with the AAT are discussed. The equipment used in obtaining the data are also fully described so that the procedure used to reduce the data can be understood.

Chapter 4 deals with the reduction of the raw AAT data. The IRAF software package used is reviewed and the complete path taken to reduce the data is put forth. Possible sources of error are also investigated.

Chapter 5 provides some background molecular spectroscopy pertaining to the cyanogen molecule so that concepts relating to the rest of the thesis can be better understood. The violet (0,0) system of CN is investigated in particular.

The Swings effect is discussed in Chapter 6. The effect of a new full-disk solar atlas and the use of new molecular constants on the predicted Swings effect is examined for Comet Bennett and the previous study by Aikman et al (1974). The Swings effect is then modeled and compared with the new observations of Comet P/Halley. In addition, 13 spectral lines that are found to be present among the ^{12}CN (0,0) violet band lines are identified. This results in the determination of the $^{12}\text{C}/^{13}\text{C}$ ratio in the comet.

The Greenstein effect is the focus of Chapter 7. Multiple spectral images of the CN (0,0) violet band are used to obtain a velocity profile of the cyanogen gas in the coma of Comet P/Halley. In addition, the effect of varying velocity profiles in the coma of a comet on the observed Greenstein effect are modeled. The results of the models are used to better interpret the conditions present inside the coma of P/Halley at the time of the observations.

Finally, we summarize our results in Chapter 8.

CHAPTER 2 A SOLUTION OF ABEL'S EQUATION

2.1 THE PROBLEM

We imagine a plasma of cylindrical symmetry and radius a . Let r be the distance of a point from the axis of the cylinder, and $\rho = r/a$, and let $n(\rho)$ be the number density of particles there. Let us suppose that we examine this plasma with a spectroscope whose slit is to one side of the cylinder and at right angles to the axis. Let y be the distance of a point on the slit from its mid-point, and $\eta = y/a$. We suppose we can measure the intensity of a spectrum line at this point and that, if the plasma is optically thin, we can calculate the column density (number of emitting molecules per unit area in the line of sight through the plasma) $N(\eta)$. Then, with $\xi^2 = \rho^2 - \eta^2$, ξ being the coordinate in the line of sight perpendicular to the cylinder axis and to the slit, it is easy to show that

$$N(\eta) = 2a \int_0^{\sqrt{1-\eta^2}} n(\rho) d\xi = 2a \int_{\eta}^1 \frac{n(\rho)\rho d\rho}{(\rho^2 - \eta^2)^{1/2}}. \quad (1)$$

This is a form of Abel's equation. A few simple analytical examples of Abel transform pairs $(N(\eta), n(\rho))$ are given in Table 1, illustrated in Figure 1. If $n(\rho)$ is known, $N(\eta)$ is found by straightforward integration. The situation most likely encountered in practice, however, is the converse problem: $N(\eta)$ is known from measurement, and $n(\rho)$ is to be deduced.

Table 1. Abel Transform Pairs

$n(\rho)$	$N(\eta)$	Notes
1. n_0	$N(0)\xi,$	$N(0) = 2an_0$ a, b
2. $n(0)(1 - \rho)$	$N(0)\left[\xi - \eta^2 \ln\left(\frac{1 + \xi}{\eta}\right)\right],$	$N(0) = an(0)$ b
3. $n(0)(1 - \rho^2)$	$N(0)\xi^3,$	$N(0) = \frac{4}{3}an(0)$ b
4. $n(0)(1 - \rho^2)^{1/2}$	$N(0)\xi^2,$	$N(0) = \frac{\pi}{2}an(0)$ b
5. $n(1)/\rho$	$2an(1)\ln\left(\frac{1 + \xi}{\eta}\right)$	b, c
6. $n(1)/\rho^2$	$2an(1)\frac{\cos^{-1}\eta}{\eta}$	c
7. $n(1)/\rho^3$	$2an(1)\frac{\xi}{\eta^2}$	b, c
8. $n(0)e^{-\rho/\rho_0}$	$N(0)\frac{\eta}{\rho_0}K_1\left(\frac{\eta}{\rho_0}\right),$	$N(0) = 2a\rho_0n(0)$ d, e
9. $n(0)e^{-\rho^2/(2\rho_0^2)}$	$N(0)e^{-\eta^2/(2\rho_0^2)},$	$N(0) = \sqrt{2\pi}a\rho_0n(0)$ d
10. $\rho_0n(\rho_0)\frac{e^{1 - \rho/\rho_0}}{\rho}$	$2a\rho_0n(\rho_0)eK_0\left(\frac{\eta}{\rho_0}\right)$	d, e
11. $n(\rho_m)\left(\frac{\rho}{\rho_m}\right)^2 e^{1 - (\rho/\rho_m)^2}$	$N(\eta_m)\left(\frac{\eta_m^2 + \eta^2}{2\eta_m^2}\right)e^{\frac{\eta_m^2 - \eta^2}{2\eta_m^2}},$ $N(\eta_m) = \sqrt{2\pi}e a\eta_m n(\rho_m)$	d, f, g
12. $kn(\rho_m)(e^{-\rho/\rho_1} - e^{-\rho/\rho_2})$	$2ak\rho_1n(\rho_m)\frac{\eta}{\rho_1}\left[K_1\left(\frac{\eta}{\rho_1}\right) - K_1\left(\frac{\eta}{\rho_2}\right)\right]$	d, e, f, h
13. $n(\rho_m)\frac{\rho}{\rho_m} e^{1 - \rho/\rho_m}$	$2ae\rho_m n(\rho_m)\frac{\eta}{\rho_m}\left[K_1\left(\frac{\eta}{\rho_m}\right) + \frac{\eta}{\rho_m}K_0\left(\frac{\eta}{\rho_m}\right)\right]$	d, e, f

Table 1. (continued)

Notes

- a. The plasma is of uniform density n_0 throughout the cylinder.
- b. $\xi = (1 - \eta^2)^{1/2}$
- c. $0 < \rho \leq 1$. $n(0)$ and $N(0)$ are infinite. $n(\rho)$ is assumed to be truncated at $\rho = 1$, i.e., $n(\rho) = 0$ for $\rho > 1$. $n(1)$ is the density at the surface of the cylinder.
- d. $\rho_0, \rho_1, \rho_2, \rho_m$ are (constant) scale factors. The functions $n(\rho)$ extend to infinity and the Abel transform pairs are exact only if the upper limit of integration is ∞ . However, to a good approximation, the integration can be terminated at a finite $r = a$, i.e., $\rho = 1$, provided these scale factors are small compared with unity.
- e. K_ν is the modified Bessel function of the third kind of order ν .
- f. ρ_m is the value of ρ at which $n(\rho)$ is a maximum.
- g. η_m is the value of η at which $N(\eta)$ is a maximum, and is given by $\eta_m = \rho_m/\sqrt{2}$.
- h. ρ_1 and ρ_2 are two independent scale factors with $\rho_1 > \rho_2$, and $\rho_1/\rho_2 = c > 1$. k and ρ_m are functions of ρ_1 and ρ_2 :

$$k = \frac{c(c/(c-1))}{c-1}, \quad \rho_m = \frac{\rho_1 \ln(c)}{c-1}.$$

With these definitions, $n(\rho_m)$ is the maximum value of $n(\rho)$, occurring at $\rho = \rho_m$. The graphs in Figures 1 and 2 are drawn for the particular case $c = 2$.

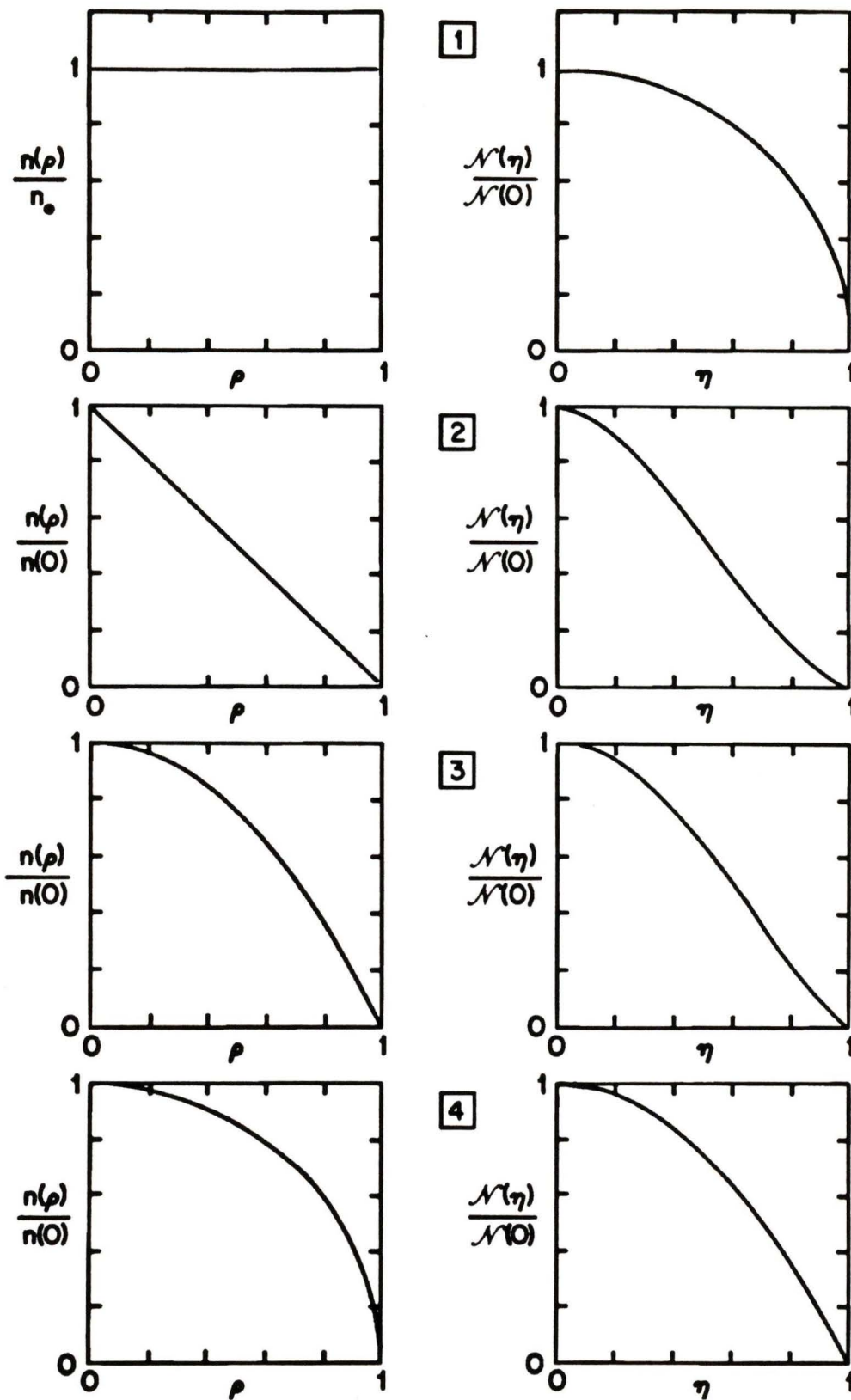


Figure 1 Abel Transform Pairs. The numbers in the small squares correspond to the numbers in the first column of Table 1.

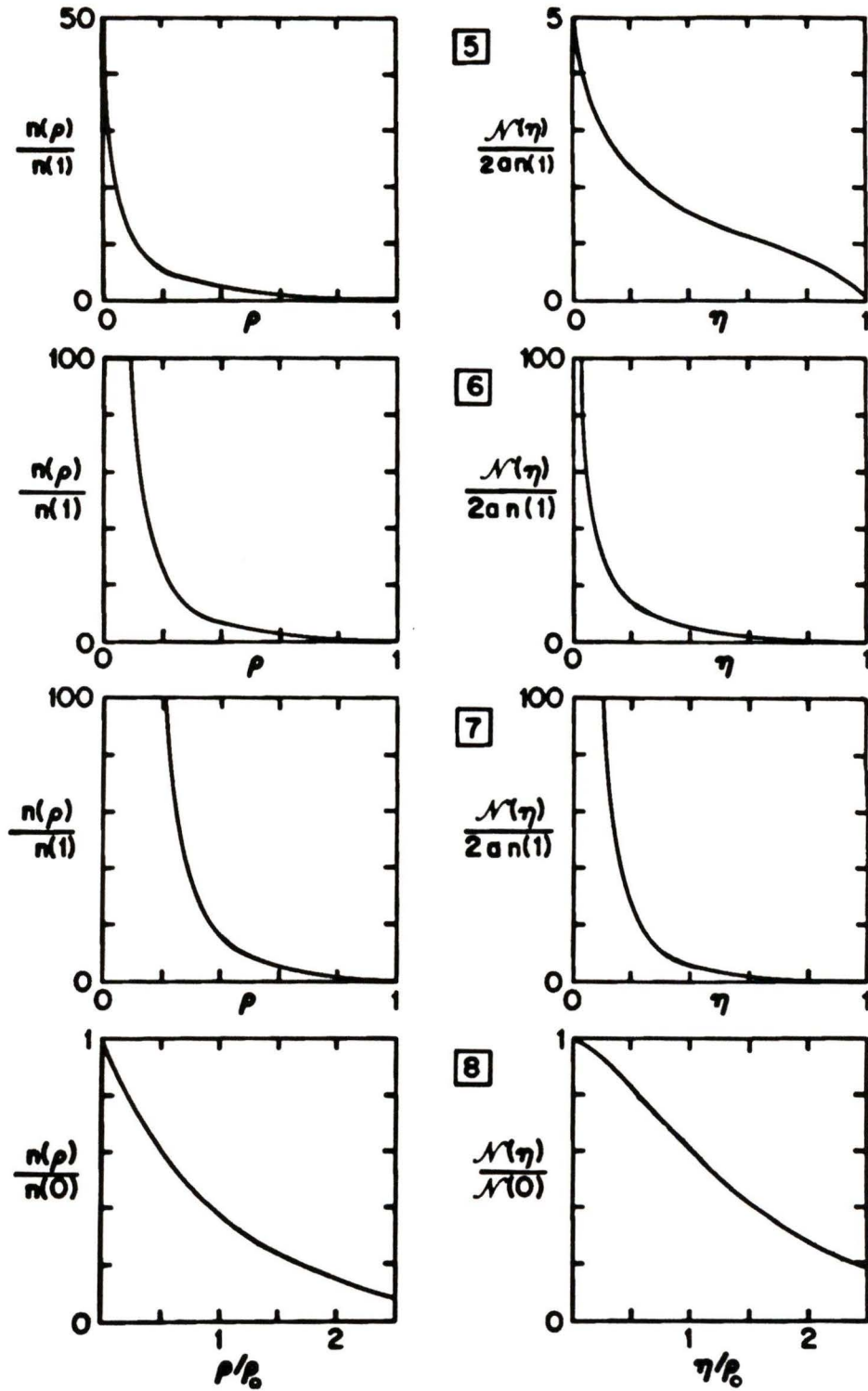


Figure 1 (continued) Abel Transform Pairs.

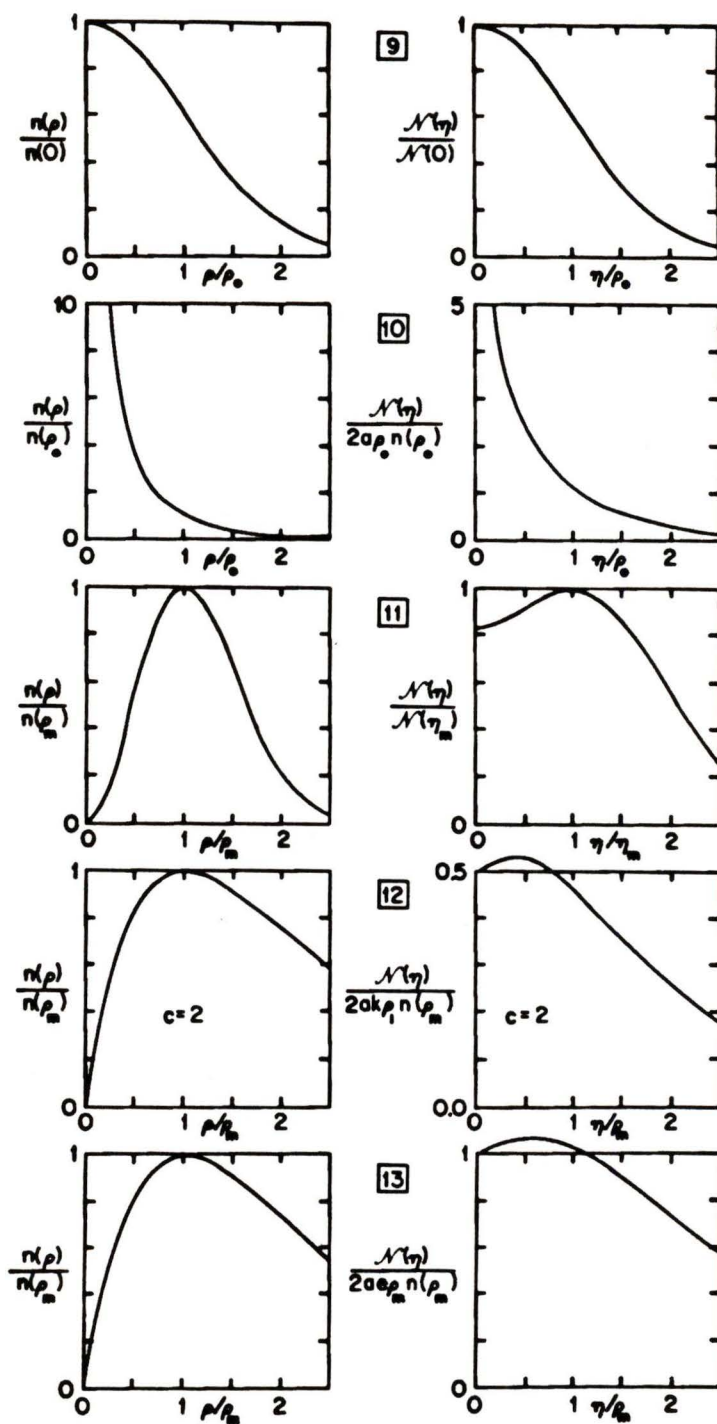


Figure 1 (concluded) Abel Transform Pairs.

2.2 THE SOLUTION

Many solutions have been proposed to this problem. Examples include those of Bockasten (1961), Barr (1962), Herlitz (1963), Paquette and Wiese (1964), and Shumaker and Yokley (1964). Some of these employ special mathematical functions that were in vogue before the days of high-speed electronic computers and are of less use today than heretofore. The solution we offer, which we have not seen given elsewhere and which seems to be fast, accurate and easy to program, is

$$n(\rho) = -\frac{1}{\pi a \rho} \frac{d}{d\rho} \left\{ (1 - \rho^2)^{1/2} \int_0^{\pi/2} N[(1 - (1 - \rho^2)\sin^2\theta)^{1/2}] \sin\theta d\theta \right\}. \quad (2)$$

Here θ is a dummy variable and N is to be evaluated for arguments given by $(1 - (1 - \rho^2)\sin^2\theta)^{1/2}$. The solution can be verified by verifying the transform pairs of Table 1 using Equations (1) and (2). A detailed proof is given in Appendix 1.

In programming Equation (2), we have usually performed the integration with respect to θ with a 200-step Simpson's rule, with interval $\pi/400$. For differentiation with respect to ρ , we have usually calculated the quantity in braces [= $P(\rho)$] from $\rho = 0$ to $\rho = 1$ at intervals $\delta\rho = 0.005$ and evaluated the derivative from

$$P'(\rho) = \frac{1}{12\delta\rho} [P_{-2} - P_2 + 8(P_1 - P_{-1})], \quad (3)$$

where $P_v = P(\rho + v\delta\rho)$. For the analytical transform pairs of Table 1 we have found that this usually gives 7- to 10-figure accuracy in a few seconds of computing time on an IBM 370 mainframe computer using double precision real variables. We have further tested the

method by setting up some arbitrary sets of hypothetical numerical values of $n(\rho)$, integrating by Equation (1) to determine $N(\eta)$ and then recovering $n(\rho)$ from Equation (2). More importantly, we have added varying amounts of random noise to $N(\eta)$ to determine how badly $n(\rho)$ is degraded by such noise. The results of these tests will now be examined in detail.

2.3 NUMERICAL TESTS

In order to verify the accuracy, and hence usefulness, of Equation (2), it was necessary to test each step of the numerical calculations under a wide variety of input parameters. The Abel transform pairs of Table 1 were chosen in order to achieve this, rather than from a conviction that they represent realistic data for a real comet. The numerical integration routine, which used Simpson's 1/3 rule, was tested first. This routine requires a table of $n(\rho)$ values as input which are then integrated by Equation (1) to produce a table of $N(\eta)$ values which can be compared with the exact analytical result. A Newton-Gregory interpolating polynomial of degree up to nine is constructed to return required function values from the table. It is found that the highest accuracy is achieved when a ninth degree interpolating polynomial is used. All of the 13 function pairs of Table 1 were used to test the integration routine. In every case, 10-decimal place accuracy was obtained.

The next step, again applied to every transform pair, was to generate a table of exact $n(\rho)$ values for a given function, integrate by Equation (1) to determine $N(\eta)$ and then try to recover $n(\rho)$ from Equation (2). As mentioned earlier, this resulted in 7- to 10-decimal place accuracy. The last step was to test the effect of varying amounts of random noise in $N(\eta)$ on the ability of Equation (2) to recover the $n(\rho)$ values. This is perhaps the most

important criterion since all real data contain noise to some extent. The NAG Fortran library routine 'G05CAF' was used to generate the random numbers.

As is often the case with integral transforms, the calculated $n(\rho)$ is very sensitive to noise in the measured $N(\eta)$. Figure 2 shows the result of adding 5% maximum random noise to the $N(\eta)$ values of transform pair #12 and then applying Equation (2). Even though the noise is amplified through the integral transform process it should be noted that the turnoff at small ρ/ρ_m is still followed correctly. As can be appreciated from Figure 1, many different functions $n(\rho)$ give rise, when integrated, to rather similar functions $N(\eta)$. In light of this, we have used the first analytical transform pair of Table 1 to further test the degree of sensitivity since it represents a worst case scenario in that one would expect the values of $n(\rho)$ to decrease as ρ increases when the noise level becomes unacceptable. In order to obtain better results, it was necessary to first apply a simple smoothing algorithm to the $N(\eta)$ data. The algorithm used the mean of the data points within a specified box size as the value at the midpoint of the box. The smoothing algorithm itself was tested in order to insure that it did not introduce any errors into the whole procedure. It was found, by smoothing the exact $n(\rho)$ function for transform pair #1, that a slight artifact affecting only the last few points at large ρ values was being introduced by the process. The Abelian integral transform was then applied to the smoothed data and compared with the exact $n(\rho)$ function used and the case with no noise added to the $N(\eta)$ data. Figure 3 shows the results of adding 5% maximum random noise to the $N(\eta)$ data (transform pair #1) and then applying the smoothing and Abelian transform algorithms. It can be seen that 95.7% of the data lie within the 20% noise level and 78.7% of the data are within the 10% noise level. We believe that our solution to Abel's equation is robust up to a 5% noise level in the data as long as a simple smoothing algorithm is first applied.

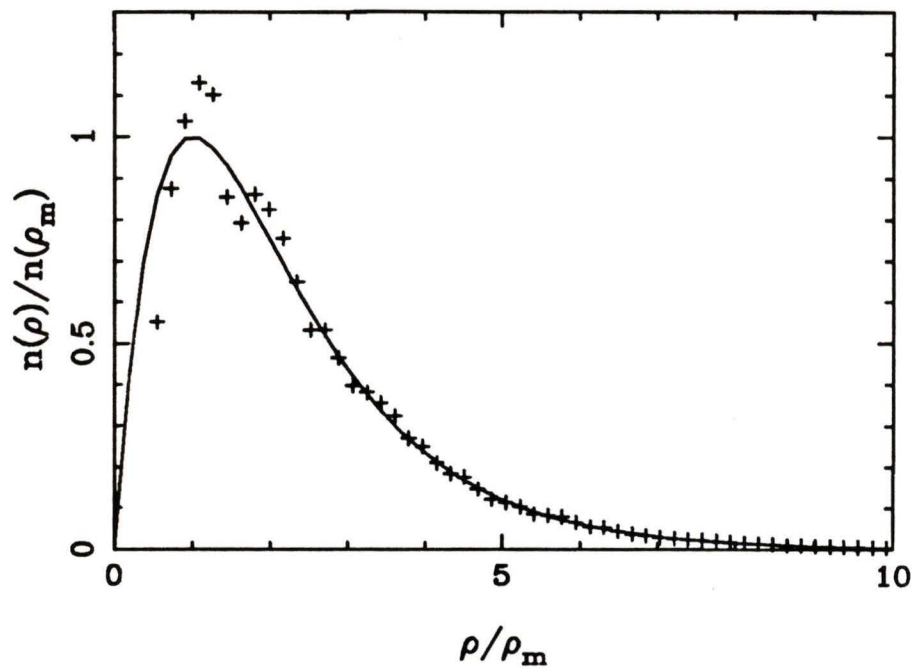


Figure 2 Test of the Effect of Noise. Noise at the 5% level was added to the $N(\eta)$ values of the twelfth transform pair of Table 1 and Figure 1. Equation (2) was then used to try to recover $n(\rho)$. The exact function is represented by the solid line.

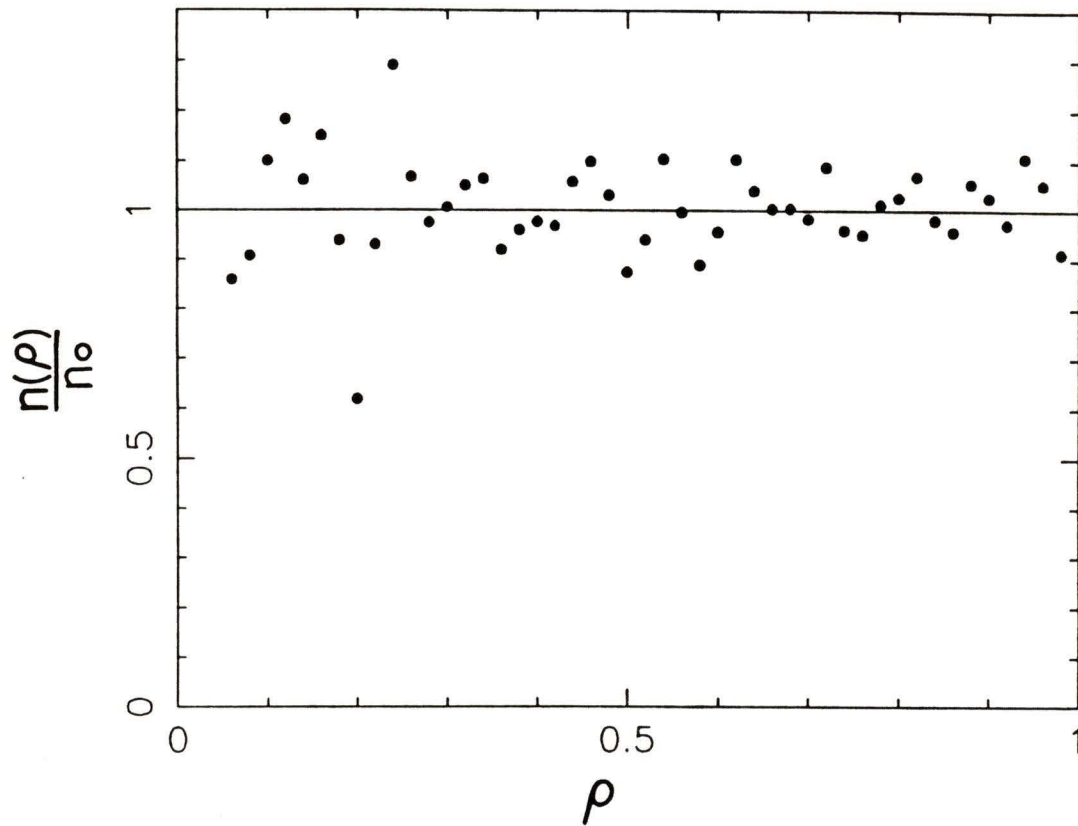


Figure 3 Smoothing and Noise. Noise at the 5% level was added to the $N(\eta)$ values of the first function-pair of Table 1 and Figure 1 and smoothed. Equation (2) was then used to try to recover $n(\rho)$, which should be a horizontal straight line. Of the 14 function-pairs, this one is the worst.

2.4 APPLICATION TO COMET IRAS-ARAKI-ALCOCK (1983 VIII)

In order to model the Greenstein effect as part of the current research, a realistic profile of the density of CN gas through the coma of a comet would be needed. To this end, fully reduced images of Comet IRAS-Araki-Alcock (1983 VIII) taken by Pritchett and Infante on May 8, 1983 were made available to the author for use. The image chosen was taken with a U filter as the CN (0,0) violet system ($B^2\Sigma^+ - X^2\Sigma^+$) is found within this filter's bandpass. Details of the observation can be found in Appendix 2. The data-reduction program R2D2, written by Dr. Chris Pritchett at the University of Victoria, was used in order to extract a surface brightness profile across the coma of the comet. This was accomplished by performing the *Y CUT* command perpendicular to an apparent axis of cylindrical symmetry in the coma such that the comet's nucleus was included in the profile. Figure 4 shows the results of this operation.

As can be seen in Figure 4, the peak of the surface density profile is located at pixel number 290 which also corresponds to the nucleus of the comet. The data were divided about this point into two halves, a north and south profile, and the south profile was mirrored about the nuclear axis so that the two profiles could be compared. In addition, the scale of distance through the coma was normalized to units of a while preserving the overall scale of the surface density profile. The north and south profiles were then smoothed using the algorithm described earlier with a box size of 0.02. The resultant profiles are depicted in Figure 5.

From Figure 5 it is clear that the north and south surface density profiles are asymmetric. This is consistent with observations by Festou et. al. (1987) who also report a strong asymmetry in the coma reflecting the anisotropic production of matter by the nucleus. They infer that the unlit side of the nucleus was outgassing at a rate one third that of the lit side at the time of their observations on May 13, 1983.

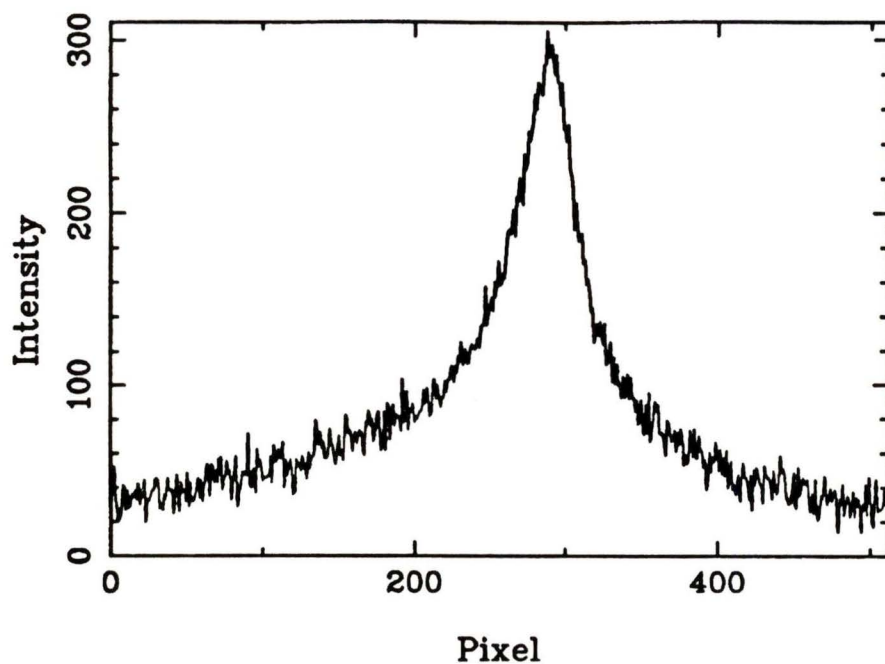


Figure 4 Surface Brightness Profile. The data reduction program R2D2 was used to obtain a surface brightness profile of Comet IRAS-Araki-Alcock along an axis of cylindrical symmetry through the nucleus.

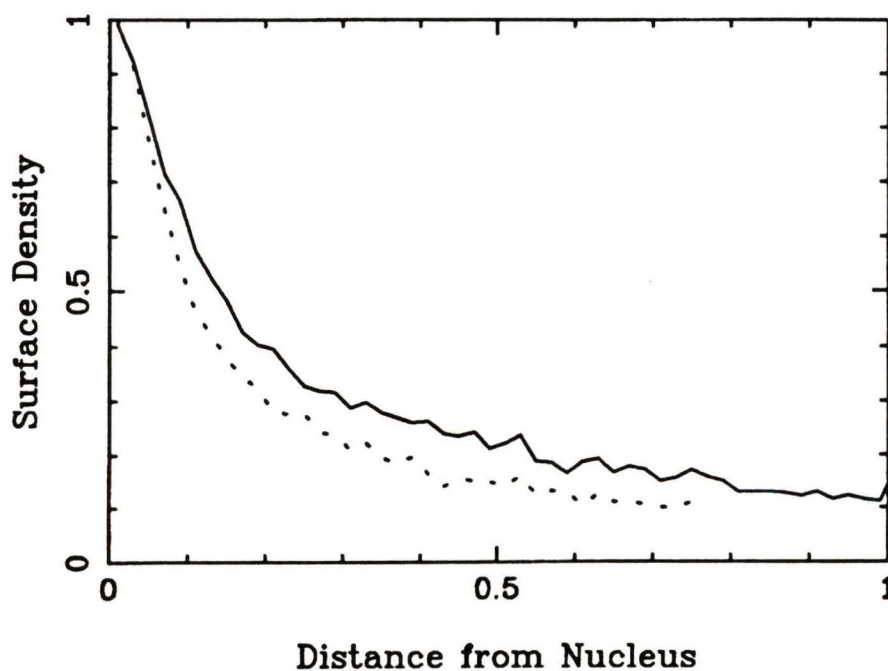


Figure 5 Surface Density Asymmetry. The data of Figure 4 were normalized to units of a , smoothed, and reflected about the comet's nucleus to show the asymmetry in the surface density profiles on each side of the nucleus. The solid line represents the data south of the nucleus and the dotted line shows the northern data.

The Abelian integral transform, Equation 2, was used in order to recover the space density profiles using the data of Figure 5. From visual inspection, it was clear that the resulting graph of $n(\rho)$ versus ρ resembled the Abel transform pairs 5 and 6 of Figure 1. This suggested that a power law relationship could be used to fit the data. Figure 6 is a log-log plot of $n(\rho)$ versus ρ used to find the slope of this power law. From a least-squares linear fit of the combined north and south data sets, a slope of -1.456 was obtained with an R^2 value of 90.6% (i.e. 90.6% of the variability in $\ln n(\rho)$ is explained by linear regression). The space density relationship found is thus

$$n(\rho) = \frac{0.045}{\rho^{1.456}}$$

Finally, it will be of use to convert ρ from units of a ($0 < \rho \leq 1$) to units of kilometers. At the time of observation (May 8.4569, 1983) Balam (1987) gives the following orbital parameters

$$R \text{ (AU)} = 1.014, \quad \dot{R} \text{ (km/s)} = -6.182, \quad \text{and} \quad \Delta \text{ (AU)} = 0.073.$$

One pixel of the CCD used corresponds to $0''.86$ of sky covered. Therefore, 289 pixels, $\rho = 1$, corresponds to an angle of $248''.54$ or 1.205×10^{-3} radians. So, $\rho = 1$ ($=a$) corresponds to a distance at the comet of

$$s = r \theta = (0.073 \text{ AU})(1.205 \times 10^{-3} \text{ radians}) = 8.750 \times 10^{-5} \text{ AU}.$$

But since $1 \text{ AU} = 1.496 \times 10^8 \text{ km}$, this is equivalent to 13,089 km.

Putting all of this together yields the space density relationship

$$n(\rho) = \frac{44,407}{\rho^{1.456}}$$

where ρ now has units of kilometers and $n(\rho)$ is scaled to match the observed density profiles. Figure 7 illustrates this relationship between the function fit and the observed north and south space density profiles. As mentioned earlier, this function will be used in Chapter 6 to determine the effect of adding a space density profile of CN gas on the Greenstein effect.

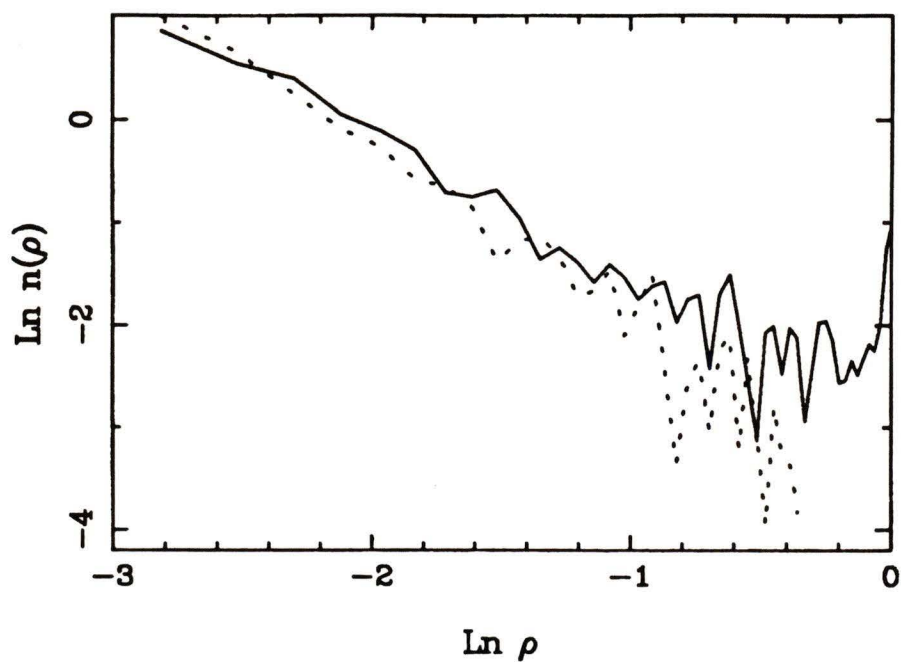


Figure 6 Search for a Power Law Fit. The data of Figure 5 were transformed using Equation (2) and then the natural logarithm of the northern (dotted line) and southern (solid line) data plotted to determine if a power law relationship exists between $n(\rho)$ and ρ .

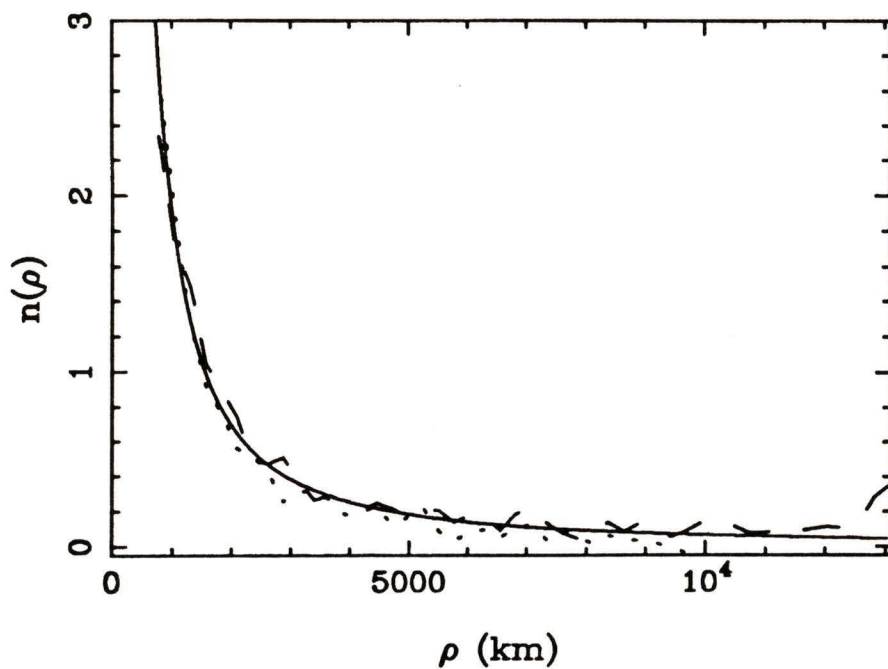


Figure 7 Space Density Profile. The function found from the power law relationship illustrated in Figure 6 is shown (solid line) along with the north (dotted line) and south (dashed line) data observed in Comet IRAS-Araki-Alcock.

CHAPTER 3 THE OBSERVATIONS

3.1 REQUIREMENTS

The 1986 apparition of Comet P/Halley was to be one of the worst on record for observers located in the northern hemisphere. Near perihelion, the comet would be far south of the ecliptic and thus only available to telescopes in the southern hemisphere. For this reason, the Anglo-Australian Observatory located on Mount Woorut, also called Siding Spring Mountain, in New South Wales, Australia, was chosen as the observing site. The observatory is located at a latitude of $-31^{\circ} 16' 37''.34$. In order to study the Greenstein effect with sufficient detail and resolution, several long-slit spectra positioned across the coma of the comet would be needed. In addition, each spectrum would have to be of high enough resolution so that the R-form branch lines of the CN (0,0) violet system (B $2\Sigma^+$ - X $2\Sigma^+$) located at 388.3 nm are completely resolved. The AAT Image Photon Counting System (IPCS hereafter) in conjunction with the RGO spectrograph and 82 cm camera fulfilled all of these requirements. This equipment, which was used to obtain the observational data on which the main body of this thesis deals with, will now be examined in detail so that the reduction path followed can be better understood.

3.2 THE EQUIPMENT USED

The Anglo-Australian Telescope (AAT) has a 3.9 meter primary mirror and a focal length of 12.7 meters, resulting in a focal ratio of about $f/3.3$ at prime focus. In addition to prime focus, three other basic optical configurations are possible including two Cassegrain configurations with focal ratios of $f/8$ and $f/15$ and a Coudé focus at $f/36$.

The RGO spectrograph, designed and built by the Royal Greenwich Observatory, mounts at the $f/8$ focus of the AAT where the scale is 6.7 arcsec/mm. It is possible to mount one of two cameras on the spectrograph - an 82 cm focal length $f/5.5$ spherical mirror and a 25 cm $f/1.67$ Cassegrain-Maksutov system. The 82 cm camera was used as it provides the highest resolution. With the 1200J grating used on the spectrograph in our case, a dispersion of $10 \text{ \AA}/\text{mm}$ is obtained.

The IPCS is the principal detector used with the RGO spectrograph. The IPCS detects individual photon events in a two-dimensional image by means of a high-gain 4-stage Image Intensifier (S20 photocathode) optically coupled to a continuously scanning television camera (Philips Plumbicon), and then records their central positions in a 512 k-pixel digital electronic memory. An important feature of the system is the event-centre-detection (ECD) logic which identifies the centroid of each photon event, despite the degradations imposed by the electron optics, providing a large increase in spatial resolution over that obtained by conventional analogue recording. The spectral resolution is determined by setting the number of frame lines of the Plumbicon camera. Highest resolution is obtained with 2048 lines covering 30 mm on the first cathode of the image tube. The number of picture elements (pixels) along the slit is controlled by setting the number of line increments of the Plumbicon. A choice from 18 to 514 is available. The spatial resolution of each increment is given by the value of the X-gain, which can be set to either "high" or "low", corresponding to an incremental separation of 140 and 70 μm , respectively.

The faceplate of the IPCS suffers from both pincushion distortion and s-distortion. Figure 8 depicts the appearance of the faceplate imaging a hypothetical emission-line long-slit spectrum. The curvature of the spectral lines (i.e. the pincushion distortion) is easily seen. The s-distortion would show up better with a continuum source and a short slit (or

equivalently a point source such as a star illuminating only part of the long slit). Figure 9 shows the resulting s-distortion exaggerated so that it is plainly visible. Of course if you look at an extended source, such as a comet, the whole faceplate is illuminated and it is difficult to trace out the s-distortion (whereas in Figure 9, it is clear that the spectrum at "P" belongs to the spectrum at "Q").

The s-distortion inherent in the detector system is handled by the IPCS through electronically delaying the start of data taking in each scan line. The faceplate is imaged onto an x-y TV camera so that the photon events can be spatially recorded as mentioned above. The delays lead to the rows of pixels being shifted so that the spectrum is made straight. The curvature or pincushion distortion is usually corrected for after the data are taken by using a comparison spectrum of an arc lamp and re-mapping the spectrum so that several wavelength calibrated arc lines are made straight perpendicular to the dispersion.

Because of structure in the response of the image tube and television target, each pixel of the IPCS has a slightly different sensitivity. This is referred to as the granularity of the detector. Without correction, the pixel-to-pixel variations in sensitivity are about 3 per cent rms over large scales (Jenkins (1987)). This granularity can be corrected for in principle by obtaining a flat-field exposure and dividing it into the data. Jenkins (1987) finds that the small-scale structure of the granularity matters much less as it carries little power compared with the large-scale granularity. He also finds an appreciable non-linearity in the IPCS detector, due to coincidence losses, which becomes obvious above count rates of a few tenths of Hz pixel⁻¹ as well as correlated photon noise between adjacent pixels at high count rates (≥ 0.5 Hz pixel⁻¹). As a result, the statistics of the data obtained with an IPCS are very complicated at all but the lowest count rates.

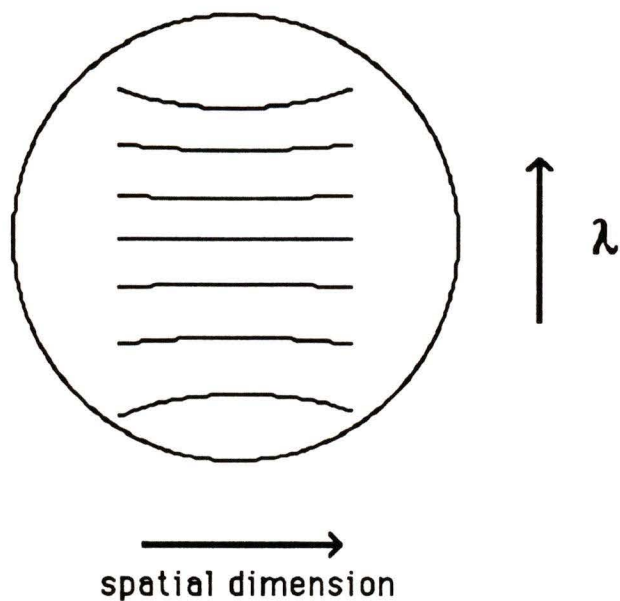


Figure 8 Pincushion Distortion. The effect of pincushion distortion on a hypothetical emission line spectrum is depicted as it would appear on the IPCS faceplate. (The amount of curvature is exaggerated).

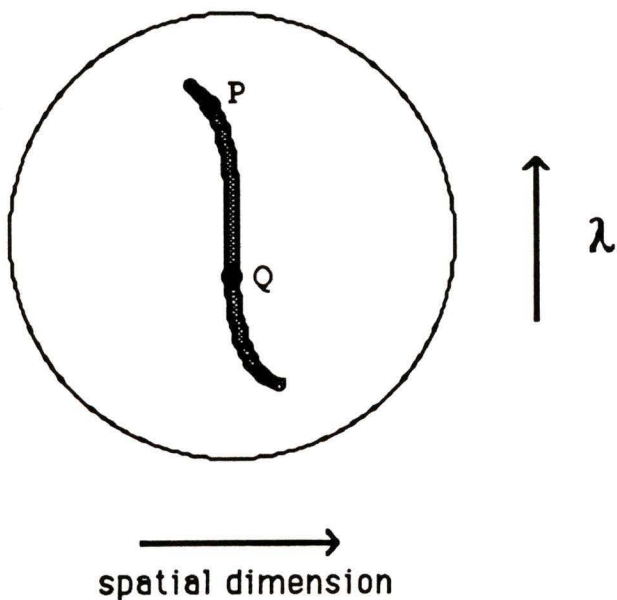


Figure 9 S-Distortion. The effect of s-distortion, occurring on the IPCS faceplate, on a spectrum. The points labelled "P" and "Q" belong to the same spectrum but are displaced spatially due to the distortion. (The magnitude of the s-distortion is greatly exaggerated).

3.3 THE SPECTRA TAKEN

In April of 1986, Dr. J.B. Tatum observed the coma of Comet P/Halley with the equipment described above. Figure 10 illustrates the positions of the 13 long-slit spectra taken with respect to the coma of the comet. The position angle of the slit was 90 degrees and each spectrum was 220 by 2040 pixels in size. The details of the observing run can be found in Appendix 3. With the configuration of equipment used, 1 pixel corresponds to 1".4 of sky in the spatial or slit direction. As the observing log (Appendix 3) and Figure 10 show, each spectrum is separated by 4 minutes of arc from its neighboring spectra. In addition to the 13 spectra of the CN (0,0) violet band system of the comet, 3 copper-argon comparison arcs were taken as well as the spectrum of the asteroid Ceres.

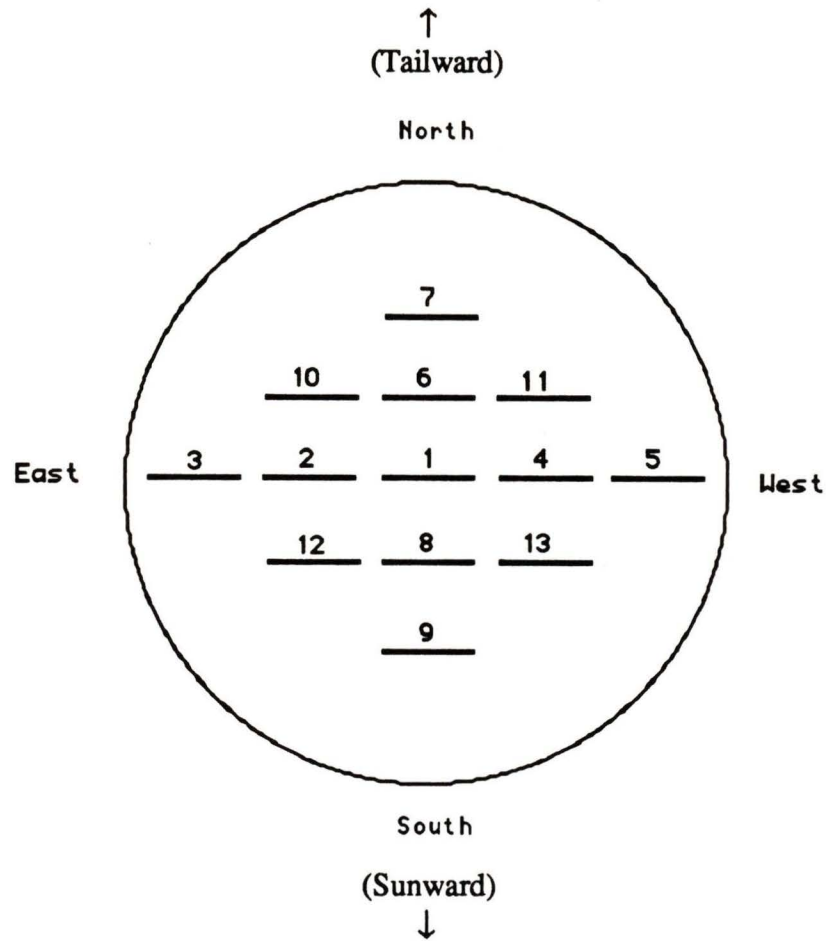


Figure 10 The Spectra Taken. The positions in the coma of Comet P/Halley of the 13 spectra taken with the Anglo-Australian Telescope. The nucleus of the comet is at the center of the first spectrum's slit. The centers of neighboring spectra are separated by 4 minutes of arc from one another (this applies to both horizontal and vertical neighbors).

CHAPTER 4 REDUCING THE DATA

4.1 IRAF

The spectra of Comet P/Halley were reduced with version 2.3 of the Image Reduction and Analysis Facility (IRAF) software created by Doug Tody of the National Optical Astronomy Observatories (NOAO). IRAF was chosen as it is the most complete reduction package currently written and is quickly becoming the standard in image reduction software. With the adoption of IRAF as the operating environment for the Space Telescope Science Institute's Science Data Analysis System (SDAS), IRAF promises to evolve into the most comprehensive software package for astronomical data reduction and analysis ever written. Other strengths of IRAF include its built-in command language which provides the user interface to the system as well as being an interpreted programming language and its high portability to differing hardware architectures through the use of kernels which provide an interface from IRAF's virtual operating system to the host operating system.

Tasks are accomplished in IRAF by accessing routines in different packages through the command language interface. The routines that were used to reduce the AAT data are described individually in Appendix 4. They shall be referred to henceforth by their names only.

4.2 THE REDUCTION PATH TAKEN

As stated earlier, the data consist of 17 two-dimensional images (220 x 2040 pixels each) written to tape in FITS format. The RFITS routine was used first to read the data into image files useable by IRAF. After examining the images both visually (using a Parallax™ image processing system) and through IRAF (using the SPLOT routine), it was apparent

that not all of the data in each image would be useable. Accordingly, every image was trimmed in size to 170 x 1301 pixels using the IMCOPY routine. Note that the 1301 pixel size in the dispersion direction was not chosen because the discarded data were unuseable, but because of speed gains that resulted when working with a smaller image (only the spectral region containing the CN (0,0) violet band was kept). The 170 pixel length in the spatial direction was created by trimming symmetrically about the spectrograph slit's center.

In order to convert the spectra from a pixel scale to a wavelength scale, the 3 copper-argon arc images were examined next. Using the IMPLOT routine, all 3 images were overlaid to see if any shifts had occurred in the spectrograph during the course of the observations. It was found that none had so that all of the comparison arcs were identical. This being the case, the IMSUM routine was used to add all of these spectra together to form one comparison arc spectrum which would be used to dispersion correct the rest of the spectra. In addition, the signal-to-noise ratio (S/N hereafter) was improved by this process. Figure 11 shows the resulting comparison arc spectrum. The laboratory wavelengths of the argon II lines occurring in the comparison arc were obtained by consulting a table of wavelengths kept at the observatory and by the use of a multiplet table (Moore (1959)).

Instrumentally produced errors were corrected for next. As the spectra have very low count rates ($< 0.2 \text{ Hz pixel}^{-1}$), corrections for coincidence count losses did not have to be applied. As well, it will be noted from Appendix 3 that no spectra were taken in order to flat field the data (a typical spectrum to effect this would be of a quartz continuum source or a dome flat). Because of this the data are not flat fielded. This is not too serious a problem primarily due to the low count rates of the P/Halley spectra and the fact that the small-scale granularity of an IPCS carries little power (only small-scale features matter for the

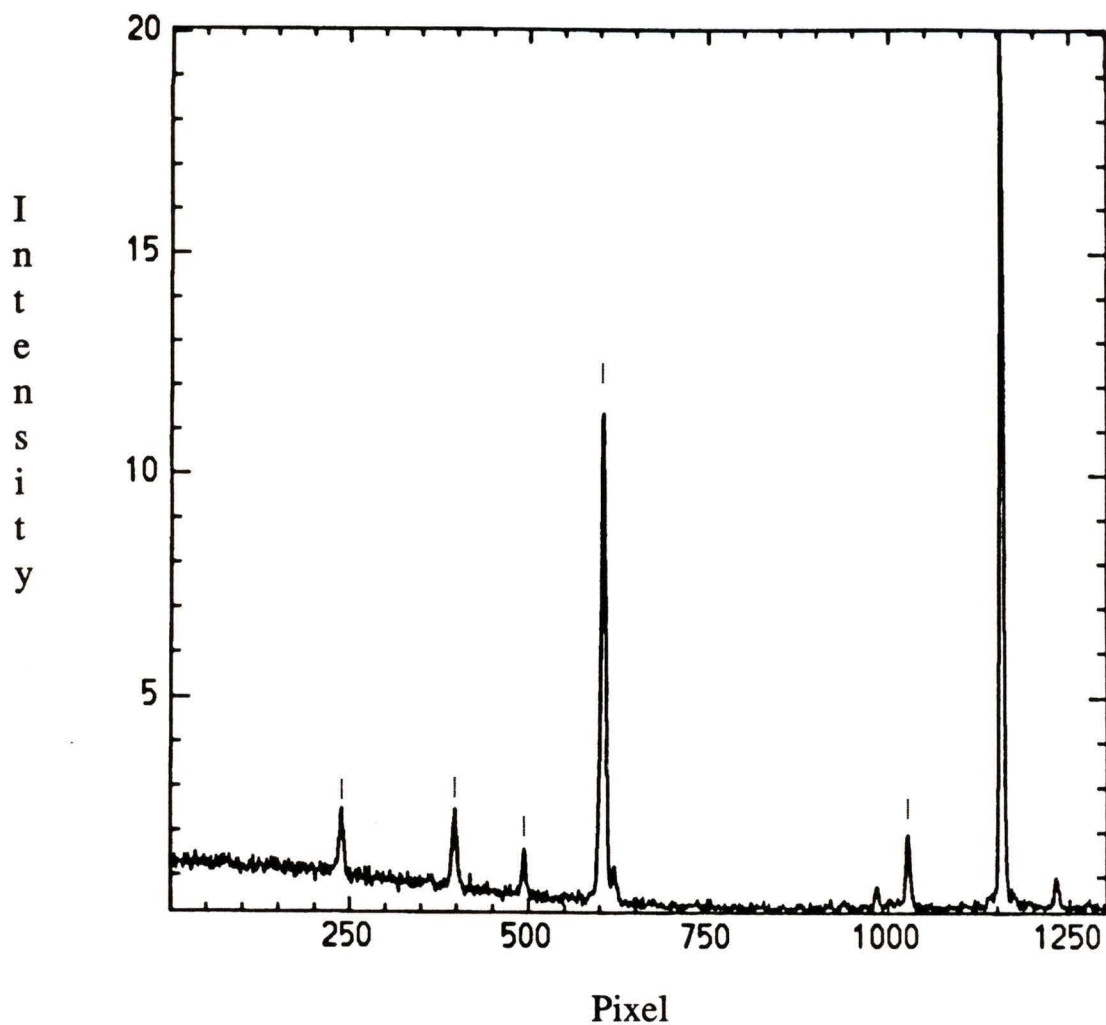


Figure 11 Comparison Arc Spectrum. The copper-argon arc spectrum used to correct the AAT data for pincushion distortion and to convert the data from a pixel to a wavelength dispersion is illustrated. Six lines were used for the wavelength calibration. These lines include the five marked lines and the intense line near pixel 1150. The wavelengths of these argon II lines are, from left to right, 3880.332 , 3875.26 , 3872.15 , 3868.528 , 3855.18 , and 3850.581 Angstroms.

Greenstein effect). At the worst, a 1% error will be introduced into the data by neglecting flat fielding (Hanes (1987) and Durand(1987)).

More serious errors are introduced by pin-cushion distortion and s-distortion, both of which are corrected for. Usually, either the delays for data taking on the IPCS are preset at the start of the observations or a slit with several holes in it is illuminated by a quartz source and the resulting point-source images are used to map out the s-distortion. In our case, neither was done. Fortunately, a spectrum of the asteroid Ceres was taken and could be used to map out the s-distortion with a little effort. The asteroid appears nearly as a point-source spectrum through the center of the two-dimensional image. In order to map out the s-distortion over the entire IPCS faceplate, an artificial spectrum was constructed in which the image of Ceres was duplicated several times down the slit length. Figure 12 shows a slice taken of this artificial spectrum parallel to the slit or spatial orientation. The peaks correspond to the duplicated spectral image of Ceres seen in cross section. The IRAF routine IDENTIFY was then run to create a database of features that were to be used in order to trace out the s-distortion (the features have to be manually marked only once and corresponded to the peaks of the Ceres spectrum seen in Figure 12). The task REIDENTIFY was used so that the positions of these features could be traced every 10 pixels across the length of the dispersion, thus mapping out any s-distortion in the detector. (Note that this method assumes that the s-distortion is the same everywhere on the IPCS faceplate as it is across the center. It is argued that first-order corrections will thus be attained resulting in only very small second-order errors due to varying s-distortion profiles perpendicular to the dispersion. The spectrum of Ceres has to be copied several times down the slit in order to fit a function to the distortion.) The result of REIDENTIFY is a database of feature coordinates which are used by the routine FITCOORDS in order to fit a function to the s-distortion. This function was fitted manually until the residuals were satisfactory.

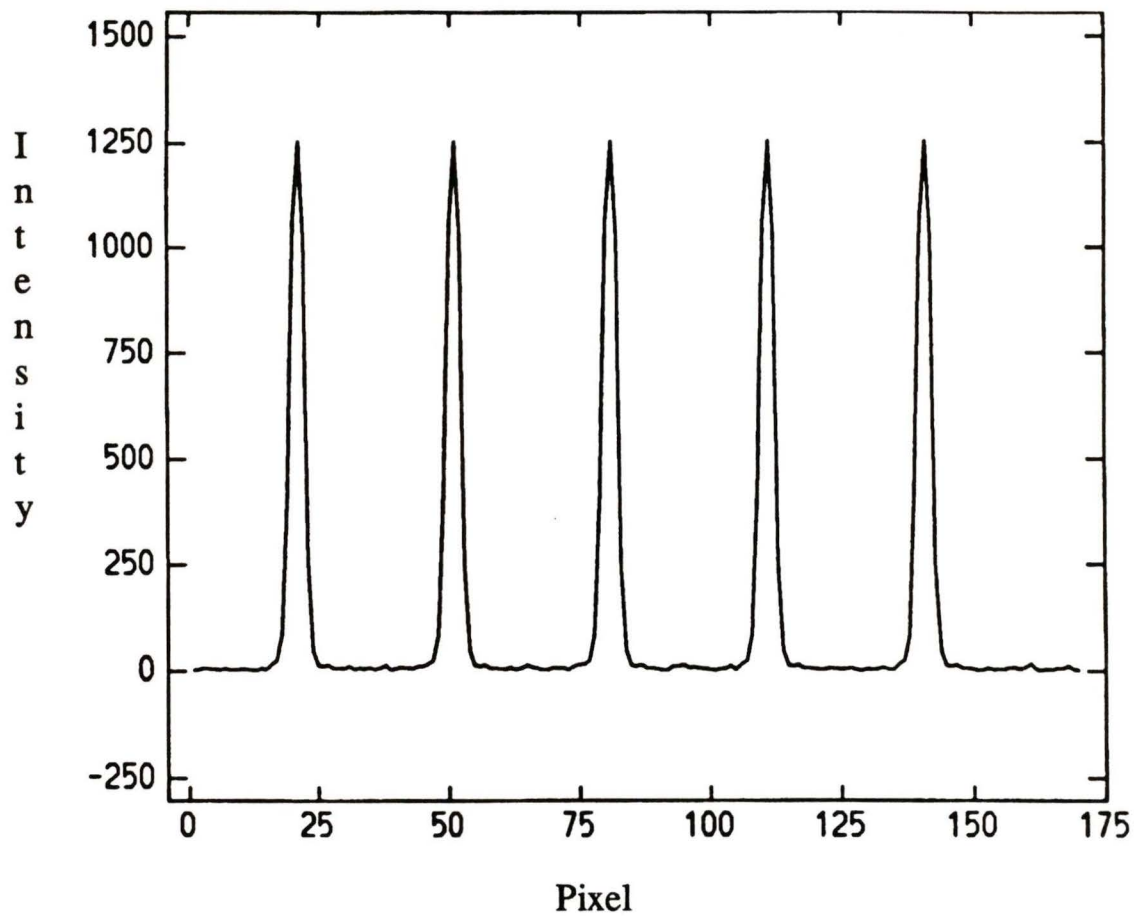


Figure 12 Artificial Ceres Spectrum. The spectrum of Ceres was duplicated several times down the slit length and is illustrated here in cross-section. This artificial spectrum was used to map out any s-distortions over the IPCS faceplate.

The process of mapping out any curvature or pin-cushion distortions is very similar to the one just described. The comparison arc spectrum is used to correct for curvature and to convert the spectra to a wavelength scale. Once again the routine IDENTIFY was used to mark features (the six spectral lines assigned wavelengths in Figure 11 were the features marked). These features were then located every 10 pixels perpendicular to the dispersion with the task REIDENTIFY. Next, a function was fitted manually with the routine FITCOORDS as before. This results in two functions which can be applied to the spectra to correct for curvature and s-distortion while converting the spectra to a linear wavelength scale. From this operation, it was found that the spectra had a dispersion of $32 \text{ m}\text{\AA}/\text{pixel}$. The routine TRANSFORM is used to accomplish the corrections and was applied to all 13 of the P/Halley spectra as well as the spectra of Ceres and the comparison arc. Note that the wavelengths are not corrected for Doppler shifts due to the earth-comet motion. The spectra were also further trimmed to 1189 pixels along the wavelength axis during this task.

Once the instrument-induced distortions had been corrected and the spectra put on a linear dispersion scale, they could be collapsed into one-dimensional spectra. Since a detailed analysis of the Greenstein effect would require high spatial resolution, each two-dimensional spectrum of the comet was divided, perpendicular to the dispersion, into 17 "bins", with 10 pixels belonging to a bin. This division was chosen as the S/N of each bin is large enough to still be useful over the entire range of spectra taken and the spatial resolution is increased by a substantial 17 times. For each bin the 10 corresponding pixels were summed to form a one-dimensional spectrum with an effective integration time of 10,000 seconds. The routine TOONEDSPEC was used to collapse the spectra in such a manner. Since there are 13 spectra and 17 bins per spectra, this resulted in 221 one-dimensional spectra being produced. It should be noted that bin numbers, which will be referred to throughout the remainder of the thesis, are assigned consecutively across the slit

so that pixels 1 to 10 compose the first bin and pixels 161 to 170 compose bin number 17. Also, if the slit is oriented from east to west, the left-most end of the slit (i.e. the east end) corresponds to bin number 1 while bin number 17 corresponds to the right-most (west) 10 pixels.

The reduced data thus consist of 221 one-dimensional spectra of the coma of comet P/Halley, in particular the CN (0,0) violet system at 3883 \AA . Figure 13 shows one such spectrum (spectrum position 1, bin 9, corresponding to the center spectrum positioned on the nucleus of the comet). This spectrum will be used in the Chapter 6 when dealing with the Swings effect. To enhance isotopic lines of cyanogen, other than $^{12}\text{C}^{14}\text{N}$, hidden within the data, all 221 spectra were co-added into a single spectrum with an effective integration time of 2,210,000 seconds (25.58 days). Because all of the spectra have the same linear dispersion, 32 m\AA / pixel , and the same starting wavelength, 3850 \AA , the spectra were co-added together by simply using the IRAF routine IMSUM. The resulting spectrum will be fully discussed in sections 6.4 and 6.5. The reduced data along with the co-added spectrum were lastly written back to tape in FITS format with the routine WFITS. These spectra have also been accepted by the International Halley Watch for archiving.

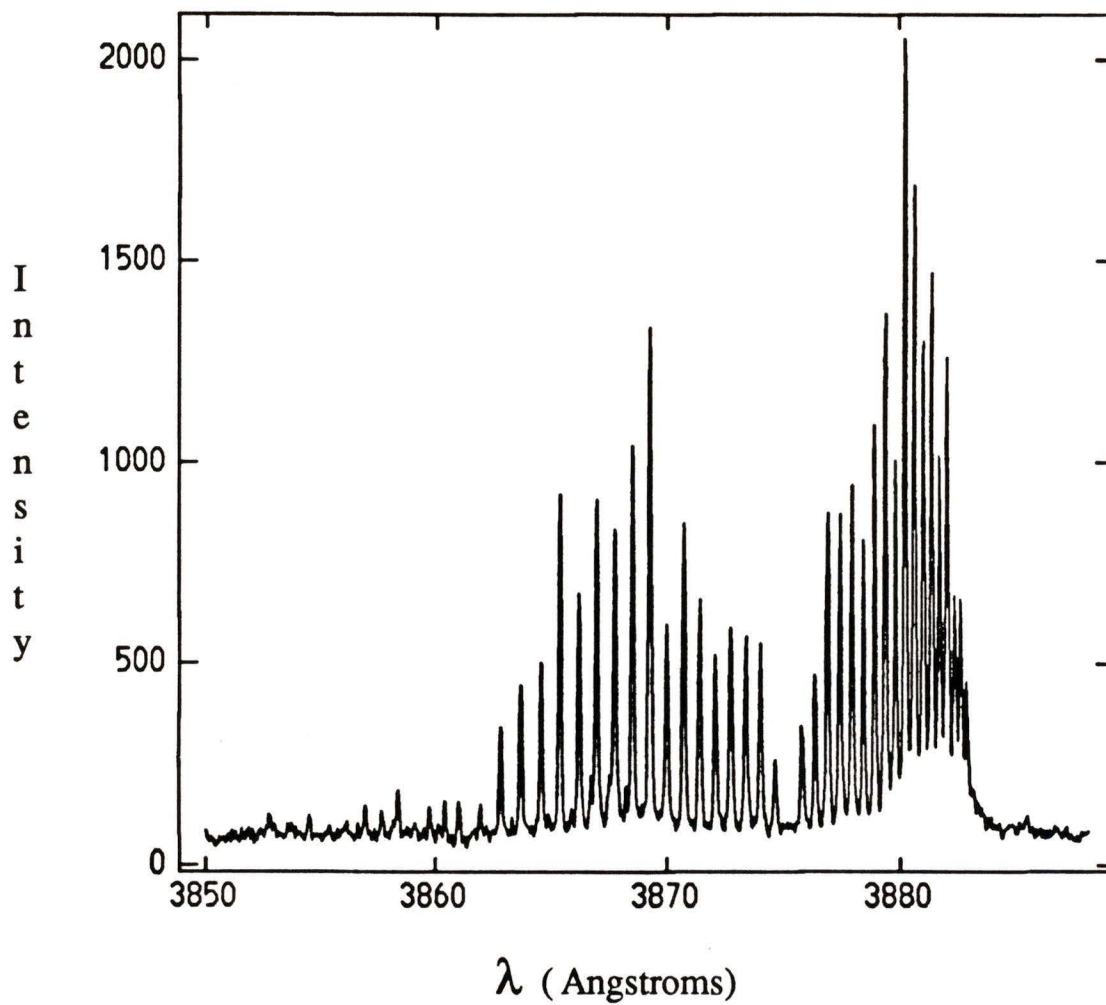


Figure 13 The P and R Branches of the CN(0,0) Violet System. The CN (0,0) band system at 3883 Angstroms corresponding to the center spectrum taken of Comet P/Halley (position 1, bin 9) is shown.

CHAPTER 5 THE CYANOGEN MOLECULE

5.1 DIATOMIC MOLECULAR SPECTROSCOPY

As cyanogen is a heteronuclear diatomic molecule, it will be worthwhile to review briefly the spectra of diatomic molecules in order to introduce fundamental concepts pertaining to this thesis. Although most of the following information can be found in Herzberg (1950), it is included herein for completeness.

In a diatomic molecule, each electronic level or state is split up into vibrational levels which are further subdivided into rotational levels. Transitions between 2 electronic states of the molecule result in spectra which occur in the visible and ultraviolet wavelength regions. The spectrum that arises from such a transition is called an *electronic band system* and includes all of the vibrational and rotational transitions that result between the 2 electronic states. The electronic band system itself consists of several sequences of *bands*, each band crowding up towards a *band head*. The band head may occur on either the red or blue end of the band. Each band corresponds to a transition between 2 vibrational levels in the molecule. Each line within a band is the result of a transition between specific rotational levels within the vibrational level. Figure 14 and 15 illustrate the structure of an electronic band system and a hypothetical transition leading to the production of a band.

Figure 16 depicts a single band in more detail. The band has 2 branches ; the branch that moves off to the red from the origin is called the *P branch*. The branch to the blue of the origin is called the *R branch* . In Figure 16 the P branch comes to a head. However, the R branch may come to a head instead. It was first noticed by Deslandres that the wavenumbers of both branches can be fitted to a single parabola of the form

$$\sigma = \sigma_0 + am + bm^2,$$

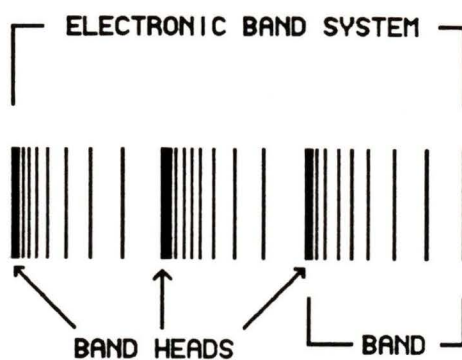


Figure 14 An Electronic Band System. The appearance of a hypothetical electronic band system is depicted. The band system consists of three bands with each band coming to a band head.

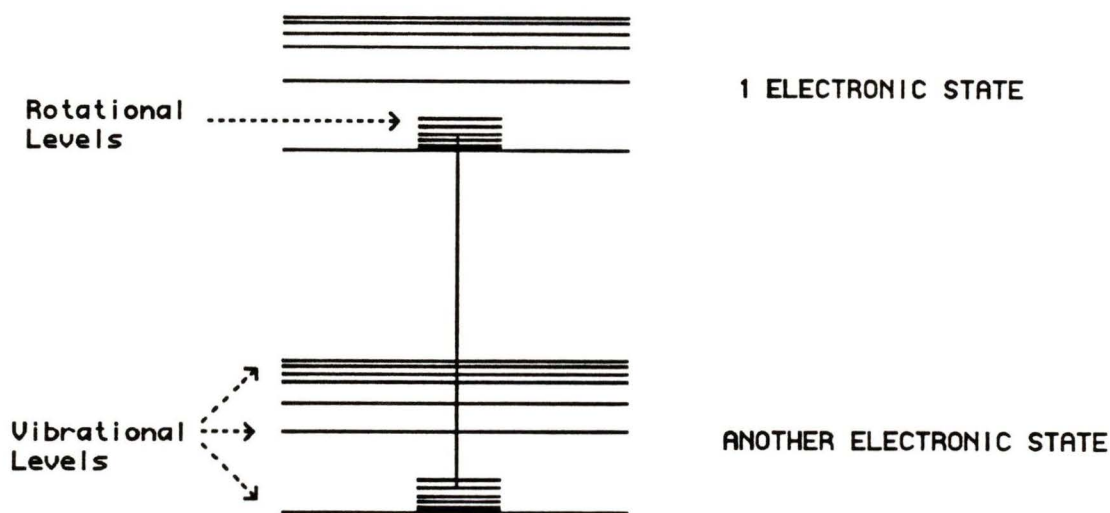


Figure 15 Band Creation. A band arises due to transitions occurring between two vibrational levels of different electronic states of the molecule. The individual lines in a band are produced by transitions between specific rotational levels of each of the vibrational levels involved. The transition shown here would result in one line of a band being produced.

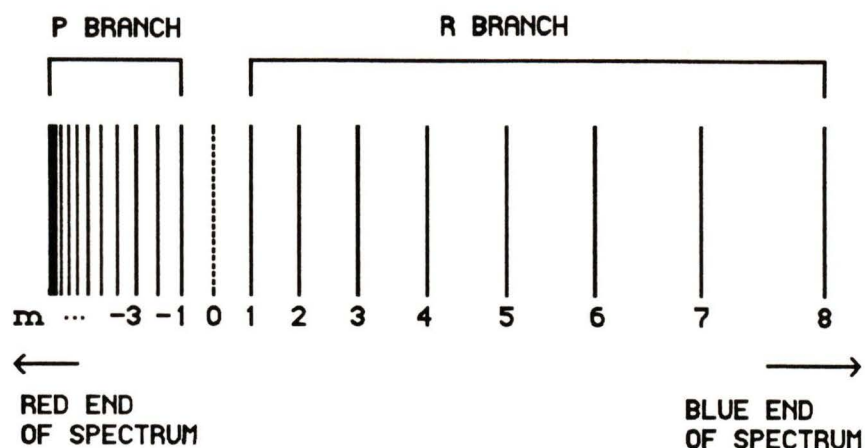


Figure 16 Structure of a Single Band. The detailed structure of a hypothetical band is shown. The wavenumbers of both the P and R branches of the band may be fitted by a single formula involving the variable 'm'. The missing line at $m=0$ is called the band origin.

N	J	Parity
4	9/2	+
	7/2	+
3	7/2	-
	5/2	-
2	5/2	+
	3/2	+
1	3/2	=
	1/2	=
0	1/2	+

Figure 17 The $2\Sigma^+$ State. The first five levels in the energy level diagram for a $2\Sigma^+$ state are depicted. Note the degeneracy of rotational levels ($N>0$) due to the interaction of molecular spin with electron spin ($J=N+S$). Also note that rotational levels with N even have positive parity while those with N odd have negative parity. (There must be a change in parity for electric dipole radiation to occur).

where σ_0 , a , and b are constants and m is a whole number which numbers the successive lines. By allowing negative values of m in addition to positive we can begin counting ($m=0$) at any line. From Figure 16 it can be seen that one line is missing in the band. This missing line is called the *band origin* and is given the value $m = 0$. With this definition, σ_0 is the wavenumber of the band origin. When represented graphically, the parabola is called a *Fortrat parabola*.

In addition to the P and R branches, there is sometimes another branch, called the *Q branch*, which fits another, different parabola. The vertex of the Q branch lies almost at the band origin.

The spacing of the lines in a band is related to the rotational inertia of the molecule. If we assume that the rotational motion of a diatomic molecule can be approximated as the rotation of a rigid body about its center of mass, then the rotational energy of the molecule is given by

$$E = \frac{I \omega^2}{2}.$$

Setting the Hamiltonian to the above energy and solving Schrödinger's wave equation yields (for the energy of the rotational levels)

$$E = \frac{\hbar^2}{2I} J(J+1), \quad (13)$$

where J is the rotational quantum number ($J = 0, 1, 2, \dots$). Finally, by dividing Equation (13) through by hc , the term values of the rotational levels are given by

$$\begin{aligned} F(J) &= \frac{\hbar^2}{2Ihc} J(J+1) \\ &= \left(\frac{h}{8\pi I c} \right) J(J+1) \\ &= B J(J+1), \end{aligned} \quad (14)$$

where B is the *rotational constant*. Experimentally it is found that Equation (14) is too simplistic and the term values of the rotational levels can be fitted according to

$$F(J) = B J (J+1) - D J^2(J+1)^2 + \dots \quad (15)$$

where D is the *centrifugal distortion constant*.

We shall now consider the wavenumbers of lines resulting from a change in the rotational state for any given vibrational transition. By convention a single prime (') shall represent the upper level of the transition and a double prime (") the lower level. The term values of the upper electronic state are (ignoring the centrifugal distortion constant)

$$T_e' + B' J'(J'+1),$$

while those of the lower state are

$$T_e'' + B'' J''(J''+1).$$

The selection rule for the quantum number J is $\Delta J = 0, \pm 1$. Transitions where $\Delta J = 0$ form the Q branch, those with $\Delta J = +1$ ($J' = J'' + 1$) form the R branch, and those with $\Delta J = -1$ ($J' = J'' - 1$) form the P branch. With this in mind, it is found that the wavenumbers of the R-branch lines can be fit with the formula

$$\sigma = \sigma_0 + 2B' + (3B' - B'')J'' + (B' - B'')J''^2, \quad (16)$$

where $J'' = 0, 1, 2, \dots$. Similarly, the wavenumbers of the P-branch lines can be fit with the formula

$$\sigma = \sigma_0 - (B' + B'')J'' + (B' - B'')J''^2, \quad (17)$$

where $J'' = 1, 2, 3, \dots$. It is customary to label lines with J'' . With such a notation the first line of the P branch is P(1) whereas the first line of the R branch is R(0). (It is also customary to label the transition between vibrational levels which create the electronic band system with the *vibrational quantum numbers* v' and v'' in the form (v', v'')). With such nomenclature, the transition from $v' = 0$ to $v'' = 0$ in the cyanogen molecule would be labelled CN (0,0). As before, the wavenumbers of the lines in both the P and R branches can be represented by a single formula. If we let $m = J + 1$ for the R branch and $m = -J$ for the P branch (with no line at $m = 0$) then

$$\sigma = \sigma_0 + (B'+B'')m + (B'-B'')m^2 . \quad (18)$$

Taking into account the centrifugal distortion constant D gives the more accurate expression

$$\sigma = \sigma_0 + (B'+B'')m + (B'-B''-D'+D'')m^2 - 2(D'+D'')m^3 - (D'-D'')m^4 . \quad (19)$$

It can be seen from Equation (19) that in order to determine the wavenumbers of lines in the P or R branches, all that is required are accurate values for the molecular constants B' , B'' , D' , and D'' of the two electronic states for the molecule in consideration.

In general, each molecule has many band systems and electronic states. The classification of these electronic states is similar to that used for atomic energy states. There are 3 angular momentum vectors associated with diatomic molecules, L , S , and R (the electronic orbital angular momentum, the electron spin, and the rotational angular momentum of the molecule respectively). It is found to be more appropriate to classify the electronic states of diatomic molecules according to the value of $|M_L|$, the component of the electronic orbital angular momentum along the internuclear axis, than according to the value of L . It is customary to put

$$\Lambda = |M_L| .$$

The quantum number Λ can take the values

$$\Lambda = 0, 1, 2, \dots, L.$$

Corresponding to $\Lambda = 0, 1, 2, 3, \dots$, the molecular state is designated a Σ , Π , Δ , Φ , ... state, analogous to the mode of designation for atoms. It should be noted that Π , Δ , Φ , ... states are doubly degenerate since M_L can have the two values $+\Lambda$ and $-\Lambda$ whereas Σ states are non-degenerate.

Like atoms, the spins of the individual electrons form a resultant spin S . The component of this spin vector along the internuclear axis, M_S , is denoted by Σ (not to be confused with the Σ molecular state). The quantum number Σ can take the values

$$\Sigma = S, S-1, \dots, -S.$$

Σ is not defined for states with $\Lambda=0$ (i.e. Σ states).

The convention for notation is to write the value of $2S+1$ as a top left superscript to the electronic state and the value of $\Lambda+\Sigma$ as a bottom right subscript. For an electronic state with $\Lambda=0$ and $S=1/2$ for example, the state would be designated a ${}^2\Sigma$ state with substates ${}^2\Sigma_{-1/2}$ and ${}^2\Sigma_{1/2}$.

The angular momenta L , S , and R can be added in various ways as first demonstrated by Hund. We shall examine Hund's case (b) for adding these momenta as this case pertains to the transition of interest with regards to the cyanogen molecule and the current research.

In Hund's case (b), the spin S is not closely coupled to the internuclear axis (always the case in Σ states). As such, no "good" quantum number can arise from combining Λ and Σ . Instead, it is better to consider the angular momentum of the molecule (less the electronic spin) as a quantum number. This quantum number, N , is given by

$$N = \Lambda + R.$$

The total molecular angular momentum is then

$$J = N + S.$$

The selection rules for Hund's case (b) are

$$\Delta S = 0$$

$$\Delta \Lambda = 0, \pm 1$$

$$\Delta J = 0, \pm 1$$

and

$$\Delta N = 0, \pm 1 \quad (\Delta N = \pm 1 \text{ for } \Sigma\text{-}\Sigma \text{ transitions}).$$

In addition to the notation of naming the branches depending on the value of ΔJ , there is an additional notation which depends on the value of $\Delta N = N' - N''$. Branches with $\Delta N = -1$ are called *P-form* branches, those with $\Delta N = 0$ are *Q-form* branches, and

those with $\Delta N = +1$ are *R-form* branches. Thus, transitions involving $\Delta J = -1$ and $\Delta N = 0$, for example, form a Q-form P branch (designated QP).

Finally, a brief note should be made on the concept of symmetry. In a Σ state, the electronic eigenfunction may remain unchanged or change in sign on interchanging the 2 nuclei. If the total eigenfunction remains unchanged, then the parity is said to be positive and the state is called a Σ^+ state. If the sign changes, then the parity is negative and the state is designated by Σ^- . For Σ^+ states, all rotational levels with N even have positive parity and all with N odd have negative parity (the reverse is true for Σ^- states). For electric dipole transitions, the parity must change between the rotational levels of the transition.

5.2 THE ($B^2\Sigma^+ - X^2\Sigma^+$) VIOLET SYSTEM OF CN

The CN (0,0) violet system at 3883 Å is produced by transitions between rotational levels of the $v'=0$ vibrational level of the $B^2\Sigma^+$ electronic state of the CN molecule and the $v''=0$ vibrational level of the ground or $X^2\Sigma^+$ electronic state. Since it is a $\Sigma-\Sigma$ transition, Hund's case (b) applies to the addition of the angular momenta. In this case, $\Lambda=0$, $S=1/2$ ($\Sigma=1/2$), and the parity of the total eigenfunction describing the transition is positive. Recall that $N = \Lambda + R$ so that $N = 0, 1, 2, 3, \dots$ in this case. Figure 17 depicts the energy level diagram for a $^2\Sigma^+$ state. It can be seen that for $N>0$, each rotational level is split up into two levels of slightly different energy (this is due to the fact that $\mathbf{J} = \mathbf{N} + \mathbf{S}$, or $J = N \pm \frac{1}{2}$). This degeneracy results in each spectral line being split up into three components. The two main lines with $\Delta N = \Delta J$ are strong and close together while the satellite line ($\Delta N \neq \Delta J$) is weak and more distant. As this fine structure was not seen in any of the cometary spectra, the calculations regarding the Swings effect will not take into account the interaction between molecular rotation and electron spin. Figure 18 depicts this simplified energy level diagram of the CN (0,0) violet band showing the formation of the

P and R branches. By considering the equilibrium established between these rotational levels, the Swings effect may be modeled.

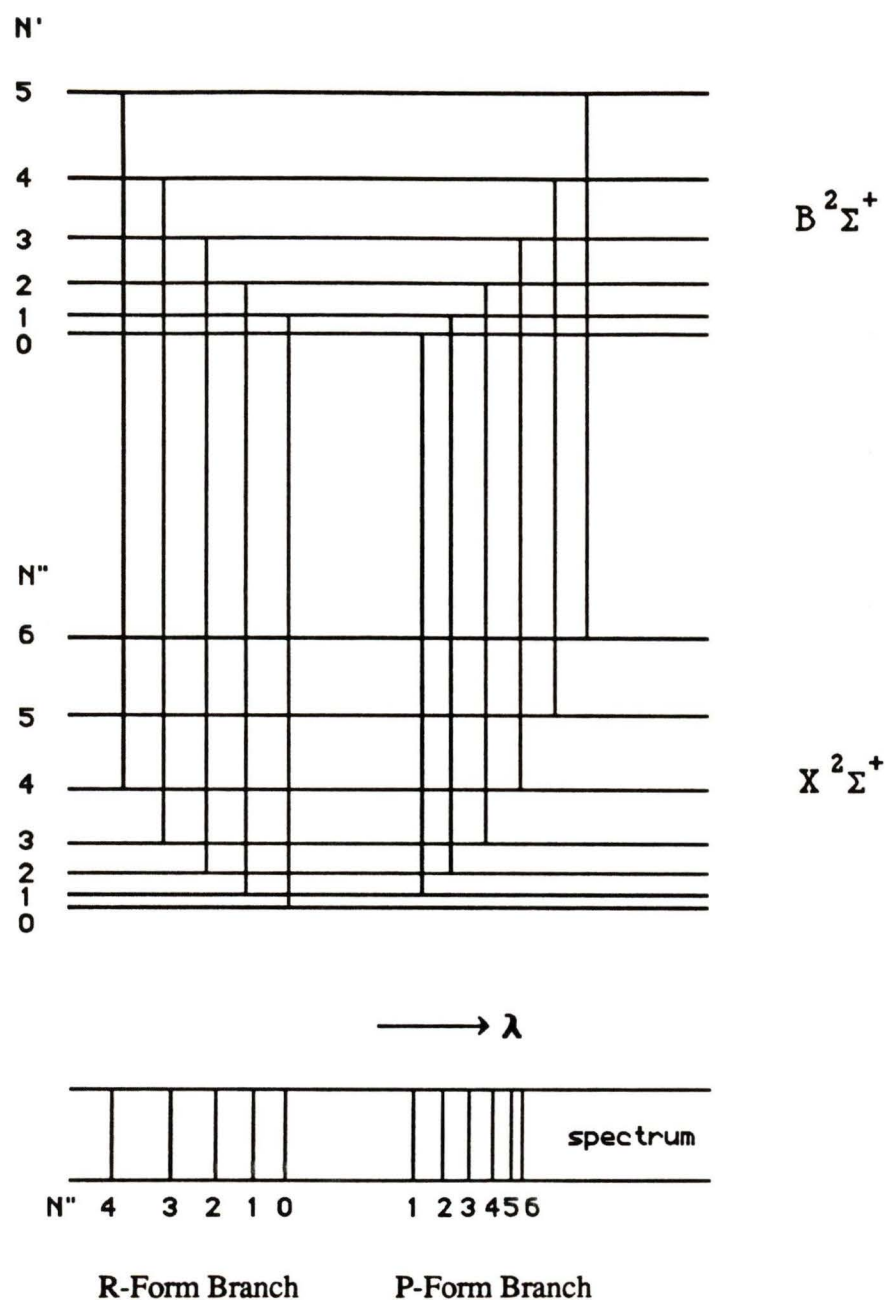


Figure 18 Formation of the P and R Branches. The energy level diagram of the $B^2\Sigma^+ - X^2\Sigma^+$ violet system of CN (0,0) is shown along with the spectrum that arises from the indicated transitions. Note that the degeneracy of the rotational states due to interaction between molecular rotation and electron spin is ignored. Inclusion of this degeneracy would result in each spectral line being broken up into three components. (Drawing is not to scale; Adapted from Aikman et al (1974)).

CHAPTER 6 THE SWINGS EFFECT

6.1 THE RESONANCE-FLUORESCENCE MODEL

A pure fluorescent formulation is used to model the Swings effect as first given in detail by Arpigny (1964) and later recast by Aikman et al (1974). Although the equations used in the equilibrium model have been clearly set forth by Aikman et al (1974), they are repeated here for completeness sake.

The notation we will use is as follows:

$N_{N'}$ is the number of molecules in the upper electronic state ($B \ ^2\Sigma^+$) having quantum number N' .

$N_{N''}$ is the number of molecules in the lower electronic state ($X \ ^2\Sigma^+$) having quantum number N'' .

$U_{R(N')}$, $U_{P(N'')}$ are the radiation densities per unit wavelength interval of the solar radiation at the distance of the comet at the wavelength of the $R(N')$ and $P(N'')$ lines, allowance being made for Doppler shift.

A , B are the Einstein A- and B-coefficients for spontaneous emission and stimulated absorption for the electronic transition.

$A_{N'',N''-1}$ is the Einstein A-coefficient for spontaneous emission for a pure rotational transition.

It must also be noted that the transition probabilities (Hönl-London factors) are $(N+1)/(2N+1)$ and $N/(2N+1)$ if N increases by 1 or decreases by 1, respectively.

Considering the possible transitions to and from a level in the lower electronic state gives the following equation for the equilibrium of a level in this state:

$$N_{N''}'' \left[\left(\frac{N''+1}{2N''+1} U_{R(N'')} + \frac{N''}{2N''+1} U_{P(N'')} \right) B + A_{N'',N''-1} \right] = \\ \left(N_{N''+1}' \frac{N''+1}{2N''+3} + N_{N''-1}' \frac{N''}{2N''-1} \right) A + N_{N''+1}'' A_{N''+1,N''}. \quad (20)$$

Likewise, considering transitions to and from a level in the upper electronic state yields the equilibrium equation:

$$N_{N'}' A = \left(N_{N'-1}'' \frac{N'}{2N'-1} U_{R(N'-1)} + N_{N'-1}'' \frac{N'+1}{2N'+3} U_{P(N'+1)} \right) B. \quad (21)$$

Arpigny (1964) and Aikman et al (1974) give the following equation for the pure rotational Einstein coefficients

$$\frac{A_{(N'',N''-1)}}{B} = \frac{GN''^4}{N'' + \frac{1}{2}} \quad (22)$$

where G is an unknown constant of proportionality.

Substituting Equations (21) and (22) into Equation (20), rearranging, and setting

$$x_{N''} = \frac{N_{N''}''}{N_0''} \quad \text{and} \quad y_{N'} = \frac{N_{N'}'}{N_0''},$$

we obtain

$$\begin{aligned}
& \left[\frac{N''(N''-1)}{(2N''-1)(2N''-3)} U_{R(N''-2)} \right] x_{N''-2} \\
& - \left[\frac{N''(N''-1)}{(2N''+1)(2N''-1)} U_{P(N'')} + \frac{(N''+2)(N''+1)}{(2N''+3)(2N''+1)} U_{R(N'')} + \frac{GN''^4}{N'' + \frac{1}{2}} \right] x_{N''} \\
& + \left[\frac{G(N''+1)^4}{N'' + \frac{3}{2}} \right] x_{N''+1} + \left[\frac{(N''+1)(N''+2)}{(2N''+3)(2N''+5)} U_{P(N''+2)} \right] x_{N''+2} = 0 \quad (23)
\end{aligned}$$

and

$$y_{N'} = \frac{B}{A} \left(\frac{N'}{2N'-1} U_{R(N'-1)} x_{N'-1} + \frac{N'+1}{2N'+3} U_{P(N'+1)} x_{N'+1} \right). \quad (24)$$

The x-values are proportional to the populations of the rotational levels in the ground state while the y-values are proportional to the populations of the levels in the upper state, and hence (if the lines are optically thin) to the observed intensities. The numerical computer model proceeds by first calculating Equation (23) for every rotational level N'' considered (usually the first 30 rotational levels are used). The matrix of coefficients is then solved to yield the x-value of each rotational level. These values are used with Equation (24) to solve for the predicted intensities of the lines in the R branch of the CN (0,0) violet band. The intensities are then normalized so that they may be compared with the observations. As mentioned above, the value of G is unknown but is varied until solution of the equations gives the least squares deviation of the calculated intensities from the observed intensities.

6.2 REFINEMENT AND COMET BENNETT

The first task of the current research on the Swings effect was to rewrite the computer model originally developed by Aikman et al (1974) so that it used more recent and accurate molecular constants in determining the wavenumbers of lines in the P and R branches of

the CN (0,0) violet band. Whereas Aikman et al (1974) used the wavenumber equation for the (0,0) band given by Weinard (1955), we adopt Equation (19) with the molecular constants of Engleman (1974). In addition, the calculations of Aikman et al (1974) used the centre-of-disk solar radiance spectrum of Delbouille et al (1973). They converted this to a whole-disc irradiance spectrum using the solar radiance tables of Houtgast (1970). The current models employ a digital whole-disc irradiance spectrum of very high resolution obtained at Kitt Peak National Observatory. The solar irradiance tables of Beckers et al (1976) are used to place it on an absolute scale.

To study the effect of the above mentioned changes, the theoretical Swings effect was computed for Comet Bennett (1969i) using the orbital parameters described by Aikman et al (1974) and compared against the previous published results. At the time of observation, the radial velocity of the comet with respect to the sun was +26.64 km/s and the heliocentric distance of the comet was 0.7856 astronomical units. Aikman et al (1974) used an empirical value for the free parameter G of $4.72 \times 10^{-4} \text{ J m}^{-3} \text{ m}^{-1}$ (the dimensions of G are those of radiation density per unit wavelength interval), whereas Tatum and Gillespie (1977) later determined the value of G from theoretical arguments to be $5.73 \times 10^{-4} \text{ J m}^{-3} \text{ m}^{-1}$ for the same set of observations. The same number of rotational levels, twenty-five, were used in both models.

Figure 19 shows the results of changing only the molecular constants used in determining the wavenumbers of the (0,0) lines. The solid lines represent the predicted intensities of the R-branch lines using the constants of Engleman (1974) in conjunction with Equation (19) (ie. the present model), and the dotted lines are the predicted R-branch line intensities using the wavenumber equation of Weinard (1955) (ie. the Aikman et al (1974) model constants). In both models a value for G of $4.72 \times 10^{-4} \text{ J m}^{-3} \text{ m}^{-1}$ was used as well as the newer digital solar spectrum. The main difference appears to be in the

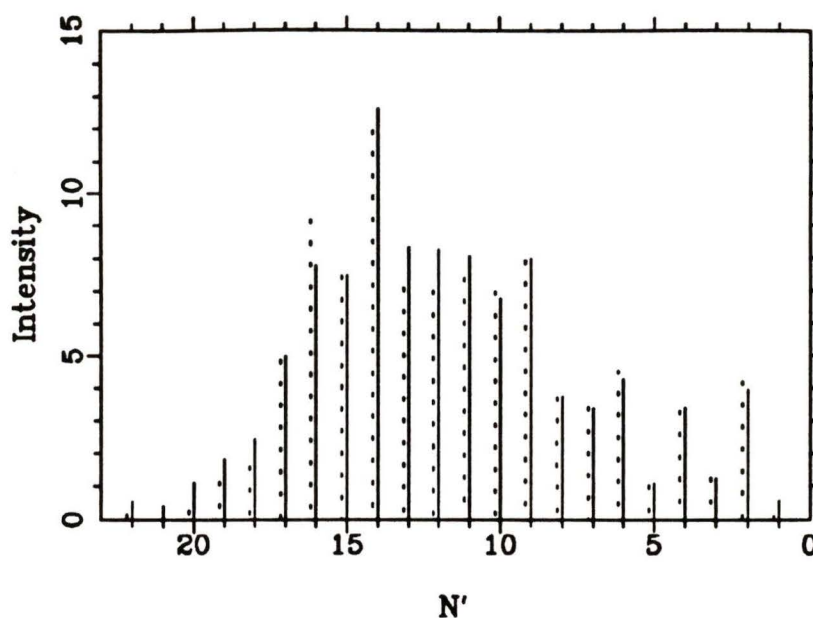


Figure 19 The Effect of Different Molecular Constants on the Swings Effect. The model of Aikman et al (1974) used the wavenumber equation of Weinard (1955) to determine the wavenumbers of the (0,0) lines. Their prediction of the Swings effect in Comet Bennett is indicated by the dotted lines. The current model uses the molecular constants of Engleman (1974) in conjunction with Equation (19) to predict the intensities of R-branch lines in Comet Bennett (solid lines). Both models use the same solar atlas and G value.

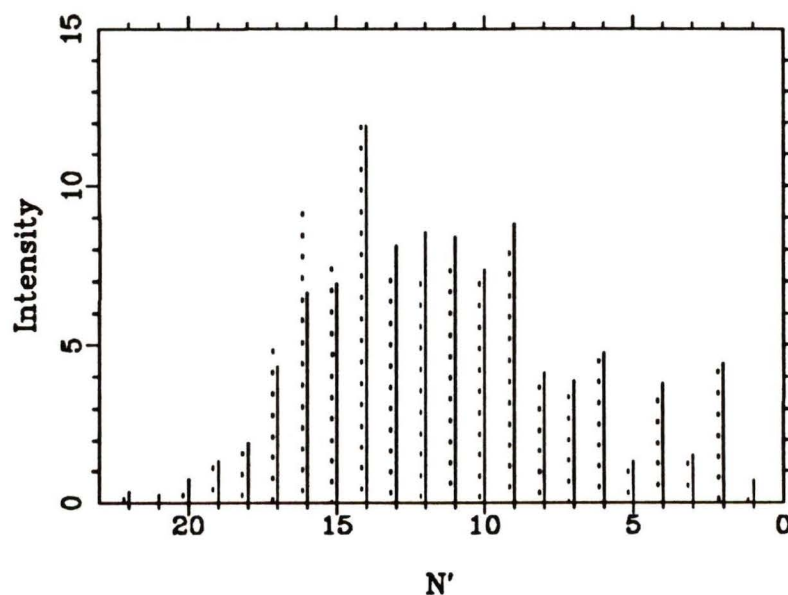


Figure 20 The Effect of G on the Swings Effect . The solid lines indicate the predicted Swings effect for Comet Bennett using a G value of $5.73 \times 10^{-4} \text{ J m}^{-3} \text{ m}^{-1}$ and the molecular constants of Engleman (1974). The dotted lines correspond to the model of Aikman et al (1974) where a G value of $4.72 \times 10^{-4} \text{ J m}^{-3} \text{ m}^{-1}$ was used along with the wavenumber equation of Weinard (1955). Both models use the same whole-disc solar spectrum.

calculated intensity for the R(15) ($N'=16$) line as well as the R(10), R(11), R(12), and R(13) lines in addition to those lines with $N' > 17$. With the exception of R(15), the present model predicts stronger intensities for the above mentioned lines than the model with older molecular constants.

The next step in comparing the models was to vary the value of G as well as the molecular constants in order to see if the discrepancy between the empirical and analytical values of G discovered by Tatum and Gillespie (1977) were due only to the use of an inaccurate solar spectrum and molecular constants. Figure 20 illustrates the results of this test. The solid lines are the predicted R-branch line intensities of the present model employing the newer solar spectrum and molecular constants as well as the analytical value for G of $5.73 \times 10^{-4} \text{ J m}^{-3} \text{ m}^{-1}$. The dotted lines are the predicted R-branch line intensities of the model by Aikman et al (1974) but upgraded to use the newer digital solar spectrum. It can be seen that the agreement between predicted intensities for lines with $N' > 17$ has been improved as well as for the R(13) line. The R(15) line intensity disagreement between the models has been increased however and in addition, the present model now predicts that line R(8) should be more intense than the older model. These differences will be important in determining the advantages of the present model over that of Aikman et al (1974) if any exist.

Figure 21 is a plot of the observed R-branch line intensities in Comet Bennett overlaid by their predicted intensities. The solid lines represent the observed intensities in the comet whereas the dotted lines are those predicted by the present model which incorporates a newer solar spectrum and molecular constants as well as the analytical value of G over the model used originally by Aikman et al (1974). The first 7 lines (R(0) through R(6)) are clearly not modeled well but this is true in the original model by Aikman et al (1974) as well and is to be expected based on previously discussed arguments.

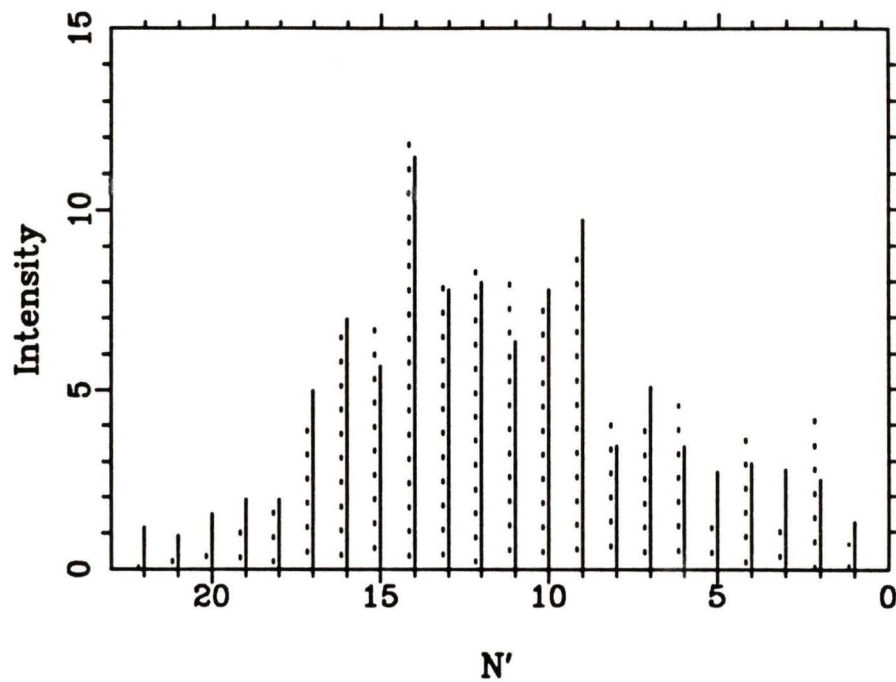


Figure 21 The Swings Effect for Comet Bennett. The observed R-branch line intensities in Comet Bennett (solid lines) are compared against the theoretical model (dotted lines) developed as an improvement to the model by Aikman et al (1974).

Comparing this plot with the original by Aikman et al (1974) leads to the following conclusions. Line R(12) is now modeled correctly and there is also an improvement in modeling the lines with $N' > 17$. Where discrepancies still exist, they are reproduced in both models. Note in addition that the intensities of lines R(15) and R(8) are predicted much better by the new model than they would be if the new solar spectrum were used but with the molecular constants of Weinard (1955) and the empirical G value determined by Aikman et al (1974). It is thus evident that the earlier discrepancy in G found by Tatum and Gillespie (1977) is due largely to the use of an inaccurate solar spectrum. These results confirm that the present model using a new solar spectrum and molecular constants is indeed an improvement over that of Aikman et al (1974).

6.3 COMET P/HALLEY

In order to study the Greenstein effect in Comet P/Halley, it is first necessary to model the Swings effect at the coma's center and determine the value for the free parameter G . Figure 22 shows the R-branch lines of P/Halley for spectrum position 1, bin 9 (the center of the coma). The intensities of the first 21 lines (R(0) through R(20)) will be modeled. Note that although only 21 line intensities are to be predicted, the model will use 30 rotational levels in its internal solution to assure that a realistic equilibrium is established. At the time of middle exposure for Figure 22 (April 15.3674, 1986), Balam (1987) gives the following orbital parameters for the comet :

$$\begin{array}{lll}
 \text{Heliocentric Distance } R \text{ (A.U.)} & = & 1.3987 \\
 \text{Radial Velocity } \dot{R} \text{ (km/s)} & = & + 26.37 \\
 \text{Geocentric Distance } \Delta \text{ (A.U.)} & = & 0.4433 .
 \end{array}$$

Before proceeding to calculate the theoretical Swings effect for P/Halley we must first determine the observed R-branch line intensities from Figure 22. Both the line heights and

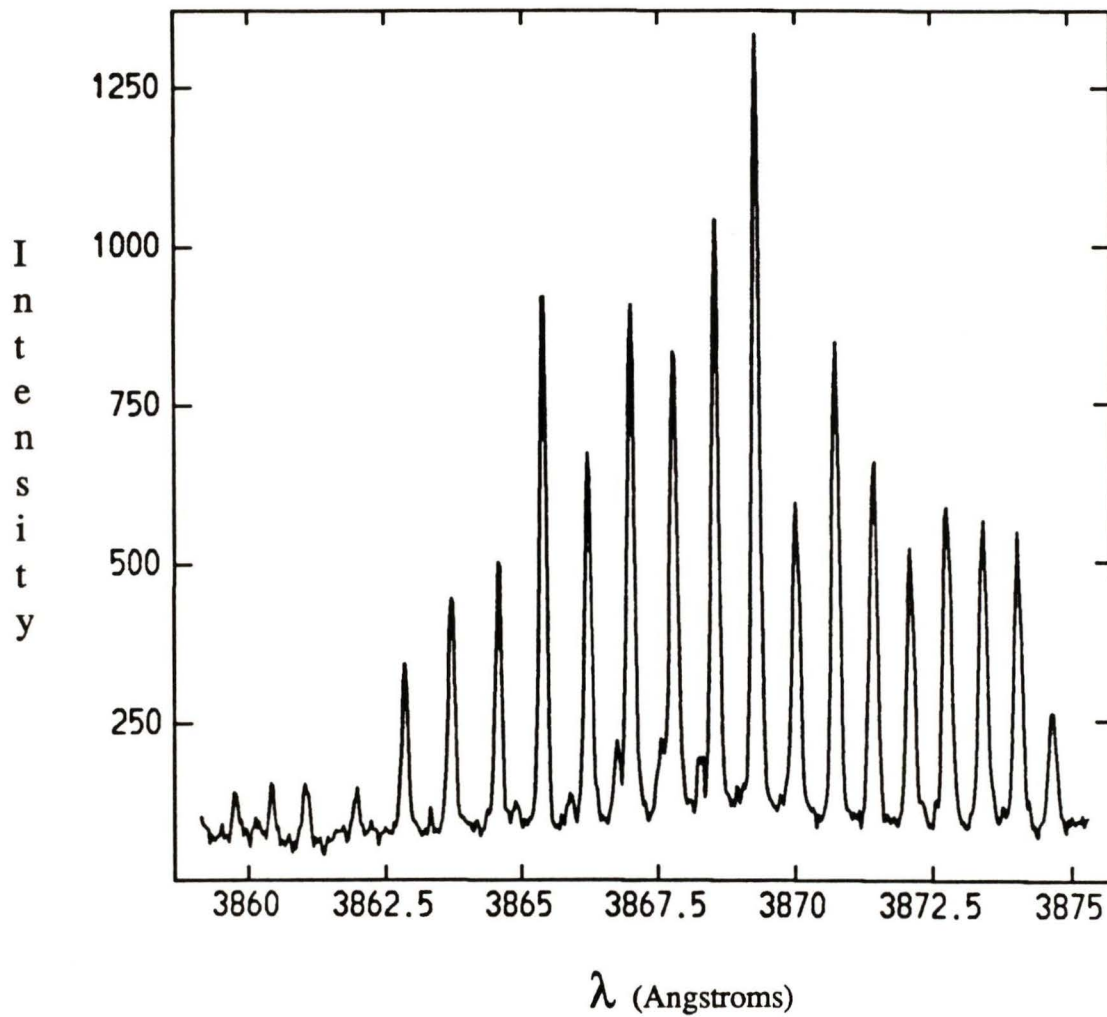


Figure 22 The R Branch of Comet P/Halley. The R-branch lines of Figure 13 are shown belonging to the center spectrum taken of Comet P/Halley. The rightmost line is R(0) and the leftmost R(20). These 21 lines are used to demonstrate the Swings effect in Comet P/Halley.

area enclosed within a line were determined for each line using the IRAF package SPLOT with the 'c' and 'e' keystrokes respectively as a measure of the flux. When using the 'e' keystroke a constant continuum was set for the entire R-branch. These data are tabulated in Table 2 and illustrated in Figure 23 (after normalization). The solid lines of Figure 23 represent the integrated line intensities and the dotted lines are the line heights. It is immediately apparent that the two measures of line intensity produce slightly different results. The integrated intensities will be used throughout the remainder of the thesis as the true measure of line flux due to this method's ability to account for the effects of blending on a line's apparent strength.

With the observed Swings effect established, the theoretical line intensities were computed. The value of G was varied until the sum of the squares of the residuals (the difference between the observed line intensity and the computed intensity) of the lines reached a minimum. Figure 24 shows that this least-squares minimum in the residuals is indeed a global minimum. Figure 25 is a close-up of the minimum region showing the empirical determination of the value of G to be $3.634 \times 10^{-4} \text{ J m}^{-3} \text{ m}^{-1}$.

The Swings effect corresponding to this determined value of G is illustrated in Figure 26. The solid lines represent the observed line intensities while the dotted lines are the computed intensities (this shall be the case henceforth unless otherwise noted). It can be seen that apart from the first 7 rotational lines, the fit between theory and observation is very good supporting the initial assumption that the coma is optically thin.

To see if there might be motions within the central coma, the radial velocity was varied from 20 km/s to 32 km/s and the sum of the squares of the residuals were again examined for a minimum. It was found that a global minimum in the residuals existed corresponding to a radial velocity of +26.84 km/s. The Swings effect corresponding to

Table 2. R-branch Line Intensities for Comet P/Halley

Line	Integrated Intensity (arbitrary units) ($\pm 2.6\%$)	Line Height (arbitrary units)
R(0)	1296	258.8
R(1)	2736	544.6
R(2)	3086	563.2
R(3)	3298	584.0
R(4)	2670	517.7
R(5)	3463	654.4
R(6)	4476	845.0
R(7)	3276	590.2
R(8)	7251	1332.0
R(9)	5287	1040.0
R(10)	4626	830.4
R(11)	4722	903.0
R(12)	3468	668.9
R(13)	4380	917.4
R(14)	2167	497.0
R(15)	2112	441.0
R(16)	1361	337.5
R(17)	430.1	144.8
R(18)	452.1	151.1
R(19)	405.7	153.1
R(20)	394.3	138.6

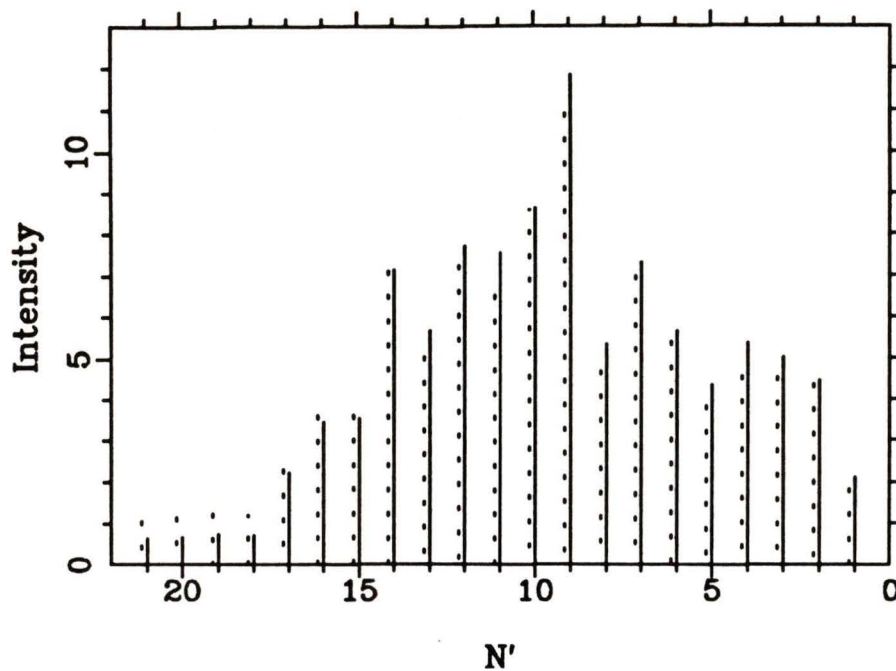


Figure 23 Integrated Intensities versus Line Heights. The R-branch line intensities of Figure 22 were measured in two different ways with the results depicted above. The solid lines correspond to the integrated intensities of the lines (ie. the area enclosed within a line is used as a measure of its flux) and the dotted lines are the line heights. Both sets of data were first normalized to total 100 before plotting.

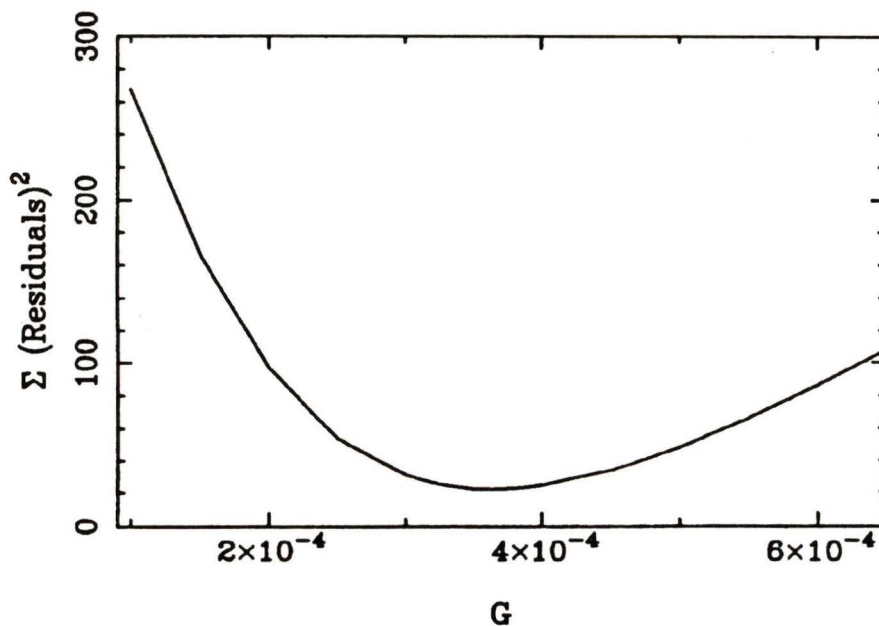


Figure 24 The Determination of G . The value of G was determined for the P/Halley Swings effect model by minimizing the sum of the squares of the residuals (the difference between the observed line intensity and the computed intensity) of the lines. It can be seen that the value of G obtained is a global minimum.

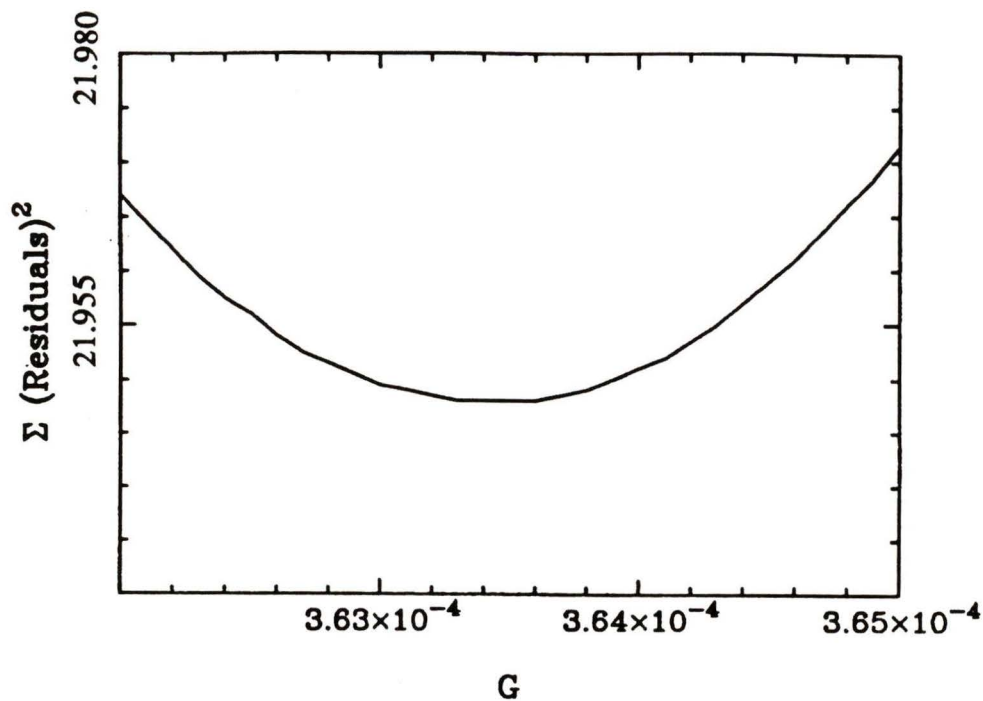


Figure 25 *The Minimum Region.* The minimum region of Figure 24 is illustrated showing the empirical value of G to be equal to $3.634 \times 10^{-4} \text{ J m}^{-3} \text{ m}^{-1}$.

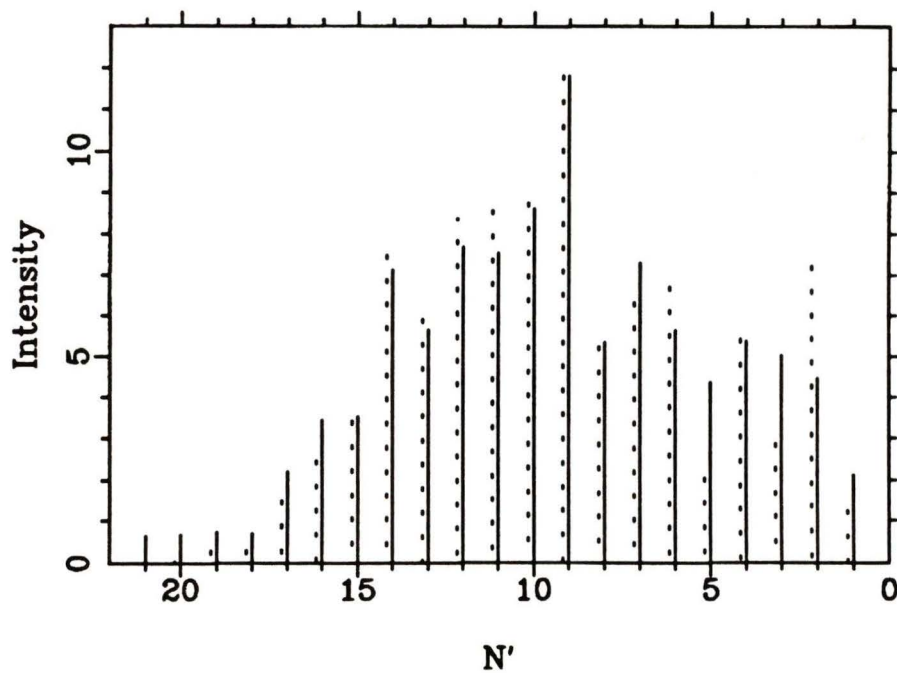


Figure 26 *Comet P/Halley Swings Effect.* The Swings effect is shown modeled for the first 21 R-branch lines of the CN(0,0) violet system according to the conditions present at the time of observation of Comet P/Halley. The solid lines represent the observed line intensities and the dotted lines are those calculated by fluorescence equilibrium.

this radial velocity is depicted in Figure 27. This result indicates that the cyanogen gas in the central coma has an additional radial velocity above that of the nucleus of + 0.47 km/s.

As mentioned earlier, the Swings effect model used herein fails to predict accurately the line intensities of the first seven rotational lines (as expected). In order to study the Greenstein effect in great detail in P/Halley it was decided that six lines would need to be used (for redundancy sake) in order to monitor the evolution of three different line ratios throughout the coma of the comet. It would thus be necessary to predict very accurately the line intensity of each of these lines given the radial velocity of the gas at that point in the coma. The six lines chosen were R(7), R(8), R(9), R(12), R(13) and R(14). These lines were chosen as they could be both predicted and measured accurately throughout the 221 spectra of the coma. Since the first 7 lines are never well predicted with the current model, the value of G was again determined by finding the minimum of the sum of the squares of the residuals in the predicted and observed line intensities ignoring the first 7 lines. A value of $G = 3.701 \times 10^{-4} \text{ J m}^{-3} \text{ m}^{-1}$ was found in this manner. Once again the radial velocity was varied until a best-fit solution was found (ignoring the first 7 lines) corresponding to $\dot{R} = + 26.47 \text{ km/s}$. This is only a difference of + 0.1 km/s above that of the nuclear motion. Figure 28 shows this best-fit solution. With these parameters the chosen six lines to be used in the next chapter are modeled remarkably well. This value of G will thus be used in creating a map of the velocity of the cyanogen gas throughout the coma of P/Halley at the time of observation.

6.4 ADDITIONAL SPECTRAL FEATURES FOUND

In Section 4.2 it was mentioned that all of the 221 spectra of the CN (0,0) violet band system in P/Halley were co-added to form one spectrum with an effective integration time of 25.58 days. This spectrum is illustrated in Figure 29. It can be seen from this spectrum

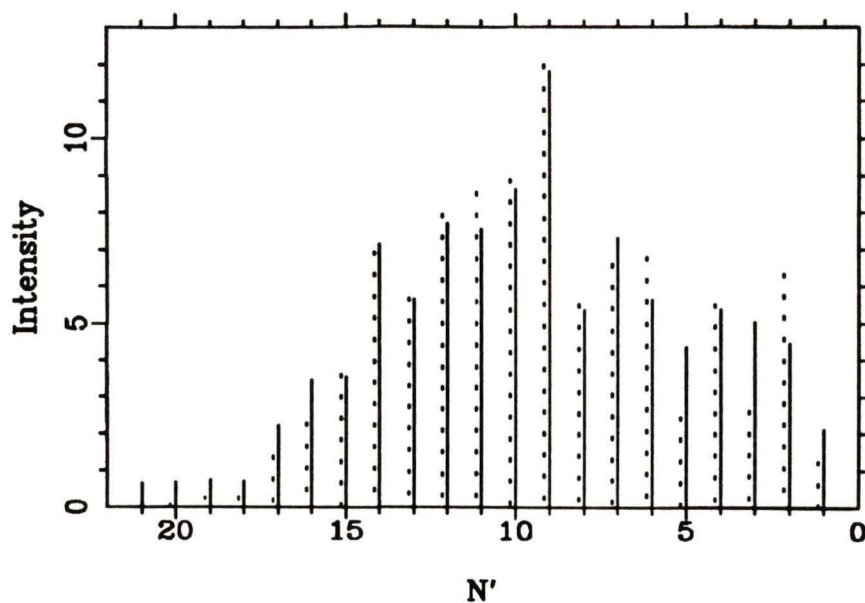


Figure 27 Radial Velocity Best Fit. The radial velocity of the comet was varied to see if there might be gas motions within the central coma and the resulting Swings effect was examined for a better fit. A best-fit solution was found corresponding to a radial velocity of +26.84 km/s and the resulting Swings effect is shown above. The solid lines represent the observed line intensities and the dotted lines are those calculated by fluorescence equilibrium.

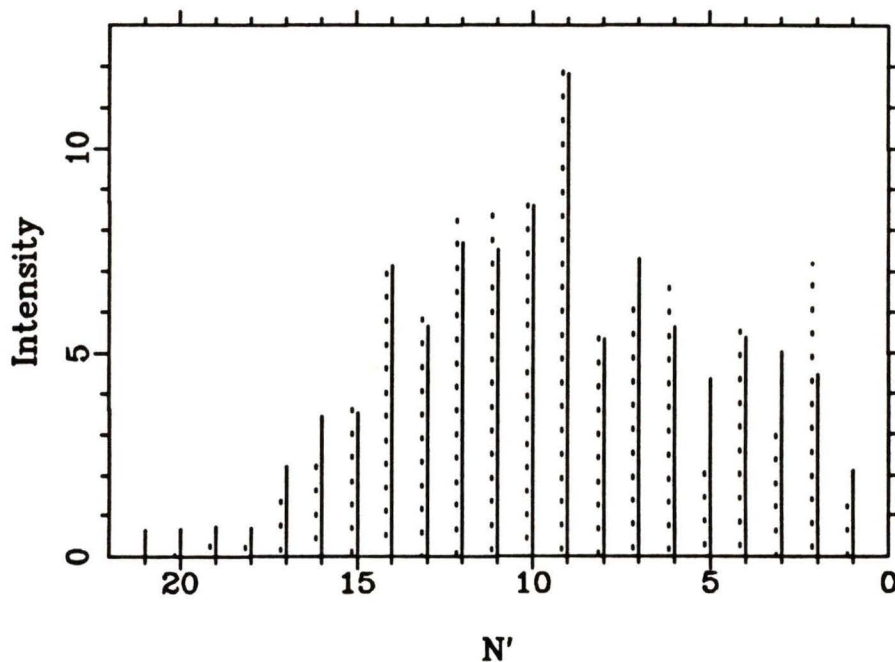


Figure 28 Swings Effect Best Fit. The Swings effect is shown corresponding to a G value of $3.701 \times 10^{-4} \text{ J m}^{-3} \text{ m}^{-1}$ and a radial velocity of +26.47 km/s. These parameters are the result of performing best-fit solutions when the first 7 R-branch lines are not included. The solid lines represent the observed line intensities and the dotted lines are those calculated by the model.

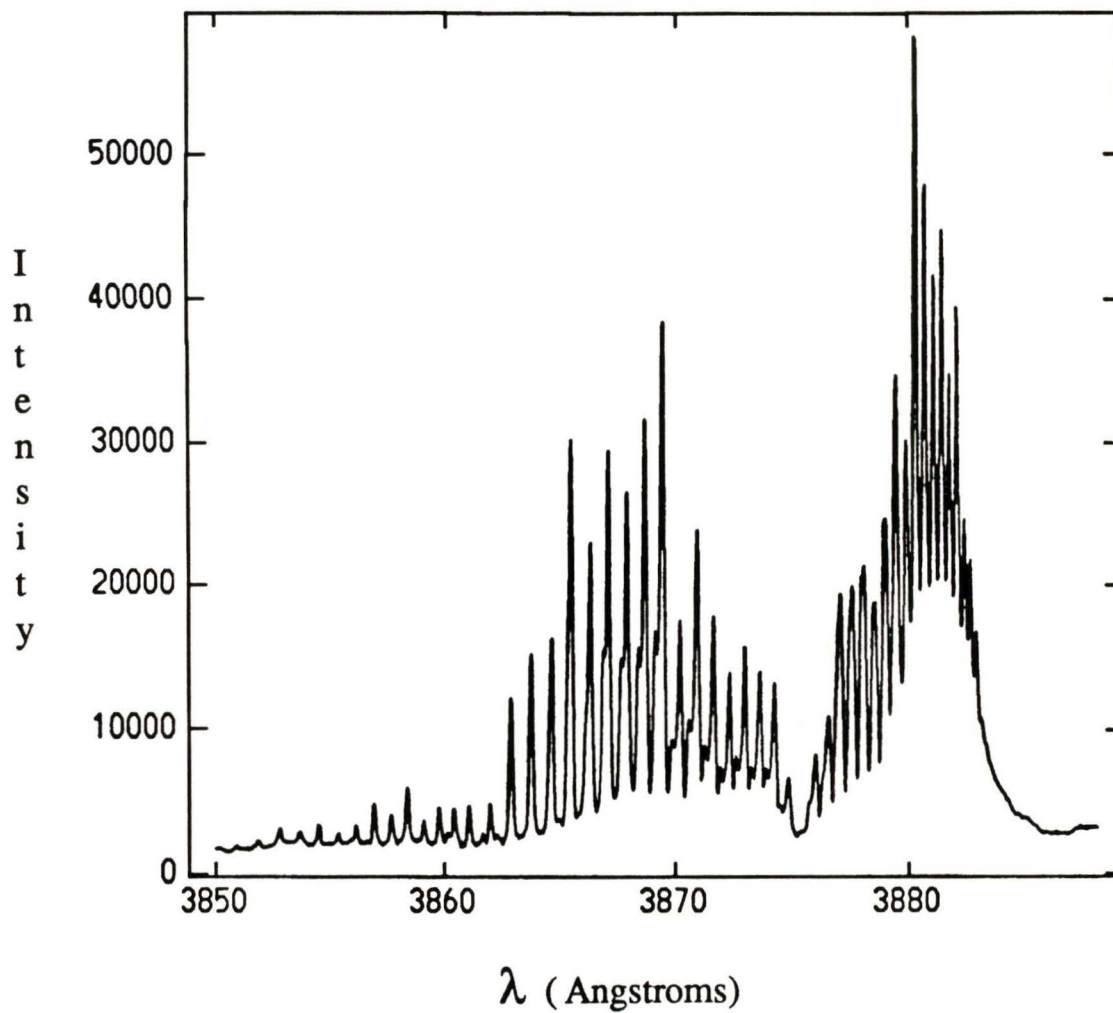


Figure 29 The Co-Added Spectrum. The illustrated spectrum was obtained by co-adding all of the 221 spectra of the CN (0,0) violet band system in P/Halley and has an effective integration time of 25.58 days. Note the additional lines interspersed throughout the R branch not belonging to the $^{12}\text{C}^{14}\text{N}$ (0,0) R-branch lines.

that there are lines not belonging to the $^{12}\text{C}^{14}\text{N}$ (0,0) band interspersed throughout the R branch. Figure 30 is an isolated view of the R branch which clearly shows the additional lines referred to by the lower-case letters 'a' through 'm'. These lines were not unsuspected considering their previous discovery by Aikman et al (1974) and Wehinger et al (1986). Aikman et al (1974) concluded that the lines belonged either to the (1,1) band of the $^{12}\text{C}^{14}\text{N}$ molecule, or to the (0,0) band of the $^{13}\text{C}^{14}\text{N}$ molecule. They could not distinguish between their two hypotheses due to the resolution of their spectra. In fact, the lines belong to both the (1,1) band of the $^{12}\text{C}^{14}\text{N}$ molecule and to the (0,0) band of the $^{13}\text{C}^{14}\text{N}$ molecule as discovered by Wehinger et al (1986) and confirmed in the present research. The significance of this discovery is that it enables the $^{12}\text{C}/^{13}\text{C}$ ratio to be determined in the comet through use of both the $^{12}\text{C}^{14}\text{N}$ (0,0) band and the $^{13}\text{C}^{14}\text{N}$ (0,0) band line intensities. Before we discuss this determination however, let us first examine the actual identification of the unknown lines.

The wavelengths of the R(0) through R(12) branch lines as well as the additional unknown lines were measured using the 'e' keystroke of the IRAF SPLOT package. In order to identify the unknown lines accurately, we needed a wavelength list of all the possible CN isotope lines in this spectral region. Zucconi and Festou (1986) have produced such a listing of the wavelengths of the various CN isotope lines (^{12}CN (0,0), ^{13}CN (0,0), C^{15}N (0,0), and ^{12}CN (1,1)) in the 3862 - 3875 Å range (R branch of CN with $N < 18$). The wavelengths of these lines were obtained with an accuracy better than 5 mÅ by means of the spectroscopic constants given by Engleman (1974). The measured line wavelengths could not be directly compared to this list as the comet's spectrum was not corrected for the Doppler shift due to the comet's motion with respect to the earth. The lines were identified by using the known ^{12}CN (0,0) R-branch lines, fitting their measured wavelengths with those calculated by Zucconi and Festou (1986) with a fourth degree polynomial, and then

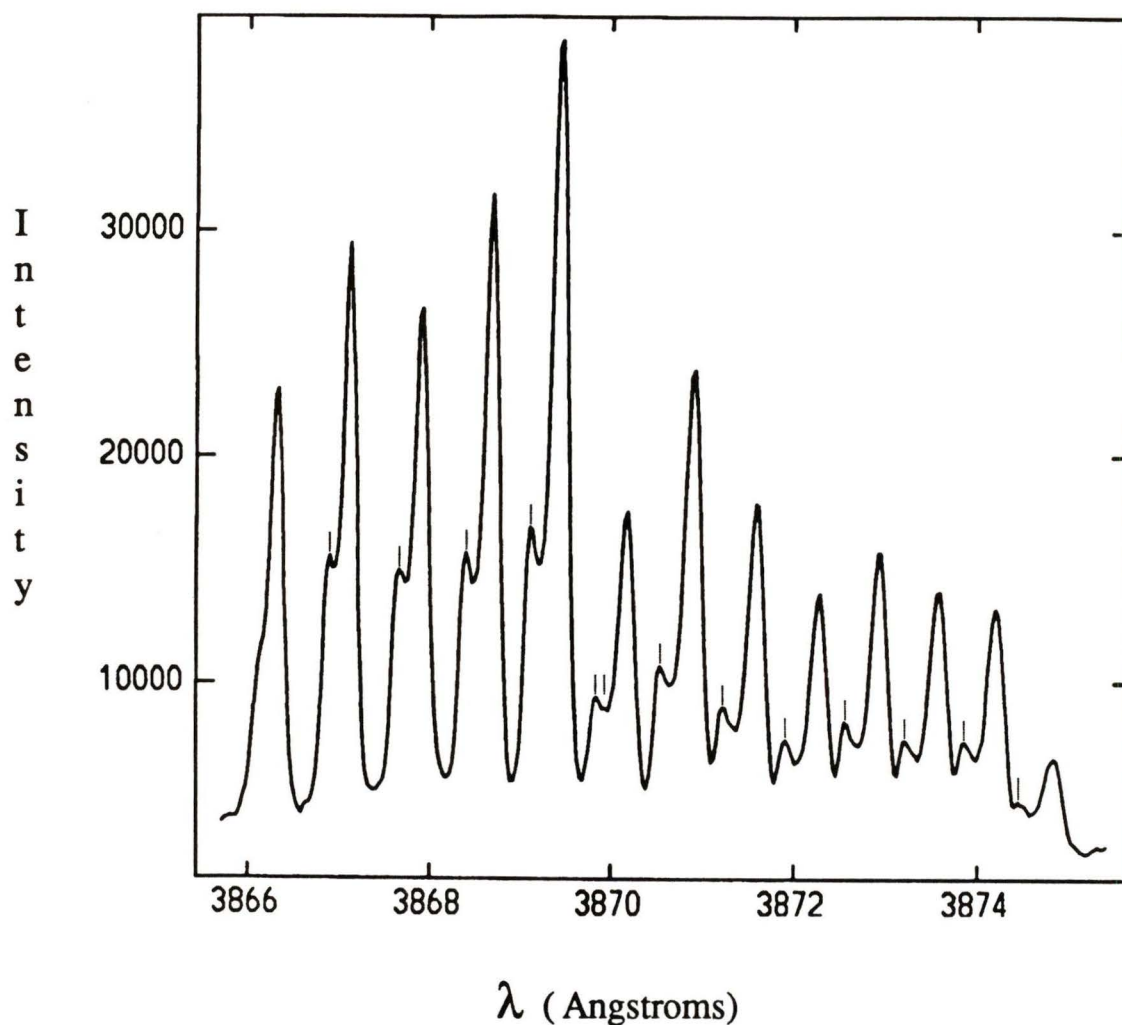


Figure 30 The R-Branch Lines of the Co-Added Spectrum. The R branch of Figure 29 is isolated and expanded to show the unidentified lines appearing in the spectrum. The rightmost line is the R(0) line of the normal isotopic species and the leftmost line is R(12) of the same species ($^{12}\text{C}^{14}\text{N}$ (0,0)). The 13 marked lines between R(0) and R(12) are the unidentified lines and are referred to in the text as lines 'a' through 'm'. Note that line 'a' is the rightmost marked line with the others following alphabetically from right to left.

Table 3. Identification of Unknown Lines in the Co-Added Spectrum

Line Designation	Measured Wavelength (Å)	Line Identification	Error (mÅ)
R(0)	3874.810		
a	3874.455	R(1) ^{13}CN (0,0)	+ 59
R(1)	3874.212		
b	3873.830	R(2) ^{13}CN (0,0)	+ 35
R(2)	3873.590		
c	3873.196	R(3) ^{13}CN (0,0)	+ 14
R(3)	3872.938		
d	3872.566	R(4) ^{13}CN (0,0)	+ 17
R(4)	3872.280		
e	3871.907	R(5) ^{13}CN (0,0)	+ 11
R(5)	3871.607		
f	3871.220	R(6) ^{13}CN (0,0)	- 1
R(6)	3870.905		
g	3870.548	R(7) ^{13}CN (0,0)	+ 22
R(7)	3870.176		
h	3869.923	P(16) ^{12}CN (1,1)	- 8
i	3869.817	R(8) ^{13}CN (0,0)	- 5
R(8)	3869.430		
j	3869.116	P(13) ^{12}CN (1,1)	+ 38
R(9)	3868.673		
k	3868.410	P(11) ^{12}CN (1,1)	+ 4
R(10)	3867.899		
l	3867.670	P(9) ^{12}CN (1,1)	+ 2
R(11)	3867.112		
m	3866.883	P(7) ^{12}CN (1,1)	+ 29
R(12)	3866.300		

interpolating to find the wavelength of the unknown line on the same wavelength scale as the identification list. Table 3 lists all of the measured line wavelengths along with the identification of the unknown lines and the difference between their interpolated wavelength and actual wavelength as given by the identification list.

With the exception of lines 'a' and 'j', the error in the identification is less than the distance to any other nearby isotope lines. Line 'a' lies within 50 mÅ of the R(1) line of $C^{15}N$ (0,0) and line 'j' lies within 10 mÅ of the R(9) line of ^{13}CN (0,0). In both these cases however the measured line is in error to longer wavelengths of the line it is identified with whereas the other nearby isotope line has a smaller wavelength than the identified line. The $C^{15}N$ (0,0) lines are also expected to be only 1/3 as strong as the ^{13}CN (0,0) lines in the spectrum (Zucconi and Festou (1986)).

6.5 THE $^{12}C/^{13}C$ RATIO

It is well known that isotope ratios measured in the neighboring interstellar medium differ from those measured in solar system bodies (Penzias (1980)). Hawkins and Jura (1987) found the $^{12}C/^{13}C$ isotope ratio of the interstellar medium in the neighborhood of the sun to be 43 ± 4 (the terrestrial value of this ratio is 89). Since comets are believed to have been formed in the early solar nebula and to have remained as chemical relics of this era, an accurate determination of the $^{12}C/^{13}C$ ratio in a comet is extremely important. As a consequence of stellar nucleosynthesis, Galactic chemical evolution models predict an increase over time of the abundance of secondary elements to primary elements. The $^{12}C/^{13}C$ ratio should decrease therefore over time. Thus, study of this ratio in a comet will constrain chemical evolutionary models, test whether or not comets were formed in the solar nebula, and probe the homogeneity of the solar nebula.

Only the $^{12}\text{C}/^{13}\text{C}$ ratio has been measured in comets and until recently the method used was through study of the $A-X$ (1,0) band head of $^{12}\text{C}^{13}\text{C}$ (4745 Å). Unfortunately, this emission feature is blended with NH_2 lines at this wavelength resulting in large error bars on the measurements. Using this method, Stawikowski and Greenstein (1964) obtained a ratio of 70 ± 15 in Comet Ikeya (1963a). Because of blending they believe that a slightly higher isotope ratio may be required. Owen (1973) obtained a ratio of 100 ± 20 in Comet Tago-Sato-Kosaka (1969g). Wyckoff et al (1987) obtained a ratio of 65 ± 8 in Comet P/Halley using the $B\ 2\Sigma^+ - X\ 2\Sigma^+ \text{CN}$ (0,0) band for the first time.

The method employed herein will be to use the ^{13}CN (0,0) violet band lines detected in the spectra in conjunction with the ^{12}CN (0,0) band lines in order to deduce the $^{12}\text{C}/^{13}\text{C}$ ratio in Comet P/Halley. The rotational structure of the isotope bands differ because of the Swings effect and so this must also be corrected for in the calculations. In order to determine the isotopic abundance ratio accurately we must use an unblended line in the comet spectrum. Zucconi and Festou (1986) find that the R(7) and R(8) lines of ^{13}CN (0,0) are the best lines to use for post perihelion observations of P/Halley. These two lines are both strong enough to be detectable and are distant from other nearby isotope lines by more than 100 mÅ. In addition, both of these lines are correctly modeled by the Swings effect program used (recall that the first 7 lines, R(0) through R(6), are not modeled correctly). For duplicity sake, both lines will be used in determining the carbon isotope ratio.

The intensities of the R(7) and R(8) lines were found using the 'e' keystroke of the IRAF package SPLIT and are listed in Table 4. These line intensities were measured from the spectrum centered on the comet's nucleus (position 1, bin 9). The co-added spectrum was not used due to strong blending of the isotope lines and the added complication of

Table 4. The $^{12}\text{C}/^{13}\text{C}$ Ratio : R(7) and R(8) Line Intensities

Line	^{12}CN (0,0) Intensity	^{13}CN (0,0) Intensity	Uncorrected $^{12}\text{C}/^{13}\text{C}$ Ratio
R(7)	95.86	1.594	60.14
R(7)	96.45	1.664	57.96
R(8)	208.9	2.425	86.14
R(8)	211.1	2.366	89.22

combining spectra taken in different positions in the coma where the Greenstein effect may alter the isotope line intensities.

The Swings effect must now be calculated for the ^{13}CN (0,0) lines before the true $^{12}\text{C}/^{13}\text{C}$ ratio may be determined. The wavelengths of the lines of ^{13}CN can be calculated, assuming the electronic isotope shift to be zero as reported by Engleman (1974), using the standard isotopic formulae:

$$\begin{aligned} B_e^i &= \rho^2 B_e \\ D_e^i &= \rho^4 D_e \\ \omega_e^i &= \rho \omega_e \\ \omega_e x_e^i &= \rho^2 \omega_e x_e, \end{aligned}$$

where

$$B_0 = B_e - \frac{1}{2} \alpha_e$$

$$\alpha_e^i = \rho^3 \alpha_e$$

$$\rho = \sqrt{\frac{\mu}{\mu^i}} \quad \text{and} \quad \mu = \frac{m_C m_N}{m_C + m_N}.$$

The following numerical values were used in the calculations:

$$m_{^{12}\text{C}} = 12.00000000$$

$$m_{^{13}\text{C}} = 13.00335430$$

$$m_{^{14}\text{N}} = 14.00307438$$

$$B_0' = 1.95874 \text{ cm}^{-1}$$

$$B_0'' = 1.89113 \text{ cm}^{-1}$$

$$\alpha_e' = 0.02215 \text{ cm}^{-1}$$

$$\alpha_e'' = 0.01735 \text{ cm}^{-1}$$

$$D_0' = 6.58 \times 10^{-6} \text{ cm}^{-1}$$

$$D_0'' = 6.41 \times 10^{-6} \text{ cm}^{-1}$$

$$\omega_e' = 2164.13 \text{ cm}^{-1}$$

$$\omega_e'' = 2068.705 \text{ cm}^{-1}$$

$$\omega_e x_e' = 20.25 \text{ cm}^{-1}$$

$$\omega_e x_e'' = 13.144 \text{ cm}^{-1}$$

The data were taken from Aikman et al (1974), Engleman (1974), and Herzberg (1950). From the given formulae it is found that

$$\rho = 0.9790033$$

and for ^{13}CN :

$$B_0' = 1.87757 \text{ cm}^{-1}$$

$$B_0'' = 1.81272 \text{ cm}^{-1}$$

$$D_0' = 6.045 \times 10^{-6} \text{ cm}^{-1}$$

$$D_0'' = 5.888 \times 10^{-6} \text{ cm}^{-1}$$

$$\omega_e' = 2118.690 \text{ cm}^{-1}$$

$$\omega_e'' = 2025.269 \text{ cm}^{-1}$$

$$\omega_e x_e' = 20.036 \text{ cm}^{-1}$$

$$\omega_e x_e'' = 12.598 \text{ cm}^{-1}$$

In order to use Equation (19) to determine the wavenumbers of the ^{13}CN lines, the band origin of the ^{13}CN (0,0) system is still required. The band origin, σ_0 , can be calculated using the formula (from Herzberg (1950)) :

$$\sigma_0 = G(v') - G(v'') + \Delta T_e$$

where

$$G(v) = \omega_e(v+1/2) - \omega_e x_e(v+1/2)^2 + \omega_e y_e(v+1/2)^3 + \dots \quad (25)$$

For the (0,0) band,

$$\sigma_0 - \Delta T_e = \left(\frac{1}{2} \omega_e' - \frac{1}{4} \omega_e x_e' \right) - \left(\frac{1}{2} \omega_e'' - \frac{1}{4} \omega_e x_e'' \right). \quad (26)$$

Using the above determined constants for ^{13}CN ,

$$\sigma_0 - \Delta T_e = 44.851 \text{ cm}^{-1}.$$

Finally, recalling that the electronic isotope shift is zero (ΔT_e is the same for both ^{13}CN and ^{12}CN), we get

$$\begin{aligned} \Delta T_e &= T_e(v') - T_e(v'') \\ &= T_e(\text{B } 2\Sigma^+) - T_e(\text{X } 2\Sigma^+) \\ &= 25,751.903 - 0 \\ &= 25,751.903 \text{ cm}^{-1}. \end{aligned}$$

So, the ^{13}CN (0,0) band origin is

$$\begin{aligned} \sigma_0 &= 25,751.903 + 44.851 \\ &= 25,796.754 \text{ cm}^{-1}. \end{aligned}$$

With the wavenumbers determinable for lines in both the ^{12}CN (0,0) and ^{13}CN (0,0) bands, it was possible to calculate the role of the Swings effect on the $^{12}\text{C}/^{13}\text{C}$ ratio. The Swings effect was calculated for both isotopes using 30 rotational lines in the computation along with a G value of 3.701×10^{-4} , a radial velocity of 26.47 km/s (determined from a least-squares fit of the residuals), and a heliocentric distance of 1.3987 AU. This resulted in the following correction factors due to the Swings effect:

$$\text{R(8) Ratio} = {}^{12}\text{CN}/{}^{13}\text{CN} = \frac{12.0244}{12.225} = 0.9836$$

$$\text{R(7) Ratio} = {}^{12}\text{CN}/{}^{13}\text{CN} = \frac{5.7507}{8.6418} = 0.6655.$$

Finally, the observed ratios of Table 4 are divided by these correction factors to obtain the true $^{12}\text{C}/^{13}\text{C}$ ratio in the comet. Using the R(8) lines the cometary $^{12}\text{C}/^{13}\text{C}$ ratio

is found to be 87.58 and 90.71 (the lines were measured separately twice each to determine errors present in the measurement process). The ratios found from the R(7) lines are 90.37 and 87.10. Averaging these results leads to a $^{12}\text{C}/^{13}\text{C}$ ratio of 88.9 ± 1.8 . The error bars are due to measurement error only and do not include any errors present due to the Swings model or the reduction of the data.

It is immediately apparent that this method of determining the $^{12}\text{C}/^{13}\text{C}$ ratio in a comet is far superior to the previously used method as there is much less error in the measurement of intensities (this is due solely to the fact that the R(7) and R(8) lines of ^{13}CN (0,0) are unblended at resolutions greater than $100 \text{ m}\text{\AA}$). It is also apparent that the determined value of $^{12}\text{C}/^{13}\text{C} = 88.9 \pm 1.8$ is in direct agreement with the value of 89 found from meteorites and from terrestrial samples, as well as from the solar photosphere and the atmospheres of Mars, Venus, and Jupiter (Owen (1973), Zucconi and Festou (1986), Hawkins and Jura (1987)). It thus appears that comets were formed in the solar nebula. According to Stawikowski and Greenstein (1964), they could not have come directly from material at the center of a star in which the carbon-nitrogen cycle had reached equilibrium, where $^{12}\text{C}/^{13}\text{C} \approx 4$, or from a star in which helium burning had occurred, where $^{12}\text{C}/^{13}\text{C}$ could be very large. The results also show that the solar nebula was extremely homogeneous with regards to these two stable isotopes of carbon. As discussed by Owen (1973), the present research lends further support against the formation of planetary ^{13}C by spallation reactions occurring in planetesimals as first envisioned by Fowler, Greenstein, and Hoyle (1962). Unfortunately, because of the homogeneity within the primordial solar nebula our results cannot be used to place constraints on the location (within the solar system) or time of formation of comets. Finally, it appears that the only possibility of variation in the $^{12}\text{C}/^{13}\text{C}$ ratio is if comets should ever arrive from outside the solar regime.

CHAPTER 7 THE GREENSTEIN EFFECT

7.1 EVIDENCE IN COMET P/HALLEY

Prior to the current research, the Greenstein effect has only been used once on four spectra coming from three different comets to establish gas velocities in the coma (Delsemme (1982)). As it is the purpose of this research to obtain velocity profiles of the cyanogen gas throughout the coma of P/Halley at the time of observation, the Greenstein effect was examined much more extensively than ever before. As discussed earlier, the R(7), R(8), R(9), R(12), R(13), and R(14) lines were used to examine the Greenstein effect. Referring to Figure 10, we define a local rectangular coordinate system in the coma centered on the nucleus (position 1, bin 9) with the Y-axis running from south to north and the X-axis from east to west. The selected R-branch line intensities were then measured for every spectral bin on the X-axis (using the 'e' keystroke of the IRAF SPLIT package) and at the central bin (bin 9) of every other spectral position.

An absolute spatial scale at the comet was established using the simple relationship $S = \Delta \theta$ (AU/pixel), where Δ is the cometary geocentric distance in astronomical units ($\Delta=0.44$ AU for all observations) and θ is the angle in radians of sky subtended by one pixel of the spectrum ($\theta=1''.4/\text{pixel}$). It was determined that $S = 450.1$ km/pixel, or that each bin corresponded to a spatial distance of 4,501 km at the comet. Due to the sampling method used, this results in a resolution along the X-axis of 4,501 km for the Greenstein effect and for any velocity profiles derived thereby. Because the spectra are separated by 4 minutes of arc along the Y-axis, the spatial resolution in this direction is only 77,163 km. It should also be noted that due to the trimming of the original spectra, there is a 16

arcsecond gap corresponding to 5,144 km between bins 1 and 17 of different neighboring spectra along the X-axis.

With the selected line intensities measured, the Greenstein effect was observed by calculating the three line ratios $R(8)/R(7)$, $R(9)/R(12)$, and $R(13)/R(14)$ at every measured point in the coma. Figures 31, 32, and 33 illustrate the observed Greenstein effect on the X-axis for each of the three ratios used. As Greenstein (1958) himself first noted, there is a definite variation in the line ratios on each side of the nucleus. These data will now be used to deconvolve the gas velocity profile in the coma of Comet P/Halley.

7.2 VELOCITY MAPS OF THE COMA

The first step in generating a velocity map from the observed Greenstein effect is to use the Swings effect computer model to produce a table of the predicted line ratios at different radial velocities. The observed line ratio is then used as an index into this table to obtain the radial velocity of the gas at a particular point. These radial velocities can finally be plotted to reveal the deconvolved velocity profile of the gas in the coma.

A value of $G = 3.701 \times 10^{-4}$ was used in the Swings effect model. The radial velocity was varied from 20 to 32 km/s with a step size of 0.01 km/s to produce the conversion table. The theoretical Greenstein effect table is graphically illustrated in Figure 34. It is immediately apparent that only the $R(9)/R(12)$ ratio can be used to obtain a velocity map of the gas in the coma since this is the only ratio of the three that increases monotonically throughout the pertinent range in radial velocity. Both of the $R(8)/R(7)$ and $R(13)/R(14)$ ratios would lead to ambiguities in radial velocity if used. This being the case, the $R(9)/R(12)$ ratio was used to obtain the gas velocity data tabulated in Table 5. Figure 35 depicts the gas velocities on the X-axis and Figure 36 is a map of the velocities on the Y-axis. The dotted line in each of these diagrams depicts the radial velocity of the comet's

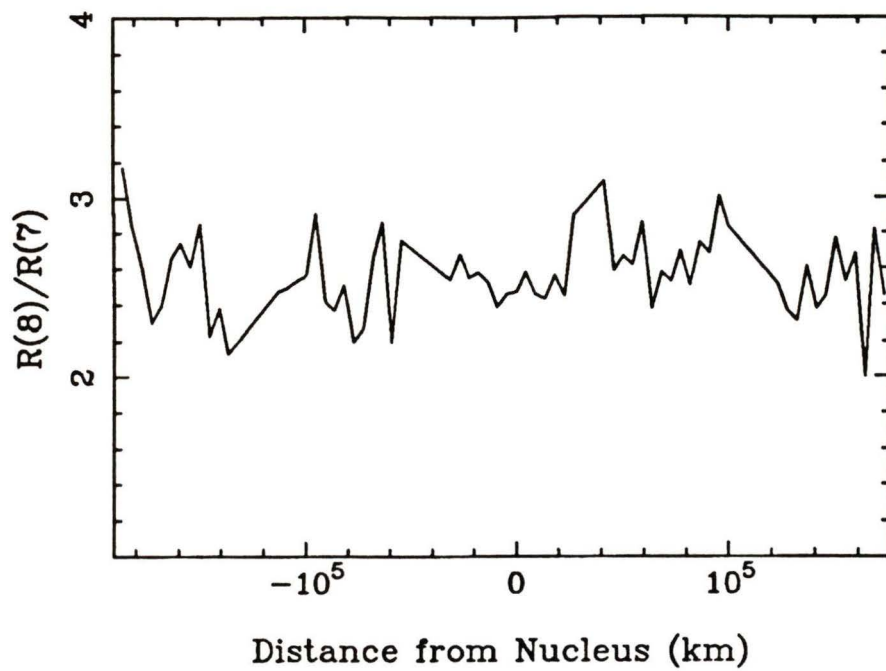


Figure 31 The Observed Greenstein Effect : $R(8)/R(7)$. The ratio of the R(8) and R(7) lines is shown for observations taken from east to west through the coma of P/Halley (spectral positions 1 through 5).

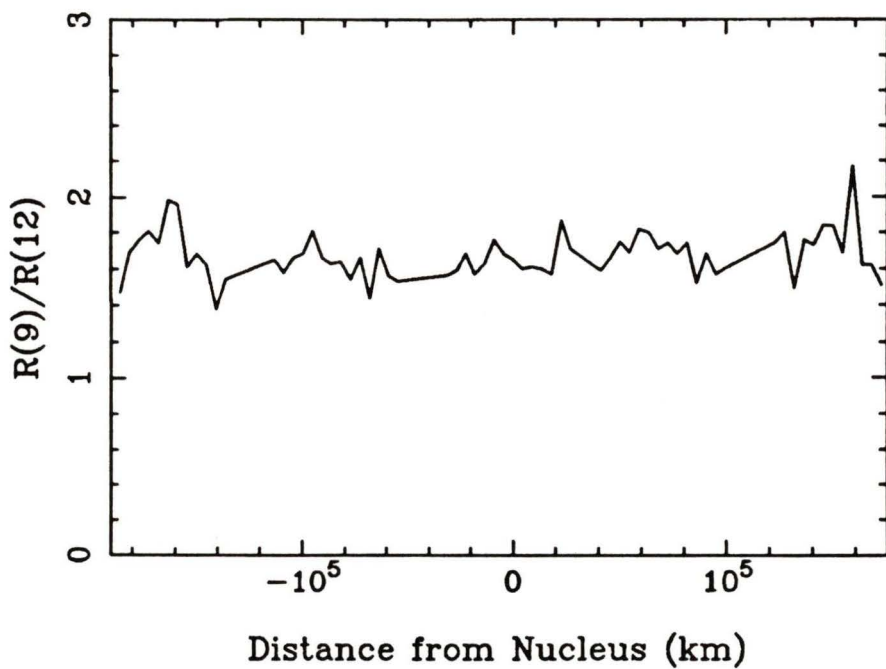


Figure 32 The Observed Greenstein Effect : $R(9)/R(12)$. The ratio of the R(9) and R(12) lines is shown for observations taken from east to west through the coma of P/Halley (spectral positions 1 through 5).

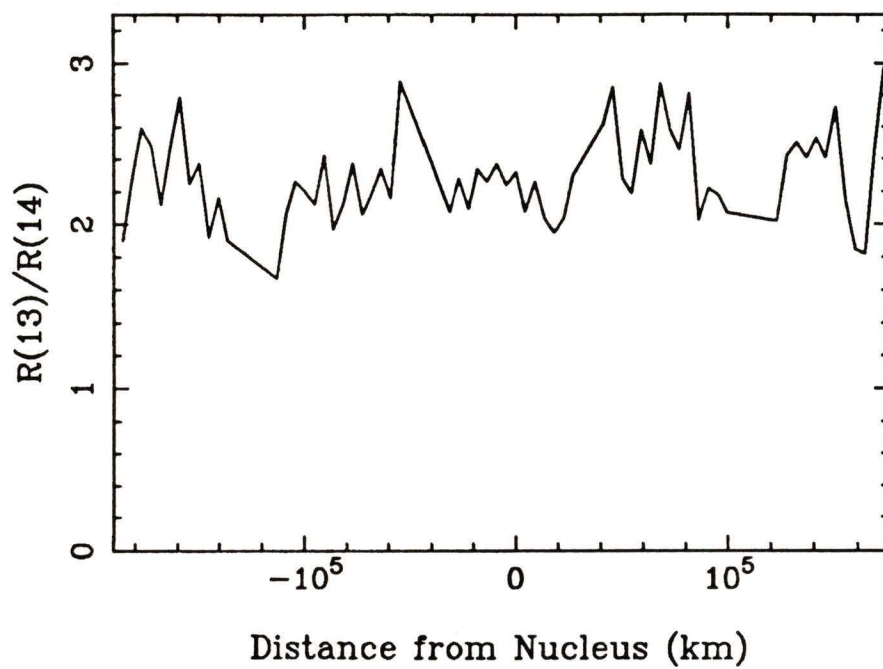


Figure 33 The Observed Greenstein Effect : $R(13)/R(14)$. The ratio of the R(13) and R(14) lines is shown for observations taken from east to west through the coma of P/Halley (spectral positions 1 through 5).

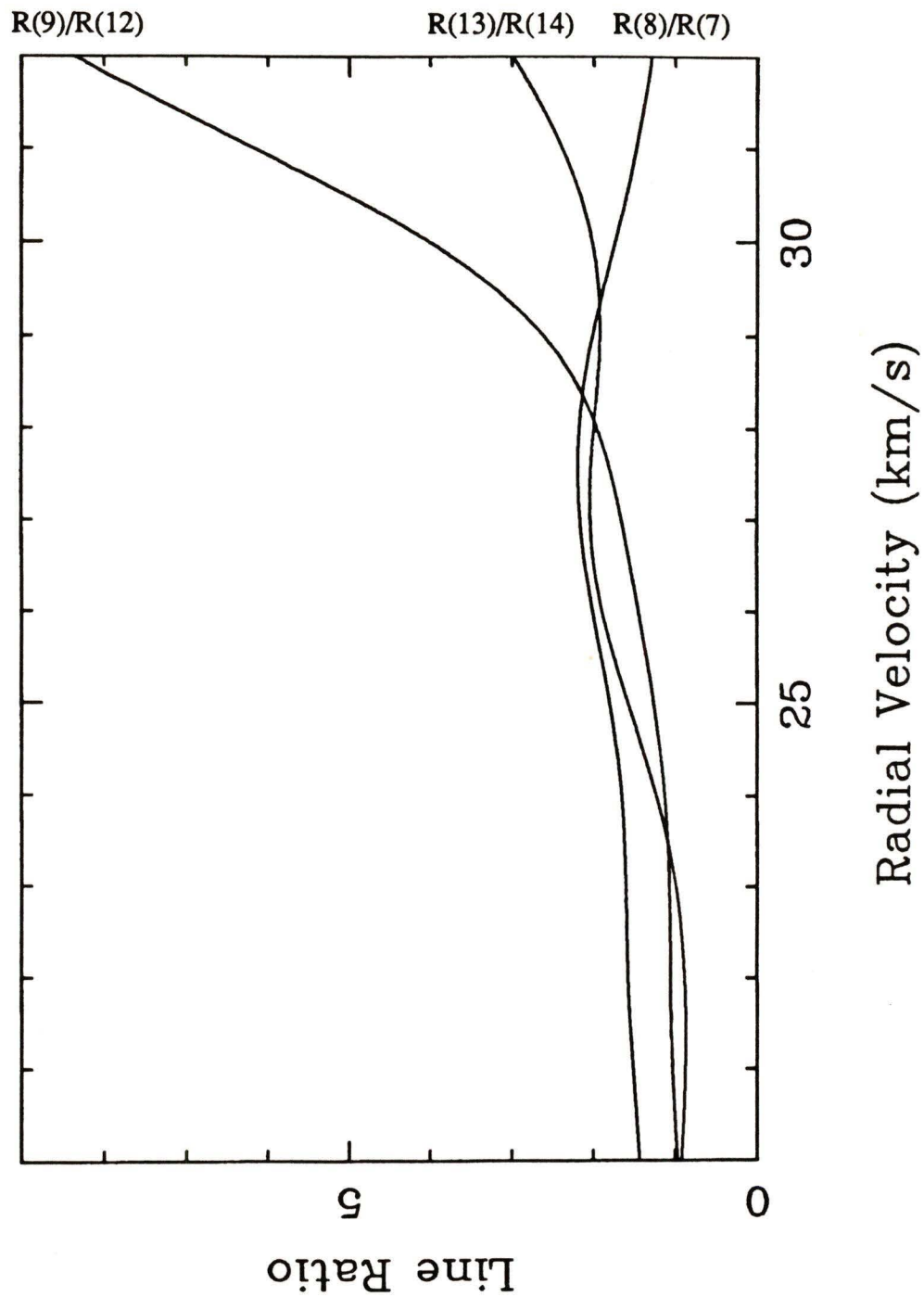


Figure 34 The Theoretical Greenstein Effect. The $R(8)/R(7)$, $R(9)/R(12)$, and $R(13)/R(14)$ ratios are shown calculated for radial velocities between 20 and 32 km/s. It can be seen that only the $R(9)/R(12)$ ratio is monotonically increasing throughout this range in radial velocity.

Table 5. The Observed Greenstein Effect

X (km)	Y (km)	R(9)/R(12)	Radial Velocity (km/s)
-185833.19	0.00	1.47	26.14
-181332.05	0.00	1.69	27.16
-176830.89	0.00	1.76	27.43
-172329.73	0.00	1.81	27.60
-167828.59	0.00	1.74	27.36
-163327.44	0.00	1.98	28.065
-158826.30	0.00	1.96	28.02
-154325.14	0.00	1.61	26.815
-149823.98	0.00	1.68	27.12
-145322.84	0.00	1.62	26.86
-140821.69	0.00	1.38	25.685
-136320.55	0.00	1.54	26.485
-113171.77	0.00	1.65	26.99
-108670.62	0.00	1.58	26.675
-104169.47	0.00	1.66	27.035
-99668.32	0.00	1.68	27.12
-95167.17	0.00	1.81	27.60
-90666.02	0.00	1.66	27.035
-86164.87	0.00	1.63	26.91
-81663.72	0.00	1.64	26.95
-77162.57	0.00	1.54	26.485
-72661.42	0.00	1.66	27.035
-68160.27	0.00	1.44	25.99
-63659.12	0.00	1.71	27.24
-59157.97	0.00	1.56	26.58
-54656.82	0.00	1.53	26.435
-31508.05	0.00	1.56	26.58
-27006.90	0.00	1.59	26.72
-22505.75	0.00	1.68	27.12

Table 5 (continued). The Observed Greenstein Effect

X (km)	Y (km)	R(9)/R(12)	Radial Velocity (km/s)
-18004.60	0.00	1.57	26.63
-13503.45	0.00	1.63	26.91
-9002.30	0.00	1.76	27.43
-4501.15	0.00	1.68	27.12
0.00	0.00	1.65	26.99
4501.15	0.00	1.60	26.77
9002.30	0.00	1.61	26.815
13503.45	0.00	1.60	26.77
18004.60	0.00	1.57	26.63
22505.75	0.00	1.87	27.78
27006.90	0.00	1.71	27.24
41153.37	0.00	1.59	26.72
45654.52	0.00	1.66	27.035
50155.67	0.00	1.75	27.39
54656.82	0.00	1.69	27.16
59157.97	0.00	1.82	27.63
63659.12	0.00	1.80	27.57
68160.27	0.00	1.71	27.24
72661.42	0.00	1.74	27.36
77162.57	0.00	1.68	27.12
81663.72	0.00	1.74	27.36
86164.87	0.00	1.52	26.39
90666.02	0.00	1.68	27.12
95167.17	0.00	1.57	26.63
99668.32	0.00	1.60	26.77
122817.09	0.00	1.74	27.36
127318.24	0.00	1.80	27.57
131819.39	0.00	1.49	26.24

Table 5 (concluded). The Observed Greenstein Effect

X (km)	Y (km)	R(9)/R(12)	Radial Velocity (km/s)
136320.55	0.00	1.76	27.43
140821.69	0.00	1.73	27.32
145322.84	0.00	1.84	27.70
149823.98	0.00	1.84	27.70
154325.14	0.00	1.69	27.16
158826.30	0.00	2.17	28.43
163327.44	0.00	1.62	26.86
167828.59	0.00	1.62	26.86
172329.73	0.00	1.51	26.34
0.00	77162.57	1.84	27.70
0.00	154325.13	1.55	26.535
0.00	-77162.57	1.50	26.29
0.00	-154325.13	1.95	27.99
-77162.57	77162.57	1.92	27.92
77162.57	77162.57	1.68	27.12
-77162.57	-77162.57	1.73	27.32
77162.57	-77162.57	1.96	28.02

nucleus at the time of the observations (+26.37 km/s). The error in velocity due to measurement errors in line intensities only is estimated at ± 0.12 km/s.

From Figure 35 it can be seen that the velocity of the cyanogen gas across the coma of the comet perpendicular to the head-tail orientation has remarkable structure. The velocity of the gas changes by as much as 1.57 km/s within a spatial distance of 4501 km (the spatial resolution of the velocity map). The overall velocity flow appears to be higher than the nuclear radial velocity with regions of very high flow superimposed over the general expanding motion of the gas. A possible explanation of these high flow regions as being due to cyanogen gas jets will be examined later.

Figure 36 depicts the gas motion along the Y-axis. It can be seen that near the head of the comet (to large negative values of Y) the gas has a large radial velocity directed away from the sun. This is probably due to the gas interacting with the solar wind. Further inside the coma where the gas molecules would be less affected by the solar wind, the flow velocity drops to below that of the nucleus (as expected if the gas is radially streaming outwards from the nucleus) and then increases steadily as the observer looks towards the tail. Finally, the gas flow seems to slow down at large positive Y values. This last observation is most likely due to the fact that the position angle of the plasma tail was $351^{\circ}.16$ (ie. $8^{\circ}.84$ west of north) at the time of the observation. At large distances from the nucleus (along the positive Y-axis) the accelerating effect of the plasma tail on the cyanogen gas molecules would be decreased as a result of this alignment.

In order to interpret Figure 35 better and to gain an insight on the effect of different velocity fields on the observed Greenstein effect, we will now proceed to model the Greenstein effect.

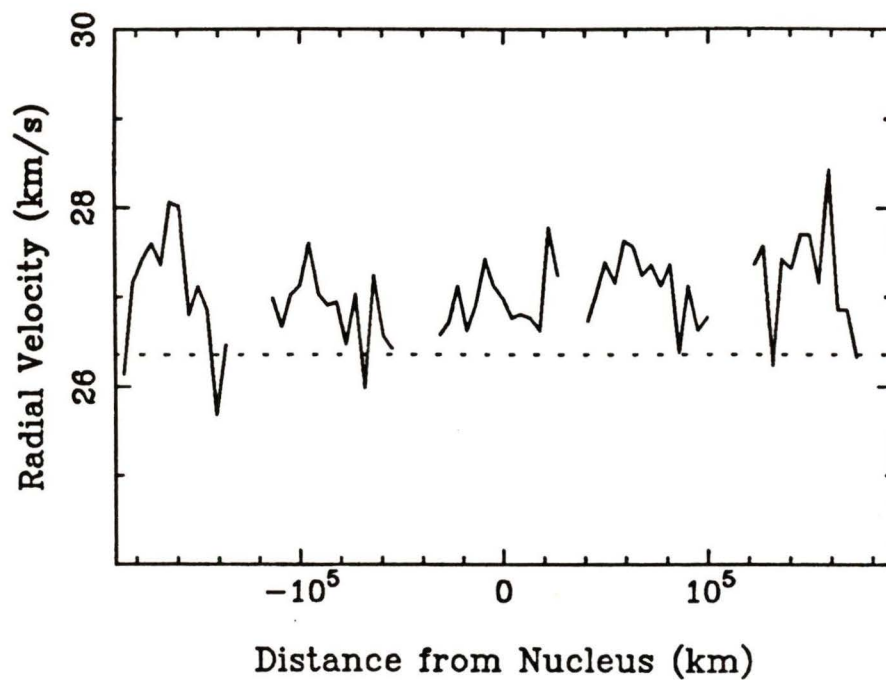


Figure 35 *East-West Velocity Map of Coma Gas*. The data of Table 5 are plotted for the gas velocities in the coma of Comet P/Halley on the X-axis (ie. for spectral positions 1 through 5). The dotted line represents the nucleus' motion.

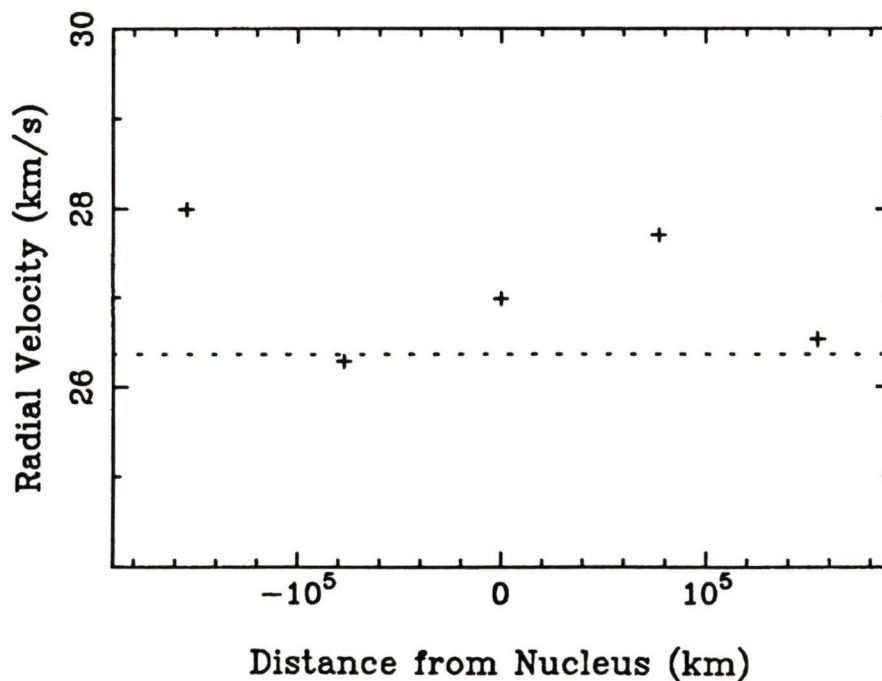


Figure 36 *North-South Velocity Map of Coma Gas*. The data of Table 5 are plotted for the gas velocities in the coma of Comet P/Halley on the Y-axis (ie. for the central bin (bin 9) of spectral positions 1 and 6 through 9). The dotted line represents the nucleus' motion.

7.3 MODELING: A FIRST APPROACH

In the previous section, we had observations of the ratio $R(9)/R(12)$ throughout the coma of Comet P/Halley and proceeded to produce maps of the velocity field in the coma by matching our observed ratios with their corresponding radial velocity as pre-computed. We shall now attempt to solve the reverse problem. Given a pre-determined velocity field we will calculate the $R(9)/R(12)$ ratio as seen by an observer (ie. the Greenstein effect). We shall start by assuming spherical symmetry of the coma velocity field and use the same parameters as were the case for our observations of Comet P/Halley ($G=3.701 \times 10^{-4}$, radial velocity (nucleus) = +26.37 km/s, and heliocentric distance of comet = 1.40 AU). Note that these parameters are used solely as a matter of convenience and are not meant to imply that the models reflect the conditions at the time of our previous observations.

Figure 37 depicts the geometry of the model. A rectangular coordinate system is used with the observer and sun located perpendicular to the X-axis. At any point in the coma, a gas particle will have a velocity $V(x,y)$ with a direction angle of $\Psi(x,y)$. At a fixed Y value the observer sees a given Greenstein effect which is a contribution of all the fluorescing gas elements along the line of sight through the coma. Each gas element may be moving in a different direction at a different speed. Assuming a constant density of gas throughout the coma and a constant heliocentric distance of all the gas elements, the radial velocity is the only parameter which affects the fluorescence of a gas element through the Swings mechanism. If we denote the intensity ($W \text{ sr}^{-1}$ of a single molecule) to be $j(G, r, \dot{r}_0 + V \cos\Psi)$, that is the element's intensity is determined by the Swings effect model with parameters G , heliocentric distance, and radial velocity (nucleus plus gas element), then the Greenstein effect at a given Y coordinate may be determined from

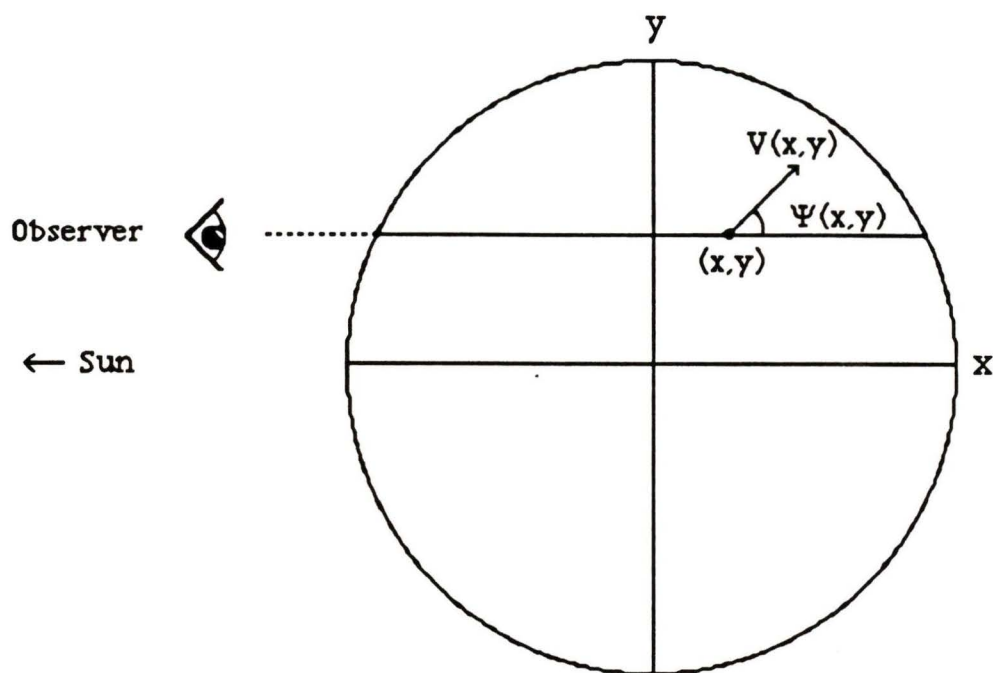


Figure 37 The Geometry of the Greenstein Models. The geometry used to model the Greenstein effect is depicted. A two-dimensional cross section of the spherical coma of the comet is placed on a rectangular coordinate system as shown with the observer and sun located at $x < -a$, where a is the radius of the coma. At any point within the coma, the gas molecules have a velocity $V(x,y)$ with a direction angle of $\Psi(x,y)$. This geometry allows both spherical and cylindrical symmetry velocity flows to be modeled.

$$I(y) = \int_{x=-\sqrt{a^2 - y^2}}^{\sqrt{a^2 - y^2}} j(G, r, \dot{r}_0 + V \cos\Psi) n(x,y) dx \quad (27)$$

where a is the radius of the coma, $n(x,y)$ is the number density of the gas at the point (x,y) in the coma, and $I(y)$ are the returned R-branch line radiances ($\text{W m}^{-2} \text{sr}^{-1}$) as seen by the observer (from which the R(9)/R(12) Greenstein effect is derived). With this formulation different models may be examined simply by changing the values of V , $\cos\Psi$, and $n(x,y)$.

We shall start with a very simple velocity flow model in which the gas is expanding symmetrically away from the nucleus with a constant radial speed V . In this case, the model parameters are:

$$\begin{aligned} V(x,y) &= V \\ \cos \Psi &= \frac{x}{\sqrt{x^2 + y^2}} \end{aligned}$$

and $n(x,y) = 1$.

Expansion velocities V of 1 and 10 km/s were tried with the results depicted in Figure 38. The resulting Greenstein effect is asymmetric, especially at higher expansion velocities.

Another simple model was tried next in which the gas rotated around the comet's nucleus as a disk with constant angular speed Ω . The parameters used were

$$\begin{aligned} V(x,y) &= \left(\frac{\sqrt{x^2 + y^2}}{a} \right) \Omega \\ \cos \Psi &= \frac{y}{\sqrt{x^2 + y^2}} \end{aligned}$$

and $n(x,y) = 1$,

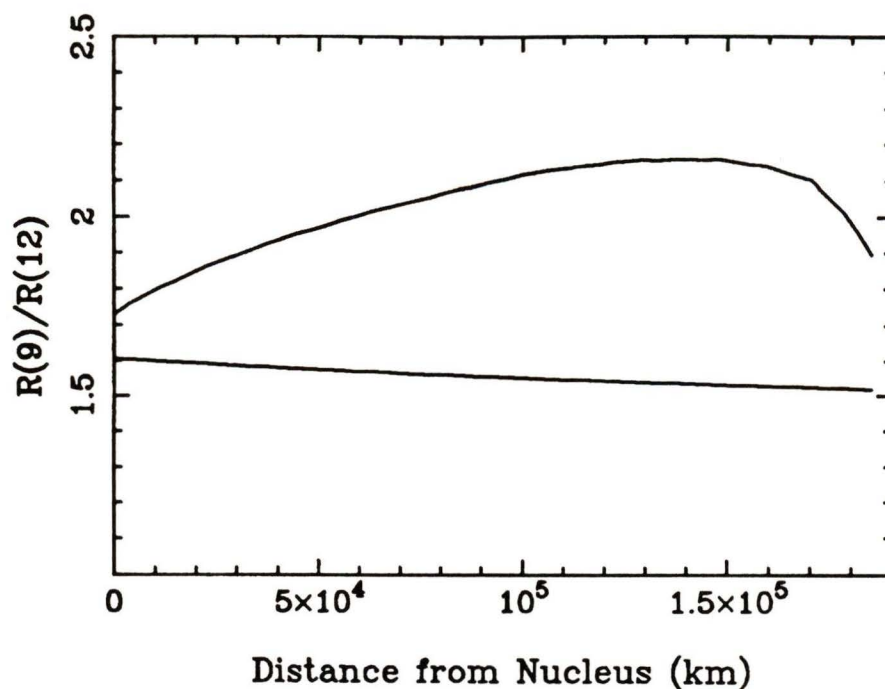


Figure 38 Symmetric Radial Gas Flow. The $R(9)/R(12)$ ratio is modeled assuming that the cyanogen gas is expanding symmetrically away from the nucleus with a constant radial speed. The top line corresponds to a radial speed of 10 km/s and the bottom, gently sloping line is for a speed of 1 km/s.

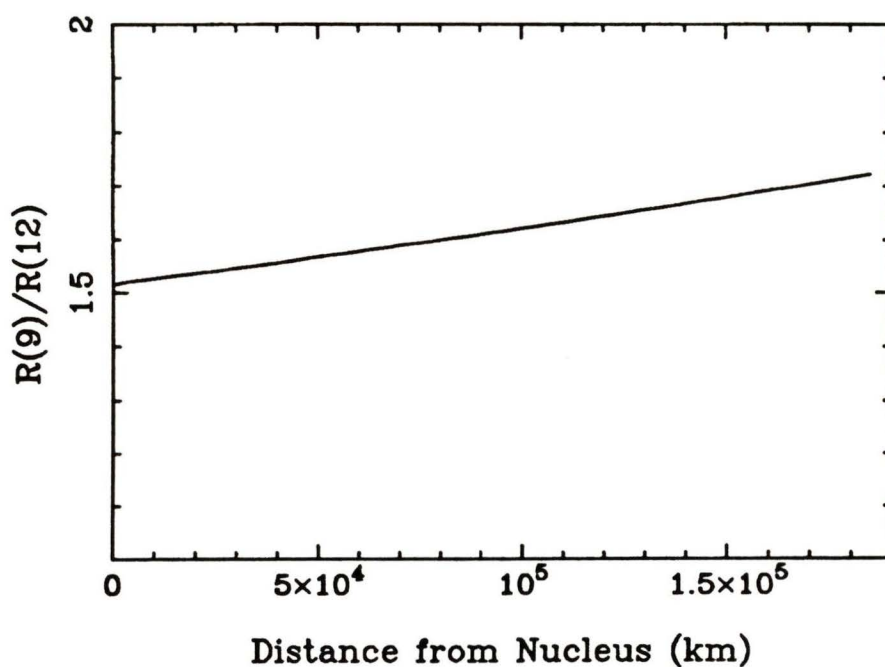


Figure 39 Rigid Rotational Gas Motion. The $R(9)/R(12)$ ratio is modeled assuming that the cyanogen gas is rotating around the nucleus as a disk with a constant angular speed of 1 km/s.

where a is the radius of the coma (200,000 km) and a value of $\Omega = 1.0$ km/s was used. The results are depicted in Figure 39 and again indicate a high asymmetry in the observed Greenstein effect on each side of the nucleus (which was not observed in Comet P/Halley).

7.4 MODELING WITH A SPACE DENSITY PROFILE AND CYANOGEN JETS

In reality, the density of the cyanogen gas in the coma is not constant but decreases with distance from the nucleus. We shall use the relationship found in Chapter 2 for the space density of the gas, namely

$$n(\rho) = \frac{44,407}{\rho^{1.456}},$$

where ρ has units of kilometers ($\rho = (x^2 + y^2)^{1/2}$) and $n(\rho)$ is in units scaled to match the observed space densities found for Comet IRAS-Araki-Alcock. This density relationship is in effect a weighting factor (see Equation 27) which reflects the fact that the velocity of a gas element with a high density will contribute more to the observed Greenstein effect than the velocity of a low-density gas element along the line of sight through the coma.

We shall again use a general radial expansion model of the gas motion in the coma ($V = 1$ km/s) in addition to the varying cyanogen density. The resulting difference in the observed Greenstein effect is shown in Figure 40. The solid line depicts the case with a constant gas density whereas the dotted line shows the affect of using a varying gas density. As can be seen, the asymmetry in the observed Greenstein effect is lessened with the addition of a varying density profile. The drop in the $R(9)/R(12)$ ratio very close to the nucleus is due to extrapolating the density function beyond its region of applicability. The sharpness of the change is an aliasing artifact due to the improper sampling of Equation 27 both along the line of sight through the coma ($dx = 1500$ km) and across the coma ($dy = 3700$ km).

It is well known that the gas and dust in a comet's coma is not emitted uniformly from the nucleus, but rather in bursts from isolated regions on the sunward side of the nucleus (Whipple (1982), Mendis et al (1985), Grün et al (1986), Levasseur-Regourd et al (1986), Sekanina and Larson (1986), Reinhard (1987), Sagdeev et al (1987)). With the passage of the Giotto spacecraft through the coma of Comet P/Halley, jets of gas have been photographed leaving the sunward side of the comet's nucleus. A'Hearn et al (1987) imaged P/Halley in the light of the CN radical. They found three prominent gas jets emanating from the nucleus. Thus, it is well established that the observed cyanogen gas is not uniformly emitted but rather confined to jets emanating from the nucleus. In fact, many astronomers now believe that the inner coma consists of nothing but these jets of dust and gas. The simple models tried up to this point do not show the sharp peaks and valleys observed in the Greenstein effect of Comet P/Halley (see Figure 35). The observed cyanogen gas jets will now be included into the models in order to see if they can explain the structure seen in the Greenstein effect.

To model the jets we shall assume, as described by Larson et al (1984) and Sagdeev et al (1987), that jets appear on the dayside of the nucleus with activity starting at sunrise and lasting until sunset. Jets are included in the computer model of the Greenstein effect by first creating a coordinate map of their distribution through the coma. The coordinate system is an exact duplicate of that used in evaluating Equation 27. The coordinate map itself is produced by assuming a number of jet sources on a two-dimensional cross-section of the comet's nucleus and then rotating the comet clockwise for a given interval. The gas is assumed to emanate radially from the comet's surface at a given speed while the jet source is exposed to sunlight. Thus, at the end of the pre-determined time interval, the gas jets will have traced out Archimedean spirals in the coordinate map. This coordinate map is

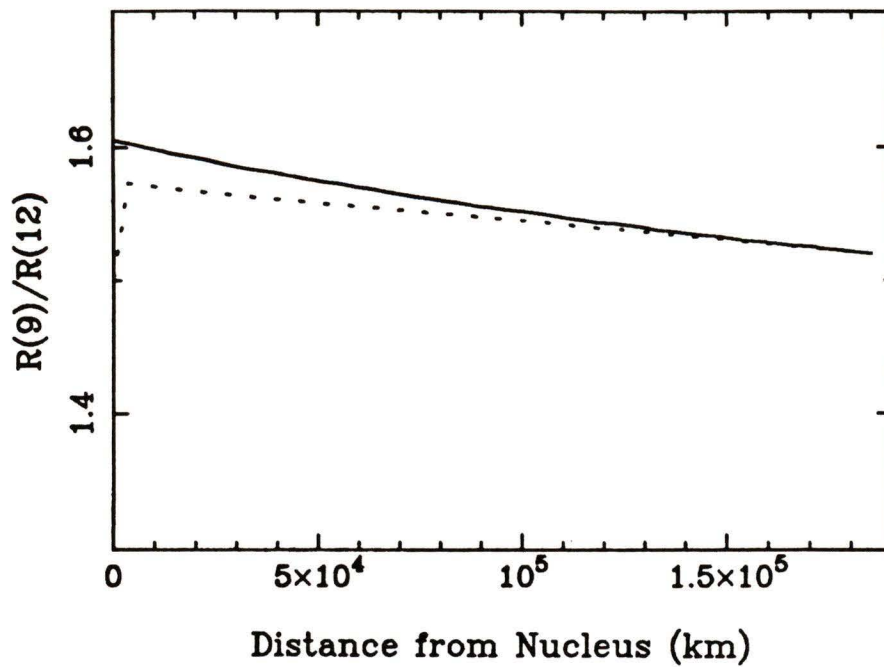


Figure 40 Addition of a Space Density Profile. The $R(9)/R(12)$ ratio is modeled assuming that the cyanogen gas is expanding symmetrically away from the nucleus with a radial speed of 1 km/s (as depicted by the solid line above). The dotted line shows the effect of adding a varying gas density through the coma to the same model.

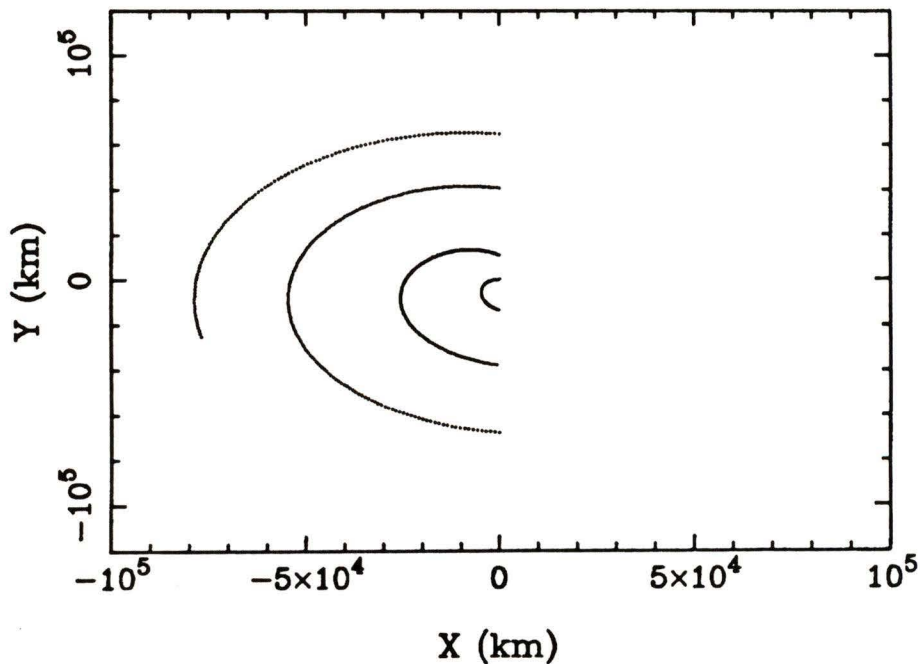


Figure 41 The First Jet Coordinate Map. The locations of cyanogen jets in the coma are graphically depicted. The rectangular coordinate system is identical to that used in the Greenstein models.

then used by the computer model as it evaluates the contribution of gas elements in the coma to the Greenstein effect through Equation 27.

The first coordinate map was created by assuming a 10.3 hour spin period of the nucleus of P/Halley (Whipple (1982)) with 2 jet sources located on the comet's surface and is shown in Figure 41. The nucleus was allowed to rotate 1.5 times around and the jet velocity was 1.5 km/s. The previous model of the Greenstein effect was used as a starting point (varying gas density with a background, uniform radial gas expansion velocity of 1.0 km/s). The gas jets were then incorporated into this model by adding a 0.5 km/s radial velocity to gas elements that were within 4,000 km of a jet. The numbers were chosen arbitrarily as the detailed characteristics of gas jets in comets are still unknown. The computed Greenstein effect for this model is illustrated in Figure 42. Small-scale variations in the $R(9)/R(12)$ ratio have been introduced where the line of sight through the coma intersects the gas jets.

In order to improve the realism of our models, we next altered the role of gas jets in the coma from the simple velocity enhancement used above. We used the same jet coordinate map as before but now added more sophisticated velocity effects as well as density effects to the jets. As the cyanogen gas is known to be concentrated in jets, it is only logical that the jets should have a higher density of gas than the general background. As a first step in realizing this, we multiplied the density of a gas element by 10 if it was considered to be in a jet. This factor was again arbitrarily chosen as we are aware of no statistics from theory or observation having yet been published on the physical parameters of cometary gas jets. In addition, the general gas density relationship of Chapter 2 was truncated to $n(\rho) = 3$ for $\rho \leq 731.5$ km in order to avoid the extrapolation effect discussed previously. Delsemme (1982) states, based on theory and observation, that the expansion velocity of CN from the cometary nucleus is given (in km/s) by

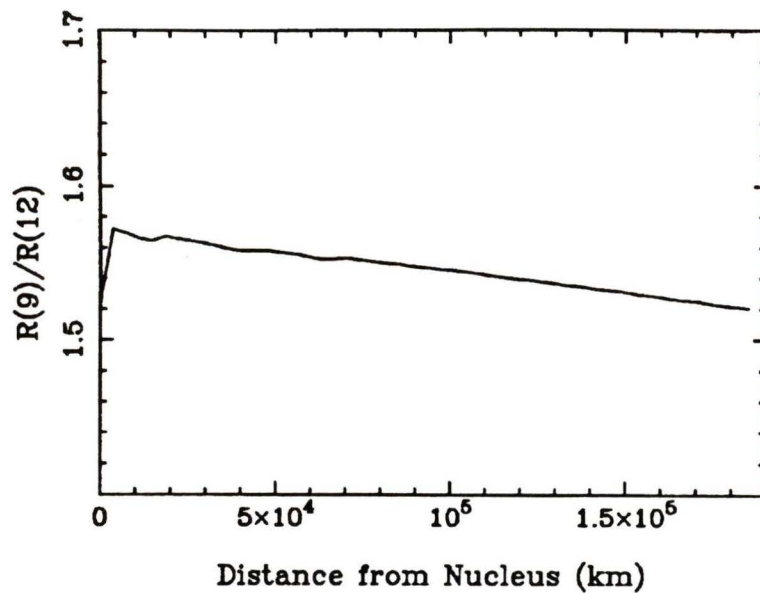


Figure 42 Addition of Cyanogen Jets. The Greenstein effect is modeled for a uniform radial gas expansion of 1 km/s and a varying gas density. In addition, cyanogen gas jets are included in the model by assuming that gas elements within 4,000 km of a jet (Figure 41) have an additional expansion radial velocity of 0.5 km/s.

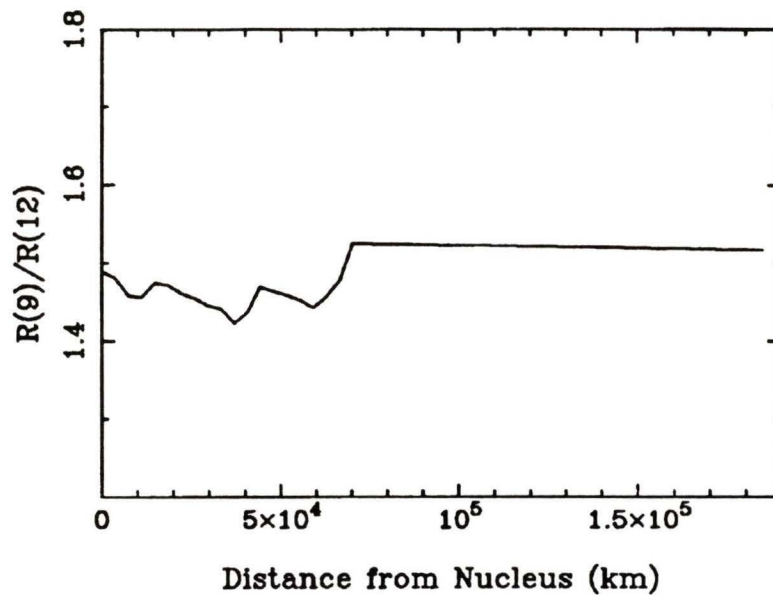


Figure 43 Jet Size, Density, and Velocity Effects. The Greenstein effect is computed assuming the parameters of the previous model (depicted in Figure 42) in addition to increasing the density of a gas element if it is within a jet, increasing the size of the jet as its distance from the nucleus increases, and changing the expansion velocity of gas elements depending on their position within a jet. Note that the general expansion velocity of the gas has also been lowered from 1.0 to 0.49 km/s.

$$v_{\text{CN}} = (0.58 \pm 0.03) r^{-0.5} ,$$

where r is the heliocentric distance of the comet in AU. For $r = 1.40$ AU this implies that the expansion velocity is 0.49 km/s. This velocity was used as the general radial outflow velocity. As before, the velocity of a gas element was increased if it was determined to be inside a jet. Because of slight differences in the velocities of ejected gas molecules, a jet tends to increase in size as its distance from the nucleus increases. This effect can be seen in the cyanogen jets imaged by A'Hearn et al (1987) in Comet P/Halley. To emulate this, the size of a jet was approximated by the simple (arbitrarily chosen) formula

$$TOL = \frac{2\rho}{15} ,$$

where ρ is the distance in kilometers from the nucleus and TOL is the tolerance determining when a gas element is considered to be in a jet (if the element's distance from a coordinate map jet is less than TOL and the element is closer to the nucleus than the coordinate map jet then that gas element is influenced by the jet). Finally, the additional radial velocity added to a gas element if it is determined to be in a jet must vary depending on the location of the element within the jet. This effect is modeled by the equation (again arbitrarily chosen)

$$EXTRA = \frac{2.5}{e^{\text{CLOSE/TOL}}} \text{ km/s} ,$$

where $CLOSE$ is the distance of the gas element from the coordinate map jet in kilometers and $EXTRA$ is the additional radial velocity which is to be added. Thus, the jets have velocity structure with the leading edge of a jet (corresponding to the coordinate map points) having the greatest velocity. Figure 43 depicts the results of this model. Note that there is more structure to the observed Greenstein effect than previously but that the variation is still quite small. This variation, due to the modeled jets, ends abruptly once the region containing the jets is passed.

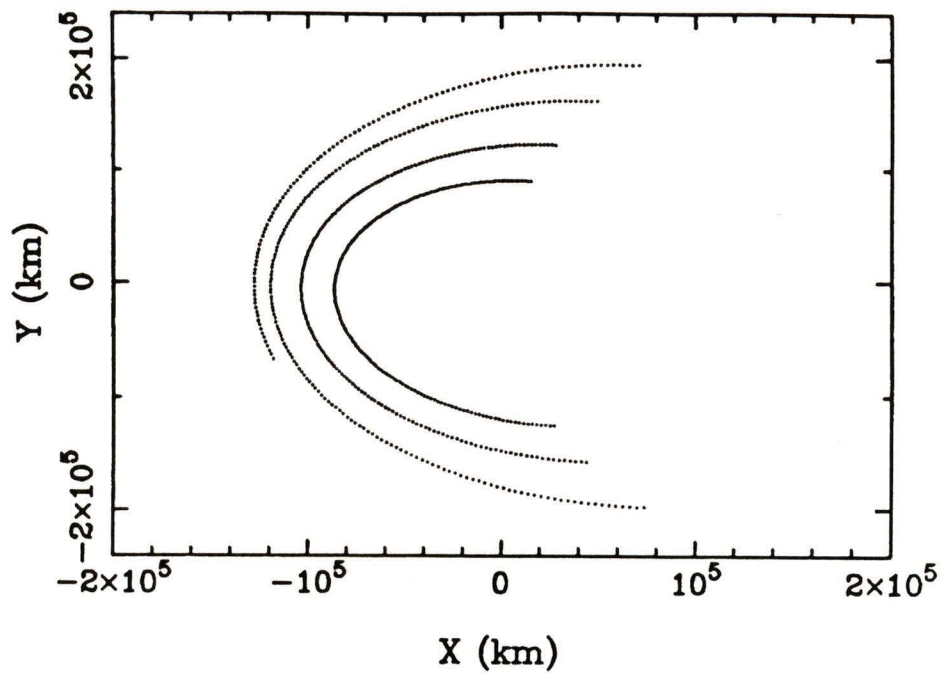


Figure 44 *The Second Jet Coordinate Map.* The locations of cyanogen jets in the coma are illustrated. The jets in this map extend over a larger area than in the first map (Figure 41).

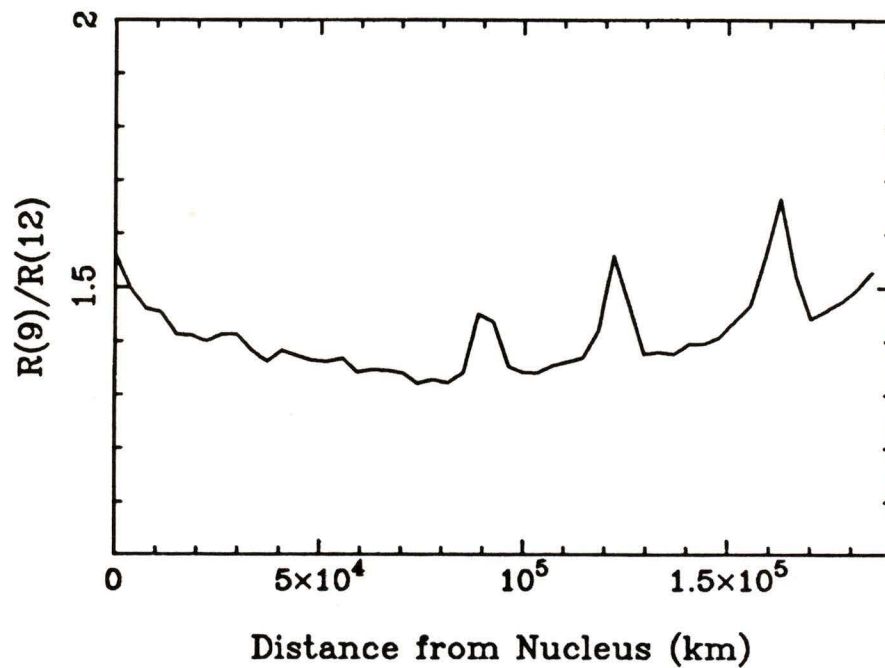


Figure 45 *Variable Jet Density and a Preliminary Solar Wind.* The Greenstein effect is computed assuming that the cyanogen jets in the coma are distributed according to Figure 44. A variable jet density was added such that the density at a jet's center is 100 times greater than the general background gas density but only 10 times greater at the jet's boundaries. A simple solar wind was also added which altered a gas element's radial velocity by 0.3 km/s.

In order to extend the region of influence of jets in the coma, our next model used the different coordinate map depicted in Figure 44. This map was created by using 2 jet sources and rotating the nucleus 3 times around. In addition, the jets had a gas velocity of 2.0 km/s and were affected by a "solar wind". The solar wind was modeled by increasing the X-coordinate of a jet according to

$$x_{\text{new}} = x_{\text{old}} + \frac{1}{2} g T^2 ,$$

where g is the acceleration due to the solar wind (0.015 m/s^2), and T is the time the particle was moving during the whole simulation.

As well as using a new jet coordinate map, the model added a varying density effect to a jet so that the gas was 100 times denser at a jet's center than its surroundings while only 10 times denser at its boundaries. The jet velocity was also increased to a maximum of 4 km/s at the leading edge and the varying size of a jet was decreased to half of its previous value. In addition, the step size of integration along the line of sight through the coma, dx , was decreased from 1500 km to 900 km. Finally, a preliminary "solar wind" was added to the model (a more comprehensive study of the effect of adding a solar wind to the models will be given in the next section). This was a very simple wind which decreased a gas element's radial velocity by 0.3 km/s if $x < 0$ km, or increased it by 0.3 km/s if $x \geq 0$ km.

The results of this model are shown in Figure 45. Three peaks in the observed $R(9)/R(12)$ ratio are now clearly visible and occur where the line of sight through the coma is aligned with a jet. In other words, when the line of sight happens to be along an extended region of a jet, that jet's influence on the observed Greenstein effect is notably increased. The slight curvature of the overall line intensity ratio is due to the addition of the simple solar wind to the model as the next section will demonstrate.

Until now, the jet coordinate maps used have been rather simplistic with only 2 active jet sources expelling gas. The photographic images of the nucleus of P/Halley returned by the European Space Agency's Giotto spacecraft show that in reality many more jet sources are active at the same time. The author is aware of one such image showing up to 8 jets emanating from the nucleus. As a result, the jet profile was changed once more to reflect a coma composed primarily of gas jets. Five jet sources were used with each source having two or three sub-sources (ie. the jets are not isolated but occur in small clusters). The nucleus was rotated by 430° with a rotation period of 52.5 hours (Sekanina and Larson (1984)). The jets also had differing velocities of either 1.5, 1.6, or 1.8 km/s and a small solar wind was added as previously but with $g = 0.006 \text{ m/s}^2$. Figure 46 shows the resulting coordinate map.

Besides using this new map of cyanogen jets in the coma, our next model was extended so that the observed Greenstein effect was calculated from $Y = -185,000 \text{ km}$ to $+185,000 \text{ km}$. The integration step size along the line of sight through the coma, dx , was once again decreased from 900 km to 300 km. There were also no solar wind effects directly in the model. Finally, the radial expansion velocity of the gas was changed back to 1.0 km/s with a maximum of 3.0 km/s being added to this velocity if a gas element was determined to be inside a jet. All other model parameters and conditions are the same as in the previous model. The calculated observed Greenstein effect is illustrated in Figure 47. As an indication of this model's computational complexity, it took an IBM 370 computer running at night one hour and forty minutes to produce the results depicted in Figure 47! The results indicate an overall constant Greenstein effect overlaid with small scale variations. The plateaus occur where there are no jet alignments along the line of sight through the coma.

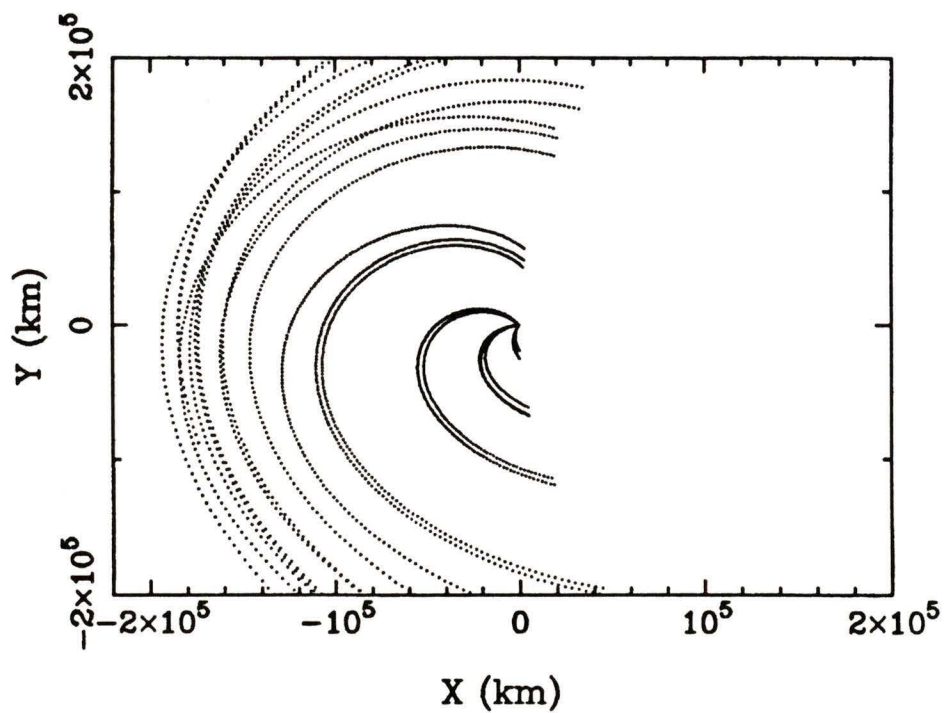


Figure 46 The Third Jet Coordinate Map. The locations of gas jets in the coma are depicted. This map is the result of using 13 individual jet sources which are grouped in clusters of two or three.

With the velocity flow models used to calculate the observed Greenstein effect, we can draw some temporary conclusions. Firstly, it must be noted that the Greenstein effect itself is a product solely of internal motions within the gas in a comet's coma. It cannot be duplicated by assuming other physical causes such as a variable "temperature" throughout the coma since the coma is never in thermal equilibrium (except perhaps in the innermost nuclear regions) but rather radiates due to a pure fluorescence of the solar radiation. It is because of this that the Greenstein effect is regarded as the most accurate and reliable technique available for establishing the expansion velocity of the cometary gas (Delsemme (1982)). In addition, a small scale velocity variation is magnified into a very detectable Greenstein effect due to the sharpness and sheer number of Fraunhofer lines in the spectral region of the CN (0,0) violet system. The observed Greenstein effect in Comet P/Halley (Figure 35) shows many sharp peaks and valleys superimposed over a rather constant R(9)/R(12) line ratio. It has been found through the simple models used herein that this overlying complexity can be explained by assuming velocity and density perturbations from a general radial gas expansion model. These perturbations are most easily explained by including gas jets in the models whose presence has been observed and known about for several years now.

7.5 ADDITION OF A SOLAR WIND TO THE MODELS

It is well established that the solar wind plays an important role in cometary physics. Most noticeable is the creation of the ion tail which always points away from the sun, but the solar wind also influences the coma of a comet. It was found previously that the addition of a simple wind affecting every gas molecule in the coma caused a slight curvature in the underlying R(9)/R(12) ratio across the coma. Our final model will attempt to incorporate the solar wind by assuming that gas molecules in the coma collide elastically

with the protons in the solar wind to a degree that depends upon the molecules' proximity to the nucleus. The gas molecules that are further from the nucleus should be affected more than those that are sheltered close to the comet nucleus. These elastic collisions can be included in the model simply by changing the direction of a gas molecule's motion according to

$$\cos \Psi = \frac{(x + \text{BEND})}{\sqrt{x^2 + y^2}},$$

where

$$\text{BEND} = e\rho/\text{SHOCK}$$

and *SHOCK* is a constant. We used *SHOCK* = 15,000 which results in noticeable solar wind effects at distances greater than 100,000 km from the nucleus. The model was also changed so that the integration step size $dx = 900$ km (to speed up the calculations), the jets had a maximum additional radial velocity of 5.0 km/s, and the maximum density at the center of a jet was 500 times that of the surrounding background gas. Figure 48 shows the calculated Greenstein effect for this final model. The high curvature of the R(9)/R(12) ratio is a direct result of the solar wind inclusion to the model. As this is not observed in P/Halley, we must assume that the solar wind does not penetrate as deeply as it does in the model into the coma. More striking is the scale of detail in the peaks and valleys of the model which closely resemble the observed Greenstein effect of Figure 32.

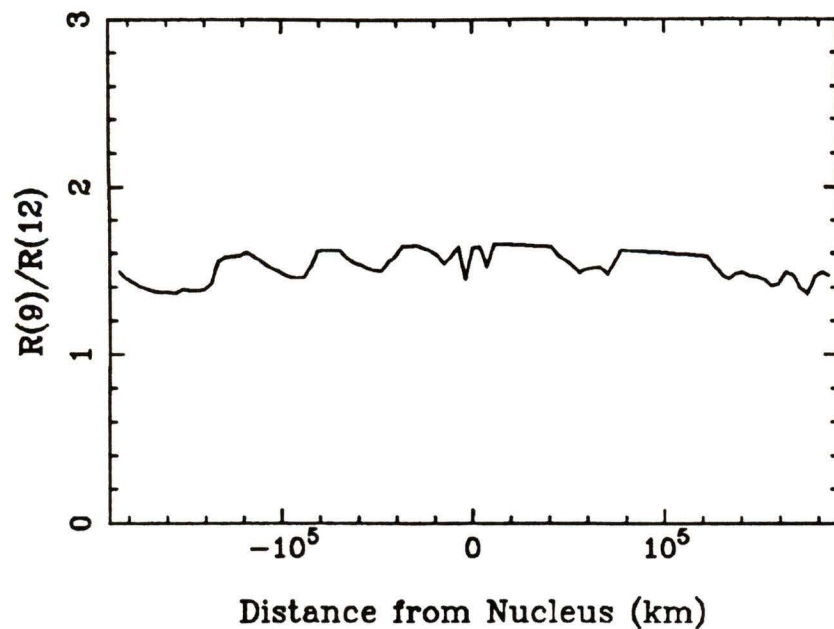


Figure 47 An Accurate Integration Model. The third jet coordinate map is used to calculate the observed $R(9)/R(12)$ ratio. The integration step size along the line of sight through the coma, dx , was decreased from 900 to 300 km. There are no solar wind effects in the model and the general radial gas expansion speed is 1.0 km/s.

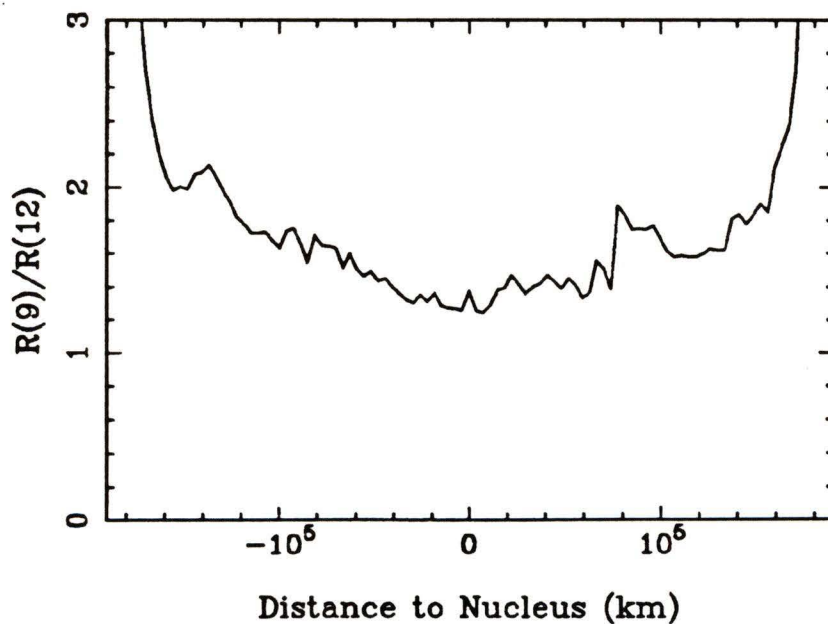


Figure 48 Addition of a Solar Wind. The role of the solar wind on the observed Greenstein effect is investigated. The coma gas molecules are assumed to interact with the particles of the solar wind through elastic collisions which increase in frequency at increasing nuclear distances. The maximum jet velocity and density have also been increased to 5.0 km/s and 500 times the surrounding density respectively.

CHAPTER 8 SUMMARY

8.1 PRESENT RESEARCH

The assumption of an optically-thin coma is verified by the accurate representation of the observed R-branch line intensities in the coma of Comet P/Halley. The use of more accurate molecular constants and a whole-disk, high-resolution solar spectrum improved the computer model of the Swings effect over that originally developed by Aikman et al (1974). Both models still do not accurately predict the intensities of the first 7 R-branch lines (lines R(0) through R(6)). Zucconi and Festou (1985) have overcome this problem by introducing an additional channel of radiation, the A-X (0,0) red band system of CN, in their models of fluorescent equilibrium which eliminates the problem.

While reducing the spectra several unidentified lines interspersed throughout the R-branch were noticed. All 221 one-dimensional spectra were co-added in order to increase the signal-to-noise ratio and aid in the identification of these lines. The lines were highly pronounced in the co-added spectrum and were identified as belonging to both the ^{12}CN (1,1) band system and the ^{13}CN (0,0) band system. These lines had previously been detected by Aikman et al (1974) but due to the lower resolution of their spectra a clear identification was not possible. The spectra of Wehinger et al (1986) confirm the present identification. The ^{13}CN R(7) and R(8) lines were then used in order to obtain the $^{12}\text{C}/^{13}\text{C}$ ratio in P/Halley. A value of 88.9 ± 1.8 was found which is in direct agreement with past determinations using other comets and the solar value of 89. The error bars on the carbon isotope ratio are the smallest to date demonstrating the accuracy of this newly employed method. The ratio itself implies that Comet P/Halley was formed within the primordial solar

nebula (since it is known that this ratio differs in the nearby interstellar medium), and that the solar nebula was extremely homogeneous with regards to these two isotopes.

The Greenstein effect was seen observationally in Comet P/Halley and the R(9)/R(12) ratio was used to create two velocity maps of the gas in the coma. The first map comprises a velocity profile across the coma perpendicular to the head-tail axis of the comet while the second map is aligned along this axis. The results of the first map indicate that there are regions in the coma where the gas velocity either drops or increases by as much as 1.57 km/s within the resolution of the sampled Greenstein effect (4501 km). In order to understand how such velocity flows could arise, the Greenstein effect was modeled by assuming a given velocity distribution and then solving Equation 27 to predict the observed R(9)/R(12) ratio. As the Greenstein effect is due solely to internal *motions* of the gas in the coma, the observed effect must have been produced by one such velocity flow model. It was found that the observed effect could be simulated by using a model of radial gas expansion from the nucleus where the gas density decreased with distance from the nucleus and the majority of the CN gas was concentrated in jets. As cyanogen gas jets have been observed by A'Hearn et al (1987) in Comet P/Halley, this model does not require any additional, unobserved velocity motions to reproduce the observed Greenstein effect. Solar wind effects were introduced and created a predictable variation in the underlying general R(9)/R(12) ratio which was not observed in P/Halley.

8.2 FUTURE RESEARCH

There is much still to be done in cometary research and this thesis suggests many further avenues that still need to be investigated. With the availability of larger telescopes operating in the sub-millimeter spectral regime, the possibility of observing the pure rotational transitions in the ground state of the CN molecule in the coma of a comet are

greatly increased. Knowledge of the actual population of the levels in the ground state would serve further to refine the models and to define quantitatively the region in the coma where collisional excitation becomes important. Additional knowledge relating to the speed of the gases in a jet and the size and density of jets must be gained before models of the Greenstein effect can accurately predict observed line ratios. In addition, more complicated models of the Greenstein effect need to be formulated to include the effects of the observational geometry (the observer is not located on the sun in reality) and the three-dimensional distribution of gas jets in the coma. Further observational constraints on the composition of the primordial solar nebula can be obtained through study of other isotope ratios besides $^{12}\text{C}/^{13}\text{C}$ in a comet. In particular, Zucconi and Festou (1986) have indicated that there is a good possibility of determining the $^{14}\text{N}/^{15}\text{N}$ ratio using the same technique as employed herein (also through utilization of the CN (0,0) violet band). Finally, velocity maps of the coma can be produced with higher resolutions (the data used herein may be re-sampled so that neighboring bins overlap each other providing a spatial resolution of up to 450 km at the comet) and the temporal variation of the coma gas velocity may be studied with many successive observations of the same region.

REFERENCES

- A'Hearn, M.F. (1982) in *Comets*, The University Of Arizona Press, 433
- A'Hearn, M.F., Ohlmacher, J.T., Schleicher, D.G. (1983) University of Maryland,
Technical report TR AP83-044
- A'Hearn, M.F. (1984) *Chem. Eng. News*, **62**, 32
- A'Hearn, M.F., Hoban, S., Birch, P., Bowers, C., Martin, R., Klinglesmith, D. (1987)
ESA Bull., **49**, 70
- Aikman, G.C.L., Balfour, W.J., Tatum, J.B. (1974) *Icarus* , **21**, 303
- Arpigny, C. (1964) *Ann. d'Ap.*, **27**, 393
- Arpigny, C. (1976) in *The Study of Comets*, IAU Colloquium No. 25. NASA SP-393, p.
814
- Balam, D. (1987) University of Victoria, Private Communication
- Barr, W.L. (1962) *J. Opt. Soc. Amer.*, **51**, 943
- Bockasten, K. (1961) *J. Opt. Soc. Amer.*, **52**, 885
- Catalano, F.A., Baratta, G.A., Lo Presti, C., Strazzulla, G. (1986) *Astron. Astrophys.*,
168, 341
- Combi, M.R. (1980) *Ap. J.*, **241**, 830
- Combi, M.R., Delsemme, A.H. (1980a) *Ap. J.*, **237**, 633
- Combi, M.R., Delsemme, A.H. (1980b) *Ap. J.*, **237**, 641
- Crovisier, J. (1987) *Astron. Astrophys. Suppl. Ser.*, **68**, 223
- Danks, T., Arpigny, C. (1973) *Astron. Astrophys.*, **29**, 347
- Delsemme, A. H. (1982) in *Comets*, The University Of Arizona Press, 85
- Durand, D. (1987) Canadian Space Astronomy Data Center, Private Communication
- Engleman, R. Jr. (1974) *J. Mol. Spect.*, **49**, 106

- Feldman, P.D., A'Hearn, M.F., Festou, M.C., McFadden, L.A., Weaver, H.A., Woods, T.N. (1986) *Nature*, **324**, 433
- Festou, M., Zucconi, J.M. (1984) *Astron. Astrophys.*, preprint
- Festou, M., Encrenaz, T., Boisson, C., Pedersen, H., Tarenghi, M. (1987) *Astron. Astrophys.*, **174**, 299
- Greenstein, J.L. (1958) *Ap. J.*, **128**, 106
- Grün, E., Graser, U., Kohoutek, L., Thiele, U., Massonne, L., Schwehm, G. (1986) *Nature*, **321**, 144
- Hanes, D. (1987) Queen's University, Private Communication
- Hawkins, I., Jura, M. (1987) *Ap. J.*, **317**, 926
- Herlitz, S.I. (1963) *Ark. f. Fysik.*, **23**, 571
- Hearnshaw, J. B. (1986) The analysis of starlight. One hundred and fifty years of astronomical spectroscopy, Cambridge University Press
- Herzberg, G.H. (1963) Molecular spectra and molecular structure. I. Spectra of diatomic molecules, 2nd ed., eighth printing, New York: D.Van Nostrand Co.
- Herzberg, G.H. (1976) in Mem. Soc. Roy. des Sci. de Liège, Series 6, **9**, 115
- Huber, K.P., Herzberg, G. (1979) Molecular spectra and molecular structure. IV. Constants of diatomic molecules, New York: Van Nostrand Reinhold Co.
- Hunaerts, J. (1959a) *Ann. d'Ap.*, **22**, 790
- Hunaerts, J. (1959b) *Ann. d'Ap.*, **22**, 812
- Ishii, H., Tamura, S. (1979) *PASJ*, **31**, 597
- Jenkins, C.R. (1987) *M.N.R.A.S.*, **226**, 341
- Jewitt, D.C., Meech, K.J. (1987) *Ap. J.*, **317**, 992
- Larson, S.M., Sekanina, Z. (1984) *Astron. Journal*, **89**, 571 and 1408
- Le Borgne, J.F., Leroy, J.L., Arnaud, J. (1987) *Astron. Astrophys.*, **173**, 180

- Levasseur-Regourd, A.C., Bertaux, J.L., Dumont, R., Festou, M., Giese, R.H., Giovane, F., Lamy, P., Le Blanc, J.M., Llebaria, A., Weinberg, J.L. (1986) *Nature*, **321**, 341
- Luk, C.K., Bersohn, R. (1973) *J. Chem. Phys.*, **58**, 2153
- Malaise, D. (1970) *Astron. Astrophys.*, **5**, 209
- Mendis, D.A., Houpis, H.L.F., Marconi, M.L. (1985) *Fund. Cosmic Phys.*, **10**, 1
- Moore, C.E. (1959) A Multiplet Table of Astrophysical Interest, Revised Edition
- Morton, D.C., dir. (1981) Anglo-Australian Observatory Observers' Guide, Revision III
- Owen, T. (1973) *Ap. J.*, **184**, 33
- Paquette, D.R., Wiese, W.L. (1964) *Appl. Opt.*, **3**, 291
- Reinhard, R. (1987) *ESA Bull.*, **49**, 62
- Sagdeev, R.Z., Shapiro, V.D., Shevchenko, V.I., Szegö, K. (1987) *Astro. Lett. and Communications*, **25**, 247
- Schadee, A. (1971) *Astron. Astrophys.*, **14**, 401
- Schadee, A. (1975) *Astron. Astrophys.*, **41**, 203
- Schleicher, D.G. (1983) PhD Dissertation, University of Maryland
- Sekanina, Z., Larson, S.M. (1986) *Nature*, **321**, 357
- Stawikowski, A., Greenstein, J.L. (1964) *Ap. J.*, **140**, 1280
- Suchard, S.N., ed. (1975) Spectroscopic Data 1. Heteronuclear Diatomic Molecules Part A
- Swings, P. (1941) *Lick Obs. Bull.*, **19**, 131
- Tatum, J.B. (1984) *Astron. Astrophys.*, **135**, 183
- Tatum, J.B., Campbell, E.C. (1983) in Cometary Exploration I. Hungarian Acad. Sci., 191
- Tatum, J.B., Gillespie, M.I. (1977) *Ap. J.*, **218**, 569

- Wehinger, P.A., Peterson, B.A., Wyckoff, S., Lindholm, E., Festou, M., Zucconi, J.M.
(1986) in 20th ESLAB Symposium Proceedings, Heidelberg, Germany (Volume III)
- Weinard, J. (1955) *Ann. d'Ap.*, **18**, 334
- Whipple, F.L. (1982) in *Comets*, The University Of Arizona Press, 227
- Whiting, E.E., Schadee, A., Tatum, J.B., Hougen, J.T. (1980) *J. Mol. Spect.*, **80**, 249
- Winnberg, A., Ekelund, L., Ekelund, A. (1987) *Astron. Astrophys.*, **172**, 335
- Wyckoff, S., Lindholm, E., Wehinger, P.A., Peterson, B.A., Zucconi, J.M., Festou, M.
(1987) *B.A.A.S.* , in press
- Woods, T.N., Feldman, P.D., Dymond, K.F., Sahnou, D.J. (1986) *Nature*, **324**, 436
- Woods, T.N., Feldman, P.D., Dymond (1987) *Astron. Astrophys.*, in press
- Zucconi, J.M., Festou, M.C. (1985) *Astron. Astrophys.*, **150**, 180
- Zucconi, J.M., Festou, M.C. (1986) *Astron. Astrophys.*, **158**, 382

APPENDIX 1

SOLUTION OF THE ABELIAN INTEGRAL EQUATION

In Chapter 2 our solution of Abel's equation was stated in Equation (2) without proof. We shall now proceed to prove this result in detail starting from Equation (1).

From geometry,

$$N(\eta) = 2a \int_{\eta}^1 \frac{n(\rho)\rho \, d\rho}{\sqrt{\rho^2 - \eta^2}}. \quad (1)$$

Let $v = 1 - \eta^2, \quad \Rightarrow \quad \eta^2 = 1 - v$

$$N(\eta) = g(v),$$

$$a n(\rho) = f(u),$$

and $u = 1 - \rho^2. \quad \Rightarrow \quad \rho = \sqrt{1 - u}$

$$du = -2\rho d\rho$$

$$\rho d\rho = -\frac{1}{2} du$$

Then Equation (1) becomes,

$$g(v) = 2 \int_{u=v}^0 \frac{f(u) \left(\frac{1}{2}\right) du}{\sqrt{1 - u - (1 - v)}}$$

$$g(v) = - \int_{u=v}^0 f(u) (v - u)^{-1/2} du$$

so,

$$g(v) = \int_0^v f(u) (v - u)^{-1/2} du. \quad (4)$$

Therefore, $g(v) = f(v) * v^{-1/2}$,

where the asterisk denotes the convolution. Let $G(s)$ and $F(s)$ be the Laplace transforms of $g(v)$ and $f(v)$ respectively. The Laplace transform of $v^{-1/2}$ is $\sqrt{\frac{\pi}{s}}$, so that, by an application of Borel's theorem,

$$G(s) = F(s) \sqrt{\frac{\pi}{s}}. \quad (5)$$

Therefore, $\pi F(s) = s H(s)$, (6)

where $H(s) = \sqrt{\frac{\pi}{s}} G(s)$. (7)

Taking the inverse transforms of Equations (6) and (7) and noting that s is a dummy variable, we obtain

$$\pi f(u) = h'(u) + h(0), \quad (8)$$

where $h(u) = \int_0^u g(w) (u - w)^{-1/2} dw$, (9)

from which we find (using Equations (8) and (9))

$$f(u) = \frac{1}{\pi} \frac{d}{du} \int_0^u g(w) (u - w)^{-1/2} dw. \quad (10)$$

Numerical integration of Equation (10) fails near the singularity at the upper limit.

The difficulty is overcome by the substitution

$$w = u \sin^2\theta. \Rightarrow dw = u (2 \sin\theta \cos\theta) d\theta$$

Using the previous result that

$$du = -2\rho d\rho,$$

so that

$$\frac{d}{du} = \frac{-1}{2\rho} \frac{d}{d\rho},$$

Equation (10) becomes

$$a n(\rho) = \frac{1}{\pi} \left(\frac{-1}{2\rho} \right) \frac{d}{d\rho} \left\{ \int_0^{\pi/2} g(w) (u - u \sin^2\theta)^{-1/2} dw \right\}$$

$$a n(\rho) = \frac{-1}{2\pi\rho} \frac{d}{d\rho} \left\{ (1 - \rho^2)^{-1/2} \int_0^{\pi/2} g(w) (1 - \sin^2\theta)^{-1/2} dw \right\}.$$

But

$$dw = 2 (1 - \rho^2) \sin\theta \cos\theta d\theta,$$

so that

$$a n(\rho) = \frac{-1}{2\pi\rho} \frac{d}{d\rho} \left\{ \frac{1}{\sqrt{1 - \rho^2}} \int_0^{\pi/2} g(w) \frac{2(1 - \rho^2) \cos\theta}{\sqrt{1 - \sin^2\theta}} \sin\theta d\theta \right\}.$$

Simplifying yields

$$a n(\rho) = \frac{-1}{\pi\rho} \frac{d}{d\rho} \left\{ (1 - \rho^2)^{1/2} \int_0^{\pi/2} g(w) \frac{\cos\theta}{\sqrt{1 - \sin^2\theta}} \sin\theta d\theta \right\}.$$

But $\cos\theta = \sqrt{1 - \sin^2\theta},$

therefore

$$a n(\rho) = \frac{-1}{\pi\rho} \frac{d}{d\rho} \left\{ (1 - \rho^2)^{1/2} \int_0^{\pi/2} g(w) \sin\theta d\theta \right\}, \quad (11)$$

where

$$\begin{aligned} g(w) &= g(u \sin^2\theta) \\ &= g((1 - \rho^2) \sin^2\theta) \\ &= g(\sin^2\theta - \rho^2 \sin^2\theta). \end{aligned}$$

But, $g(v) = N(\eta)$

where $\eta^2 = 1 - v. \Rightarrow \eta = \sqrt{1 - v}$

Thus

$$g(\sin^2\theta - \rho^2 \sin^2\theta) = N\left(\sqrt{1 - (\sin^2\theta - \rho^2 \sin^2\theta)}\right).$$

So we have $g(w) = N[(1 - \sin^2\theta + \rho^2 \sin^2\theta)^{1/2}]. \quad (12)$

Finally, substituting Equation (12) into Equation (11) gives

$$a n(\rho) = \frac{-1}{\pi\rho} \frac{d}{d\rho} \left\{ (1 - \rho^2)^{1/2} \int_0^{\pi/2} N[(1 - \sin^2\theta + \rho^2 \sin^2\theta)^{1/2}] \sin\theta d\theta \right\}.$$

This can also be written as

$$n(\rho) = \frac{-1}{\pi a \rho} \frac{d}{d\rho} \left\{ (1 - \rho^2)^{1/2} \int_0^{\pi/2} N[(1 - (1 - \rho^2)\sin^2\theta)^{1/2}] \sin\theta d\theta \right\}. \quad (2)$$

APPENDIX 2
THE OBSERVING RECORDS: COMET IRAS-ARAKI-ALCOCK

The following is a fascimile of the observing log at Kitt Peak for the observation of Comet IRAS-Araki-Alcock (1983 VIII) used in Chapter 2, section 4, to obtain a space density profile of the gas in the coma.

Kitt Peak National Observatory
 CCD Direct Camera Log

Page 10

Date May 8/1983

Telescope 0.9 m (#1) f Ratio 7.5

Tape No. T4465

Observer Pritchett / Infante

Density 1600

Tape Format FITS Filters used U,B,V,R,I, H α

Tape Picture Number 36 Disk File 118 Object Comet IRAS-Araki-Alcock

Coordinates $\alpha \approx 18\ 01\ 36$, $\delta \approx +63\ 57\ 43$ Epoch 1950

Beg. UT 10:58

End HA 0:33 w Telescope Focus 2590

Filter Type U

Integration Time 100 seconds

Air Mass 1.18

APPENDIX 3 THE OBSERVING RECORDS: COMET P/HALLEY

The following is a facsimile of the observing log at the AAT for the observations of Comet P/Halley used extensively throughout the course of this research.

RGO/IPCS Log Anglo-Australian Observatory

Camera: 82 cm Grating: 1200 J Frame Lines: 2048 Page: 84
 Collimator: 5.92 Blaze To: Camera Line Incr.: 258 Civil Date: 14-15/4/86
 Slit Corr.: +10 Grtc. Angle Corr.: 0 X-Res Factor: 1 N.A.: Cooper
 Format: 2040 x 220 / 29.2 X-Gain: High Tape No.: 1632
 Observers: Tatum, Ramsay

Run No.	Object	1950.0						Start		
		RA			DEC			H.A.	Z.D.	U.T.
		H	M	S	°	'	"			
1	Comet Halley	13	33	37.8	-43	07	34	-5 21	62.6	08 49
2	"	13	33	41.9	-43	06	16	-5 01	59.1	09 09
3	"	13	33	47.5	-43	05	04	-4 42	55.9	09 28
4	"	13	32	26.0	-43	03	52	-4 23	52.5	09 45
5	"	13	31	47.8	-43	02	39	-4 04	49.1	10 04
6	"	13	32	15.5	-42	57	27	-3 47	45.8	10 22
7	"	13	31	59.3	-42	52	13	-3 28	42.5	10 40
8	"	13	31	41.6	-43	02	52	-3 08	38.8	11 00

Run No.	Object	1950.0						Start		
		RA			DEC			H.A.	Z.D.	U.T.
		H	M	S	°	'	"			
9	Comet Halley	13	31	23.1	-43	05	27	-2 47	34.9	11 21
10	Cu Ar (arc)									
11	Ceres	10	37	47.2	+24	43	51	+0 32	56.3	11 46
12	Cu Ar (arc)									
13	Comet Halley	13	31	00.9	-42	50	05	-1 57	26.0	12 10
14	"	13	29	52.8	-42	48	12	-1 28	21.0	12 38
15	"	13	30	20.2	-42	54	57	-1 10	18.3	12 56
16	"	13	29	20.2	-42	53	40	-0 50	15.5	13 14
17	Cu Ar (arc)									

Run No.	A & G Angle	Dwell	Indicated		Filters	Remarks
			Slit	Grating		
			Dekker	Angle		
1	90°	1000	40 / 50	12°.72	CuSO ₄	Nucleus
2	↓	1000	↓	↓	"	4 arc minutes east
3		1000			"	8 arc minutes east
4		1000			"	4 arc minutes west
5		1000			"	8 arc minutes west
6		1000			"	4 arc minutes north
7		1000			"	8 arc minutes north
8		1000			"	4 arc minutes south
9		1000			"	8 arc minutes south

Run No.	A & G Angle	Dwell	Indicated		Filters	Remarks
			Slit Dekker	Grating Angle		
10	90°	104	40 / 50	12°.72	CuSO ₄ ND 2.5	arc
11	↓	1000	↓	↓	CuSO ₄ ND 7	asteroid Ceres
12		113			CuSO ₄ ND 2.5	arc
13		1000			CuSO ₄	4 arcmin north & east
14		1000			"	4 arcmin north & west
15		1000			"	4 arcmin south & east
16		1000			"	4 arcmin south & west
17		120			CuSO ₄ ND 2.5	arc

APPENDIX 4

IRAF ROUTINE DESCRIPTIONS

The following list is a description of the IRAF routines used in reducing and analyzing the AAT IPCS data. For each routine used, the routine name is given in bold letters followed by the shortest possible usage of the routine (i.e. minimal parameters that must accompany the routine called). A short description of the key parameters used with the routine is followed by a description of the routine's purpose along with examples of its use in reducing the AAT data. Note that default values of a parameter, if such exist, are given following the parameter name.

Fitcoords

USAGE: **fitcoords** *images fitname*

PARAMETERS: **images**

- List of images containing the feature coordinates to be fit. If the parameter *combine* is "yes" then feature coordinates from all of the images are combined and fit by a single function. Otherwise, the feature coordinates from each image are fit separately.

fitname = ""

- If the input images are combined and fit by a single function then the fit is stored under this name. If the images are not combined then the fit for each image is stored under the name formed by appending the image name to this name. A null prefix is acceptable when not combining but it is an error if combining a list of images.

interactive = yes

- Determine coordinate fits interactively?

DESCRIPTION:

A two dimensional function of the image coordinates is fitted to the user coordinates from the specified images;

$$\text{user coordinate} = \text{function}(\text{column}, \text{line}).$$

The coordinates from all the input images may be combined in a single fit or the coordinates from each image may be fit separately. When the fitting is done interactively the user may change the fitted function and orders iteratively, delete individual coordinates or entire features, and graph the fit and residuals in a number of ways.

EXAMPLES:

A number of strong arc lines are identified along one line of the arc calibration image. The arc lines are then reidentified at every 10th line so that any pin-cushion distortion (curvature) can be traced. A two dimensional function that corrects the distortion and converts to a wavelength scale is determined as follows:

$$\text{fitcoords argarc c}$$

Here the fitting was done interactively until the residuals were satisfactory.

To correct for s-distortion, the "artificial" spectrum of Ceres was first used to identify positions along one column where the spectrum crossed the column. These positions were then reidentified at every 10th column tracing any s-distortion on the IPCS faceplate. A two dimensional function to correct the distortion was fit interactively as follows:

$$\text{fitcoords ceres s}$$

Identify

USAGE: *identify images*

PARAMETERS: *images*

- Images containing features to be identified.

section = "middle line"

- If an image is not one dimensional or given as a one dimensional image section then the image section given by this parameter is appended to the image name.

coordlist = "identify\$henear"

- User coordinate list.

nsum = 10

- Number of lines or columns to be summed when the image is two dimensional.

fwidth = 4

- Width in pixels of features to be identified.

DESCRIPTION:

Features in the input images are identified interactively and assigned user coordinates. A "coordinate function" mapping pixel coordinates to user coordinates may be determined from the identified features. A user coordinate list is used to identify additional features automatically. This task is used to measure positions of features, determine dispersion solutions, and to identify features in two dimensional images to be traced and extracted or used to map a two dimensional coordinate transformation.

To define or mark a feature in a spectrum, the 'm' key is used. The feature nearest the cursor position is marked. The feature position is determined by the feature centering algorithm.

If two or more features are identified spanning the range of the data or if a coordinate function is defined then the 'l' key may be used to identify additional features from a coordinate list.

The 'f' key fits a function of the pixel coordinates to the user coordinates. The type of function and the order are initially set with the parameters *function* and *order* (which default to a first order Chebyshev polynomial). The fitting is done within the interactive curve fitting package which has its own set of interactive commands.

EXAMPLES:

The copper-argon comparison arc is to be used in order to trace the pin-cushion distortion and dispersion correct the spectra. To accomplish these tasks, several arc lines must first be marked so that they can later be traced perpendicular to the dispersion. To do this the following command is entered:

```
identify argarc coordlist="argon.dat"
```

which enables the user to mark lines with the 'm' key. After three lines are marked, the 'l' keystroke is used to automatically identify the other lines found in the supplied database of argon line wavelengths. These user coordinates are stored automatically in the database directory file "idargarc".

Similarly, the "artificial" spectrum of Ceres is to be used to correct for s-distortion and so the image must be marked for the points where the individual spectra cross a column. To do this, the command entered was

```
identify ceres section="middle column" fwidth=15
```

which enables marking of all the features. These user coordinates are stored in the database directory file "idceres".

Imcopy

USAGE: *imcopy input output*

PARAMETERS: *input*

- Images to be copied.

output

- Output images or directory.

verbose = yes

- Print each operation as it takes place?

DESCRIPTION:

Each of the input images, which may be given as a general image template including sections, is copied to the corresponding output image list, which may also be given as an image template, or the output directory. If the output image name exists and contains a section then the input image will be copied into that section of the output image (provided it is of the same size). The verbose operation just verifies that the input image name has been copied to the output image name.

EXAMPLES:

For a simple copy of an image:

```
imcopy image imagecopy
```

To trim all of the raw AAT spectra to 170 by 1301 pixels:

```
imcopy data*[300:1600,38:207] data*
```

It is found that the spectrum of Ceres is contained within pixels 76 to 90 in the slit direction. In order to trace s-distortions, an "artificial" image of Ceres is to be created whereby its spectrum is copied down the spatial axis several times. This is done by the commands:

```
imcopy data011 ceres
imcopy ceres[* ,76:90] ceres[* ,16:30]
imcopy ceres[* ,76:90] ceres[* ,46:60]
imcopy ceres[* ,76:90] ceres[* ,106:120]
imcopy ceres[* ,76:90] ceres[* ,136:150]
```

Implot

USAGE: `implot image [line]`

PARAMETERS: `image`

- Name of (first) image to be plotted.

`line`

- If given, the number of the image line to be plotted, otherwise the central line is plotted.

DESCRIPTION:

Implot is an interactive, cursor driven task for examining images by plotting the lines and columns or the averages of lines and columns. A single image line is plotted when the task is first run, then cursor mode is entered and keystrokes may be used to generate additional line and column plots. Some of these keystrokes include the ability to expand part of a plot both in the horizontal and vertical direction ('e' keystroke), and to overplot one image on top of another at any scale ('o' keystroke).

EXAMPLES:

The 3 arc calibration images are to be checked against each other to see if any shifts have occurred in the spectrograph during the AAT observations. To do this, we first enter implot with the command:

```
implot arc1
```

which causes the middle line of the first arc image to be displayed. The 'o' keystroke is used next to overplot the second and third arc images on the first at the same viewing scale. If any shifts are present between the images, they will clearly be seen in this operation.

Imsum

USAGE: `imsum input output`

PARAMETERS: `input`

- Input images.

`output`

- Output image.

`title = ""`

- Image title for the output image. If null ("") then the title of the first image is used.

`pixtype = ""`

- Pixel datatype for the output image. The pixel datatypes are "double", "real", "long", "integer", and "short" in order of precedence. If null ("") then the highest precedence datatype of the input images is used. The datatypes may be abbreviated to a single character.

`calctype = ""`

- Calculation type. The calculation types are the same as the pixel datatypes.

`option = "sum"`

- Output options are "sum", "average", or "median".

DESCRIPTION:

The input images are summed, averaged, or medianed pixel by pixel and the result recorded in the output image. All input images must be the same size but not necessarily of the same pixel datatype. Beware of integer overflows with images of datatype short.

EXAMPLES:

To create one comparison arc spectrum by adding the 3 spectra taken:

```
imsum arc1,arc2,arc3 argarc pixtype="real" calctype="real"
```

To coadd all of the 221 one dimensional spectra (while keeping the exposure time accurate):

```
imsum pos* coadd hparams="exposed" pixtype="real" calctype="real"
```

Reidentify

USAGE: reidentify *reference images*

PARAMETERS: reference

- Image with previously identified features.

images

- Images in which the features in the reference image are to be reidentified. The image may be the same as the reference image to reidentify features in other lines or columns.

section = "middle line"

- If the reference image to be reidentified is not one dimensional or given as a one dimensional image section then the image section given by this parameter is appended to the image name.

step = 10

- The step between lines or columns when reidentifying features in the same two dimensional image (i.e. tracing features). If the step is zero then no tracing is done.

nsum = 10

- The number of lines or columns to be summed in two dimensional images before reidentifying the features.

DESCRIPTION:

Features identified in a reference image are reidentified in other lines or columns of two dimensional images and in other images. The features for the reference image and those determined for reidentified images are recorded in the database. If the image is two dimensional and the step size is not zero then the features are reidentified at the other lines or columns by tracing from the starting line or column in the specified step size.

For tracing identifications in two dimensional images, the features are recentered starting from the previously reidentified line or column. This tracing proceeds in steps given by the parameter *step* in both directions from the reference line or column. The tracing stops at the edges of the image or when the number of features lost exceeds the allowed number (default is 0).

In two dimensional images a number of lines or columns given by the parameter *nsum* are summed to form the one dimensional image vector in which the features are to be identified. This increases the accuracy for weak features.

EXAMPLES:

The features in image "argarc" were identified previously using the middle line with the task *identify* . These features (6 spectral lines) are to be traced and reidentified every 10 pixels in the slit direction to trace out any curvature. This is done with the command:

reidentify argarc argarc

Rfits

USAGE: *rfits fits_file file_list iraf_file*

PARAMETERS: *fits_file*

- The FITS data source. If the data source is a disk file or an explicit tape file specification of the form *mt*[n]* where *n* is a file number then only that file is converted.

file_list

- The files to be read from a tape are specified by the *file_list* string. The string can consist of any sequence of file numbers separated by at least one of comma, or dash.

iraf_file

- The IRAF file which will receive the FITS data if the *make_image* parameter switch is set. For tape files specified by the *file_list* parameter the filename will be used as a prefix and the file number will be appended.

make_image = yes

- This switch determines whether FITS image data is converted to an IRAF image file. This switch is set to *no* to obtain just header information.

DESCRIPTION:

FITS data is read from the specified source, either a disk file or magnetic tape, and converted to IRAF image files.

EXAMPLES:

The raw data from the AAT were stored in FITS format on magnetic tape. In order to reduce these data with IRAF, they first had to be read into the computer and converted to IRAF image files with the command:

```
rfits mtd 1-17 data
```

Splot

USAGE: `splot image line`

PARAMETERS: `image`

- The image or spectrum name to plot. If a two-dimensional image, the parameter, *line*, is required.

`line`

- The image line to plot if two-dimensional.

DESCRIPTION:

SPLIT provides an interactive facility to display and analyze spectra. If the image is two-dimensional, the image line to be displayed is also required. After the initial display, all functions are driven by single keystroke commands when the graphics cursor is displayed. Some of these commands are:

- a Auto-expand - expands region between vertical cursors and autoscales vertically.
- c Prints cursor position in x and y.
- d Deblends emission lines. Up to 4 simultaneous lines can be deblended. Returned values are the line heights, centers, FWHM, and integrated flux.
- e Equivalent width. Requires 2 cursor settings. Both x and y cursors are used; the y cursor sets the continuum level which may be sloping, and the x cursor delineates the area of integration. Returned values are the flux above

the continuum (may be negative for absorption lines), the line center (from a weighted center of gravity), and the equivalent width, in angstroms (assuming the spectrum is properly corrected).

- g Get another spectrum to work on. The current spectrum is discarded.
- m Mean, RMS, and signal-to-noise over a region. Requires 2 cursor settings in x.
- o Overplot another spectrum. Only one spectrum can be worked on at a time and the new spectrum replaces the old for future operations.
- (Minus sign). Subtract a fit generated by the deblend routine. Requires two settings in x.

EXAMPLES:

The flux of a line in the R-branch of a spectrum of the CN (0,0) violet band for Comet P/Halley is needed in order to model the observed Greenstein effect. The one-dimensional spectrum is first loaded into splot with the commands

```
splot pos.2.0009
```

and then manipulated by using the 'a' keystroke until the desired line is clearly visible. The 'e' keystroke is then used in order to obtain the flux above a set continuum.

Toonedspec

USAGE: `toonedspec input output`

PARAMETERS: `input`

- List of input two-dimensional spectra. The header parameter DISPAXIS must be defined.

`output`

- List of output root names for the one-dimensional spectra.

`startrec = 1`

- Starting output record number to be appended to the output root name.

first = 1

- First column or line of the two-dimensional spectrum to be extracted.

last = INDEF

- Last column or line of the two-dimensional spectrum to be extracted. If INDEF then the last column or line defaults to the last column or line of the 2D spectrum.

step = 1

- Step in columns or lines for extraction.

nsum = 1

- Number of columns or lines to sum for each extraction.

DESCRIPTION:

A set of columns or lines (determined by the image header parameter DISPAXIS in the input spectra) is extracted from each input two-dimensional spectrum and new one-dimensional spectra are created. The output pixel type is "real" regardless of the input pixel type.

The set of lines or columns extracted is specified by a first and last column or line and a step. For example, if the first column is 10, the last column 20, and the step is 5 then the extracted columns are 10, 15, and 20. A number of neighboring columns or lines may be summed using the *nsum* parameter. In the example, if *nsum* = 3 then the extraction columns are the sums of columns 10 to 12, 15 to 17, and 20 to 22.

EXAMPLES:

The 13 spectra of Comet P/Halley have been corrected for distortions and wavelength calibrated. In order to increase spatial resolution, they are each to be divided up into 17 "bins" with 10 pixels belonging to each bin. These bins are to be collapsed forming 221 one-dimensional spectra in total. This is accomplished by the command (done for each of the 13 spectra):

```
toonedspec pos.1 pos.1 first=1 last=170 step=10 nsum=10
```

Transform

USAGE: `transform input output fitnames`

PARAMETERS: `input`

- List of input images to be transformed.

`output`

- List of output images. The number of output images in the list must match the number of input images.

`fitnames`

- Names of the user coordinate maps in the database to be used in the transform.

`interptype = "spline3"`

- Image interpolation type. The allowed types are "nearest" (nearest neighbor), "linear" (bilinear), "poly3" (bicubic polynomial), "poly5" (biquintic polynomial), and "spline3" (bicubic polynomial).

`flux = yes`

- Conserve flux per pixel? If "no" then each output pixel is simply interpolated from the input image. If "yes" the interpolated output pixel value is multiplied by the Jacobean of the transformation (essentially the ratio of pixel areas between the output and input images).

$x1 = \text{INDEF}, y1 = \text{INDEF}$

- User coordinates of the first output column and line. If INDEF then the smallest value corresponding to a pixel from the image used to create the coordinate map is used.

$x2 = \text{INDEF}, y2 = \text{INDEF}$

- User coordinates of the last output column and line. If INDEF then the largest value corresponding to a pixel from the image used to create the coordinate map is used.

$dx = \text{INDEF}, dy = \text{INDEF}$

- Output pixel intervals. If INDEF then the interval is set to yield the specified number of pixels.

$nx = \text{INDEF}, ny = \text{INDEF}$

- Number of output pixels. If INDEF and if the pixel interval is also INDEF then the number of output pixels is equal to the number of input pixels.

DESCRIPTION:

The coordinate maps created by the task *fitcoords* are read in from the database. The maps are used to interpolate the input images to a new coordinate grid in the output images. This is done by determining two surface functions, $\text{column} = f(u1, u2)$ and $\text{line} = g(u1, u2)$, where $u1$ and $u2$ are the user coordinates evaluated from the coordinate maps at an even

grid in the input images. The type of image interpolation is selected by the user. The parameter *flux* selects between direct image interpolation and a flux conserving interpolation.

The output coordinate grid may be defined by the user or allowed to default to an image of the same size as the input image spanning the full range of user coordinates in the coordinate transformation map.

EXAMPLES:

The arc calibration image was used to determine a two-dimensional dispersion map which also corrected for pin-cushion distortion. The "artificial" image of Ceres was used to determine a two-dimensional s-distortion map. These maps were made using the task *fitcoords*. To transform the 13 AAT spectra into linear wavelength between 3850 and 3888 Angstroms with a dispersion of 32 mÅ/pixel:

```
transform data* pos.* cargarc,sceres interptype="poly3" x1=3850 x2=3888
dx=0.032
```

Wfits

USAGE: `wfits iraf_files fits_files`

PARAMETERS: `iraf_files`

- String parameter specifying the input file(s), e.g. "file1" or "file*".

`fits_files`

- String parameter specifying the output destination. Magnetic tape output is assumed if the first two characters are "mt", otherwise the output destination defaults to disk. Tape output will begin at the file number specified in `fits_files`, e.g. file 5 if `fits_files = "mtb1600[5]"`.

newtape

- Boolean parameter specifying whether an output tape is blank or contains data.

make_image = yes

- By default wfits writes the FITS image(s) to the output destination. If make_image = no, then the FITS headers can be examined before actually writing a FITS tape.

bitpix = 0

- A bitpix of 8, 16, or 32 will produce either an unsigned byte, twos-complement 16 bit integer, or twos-complement 32 bit integer FITS image. If bitpix is set to any other value, wfits will choose the highest precision based on the IRAF image.

DESCRIPTION:

IRAF data is read from disk and written to the specified destination, either disk or magnetic tape, in FITS format.

EXAMPLES:

Write the first 17 reduced AAT spectra to a new magnetic tape in FITS format at the highest precision possible:

```
wfits pos.1.* mtd[1] bitpix=32
```

Write the next 17 spectra to the same magnetic tape without overwriting anything (again in FITS format at the highest possible precision):

```
wfits pos.2.* mtd[18] bitpix=32
```

APPENDIX 5 SELECTED PROGRAMS

Many programs were written in order to produce the results contained within this thesis. The following two FORTRAN program listings are given as representative samples. The first is the numerical program which performs the Abelian integral transformation on a table of data (i.e. Equation 2 of Chapter 2 is solved). The second is the program used to model the Greenstein effect. Note that the Swings effect is also modeled within this program.

```
C -----
C Program ABEL (Abel's equation solved for n(rho))
C - This program reads in the needed data (intensity profile) from a file and performs
C interpolation to solve for n(rho).
C -----
```

```
IMPLICIT REAL*8 (A-H,O-Z)
DIMENSION Z(500)
COMMON XARR(500),YARR(500),NUMVAL,IDEG,RLOWER,UPPER,
& XSHIFT
```

```
C -----
C Variable Dictionary:
C
C PI06      = PI * (12 * DRH) } USED IN DIFFERENCE EQUATION
C RH        = RHO
C DRH       = STEP SIZE FOR RHO SPACINGS
C ENRH      = n(RHO) {PROGRAM VALUE}
C NUMVAL    = THE NUMBER OF VALUES IN THE DATA TABLE TO BE READ
C           IN
C XARR      = ARRAY OF RHO VALUES (0<RHO<1)
C YARR      = ARRAY OF INTENSITY VALUES (AT EACH RHO DISTANCE)
C IDEG      = DEGREE OF INTERPOLATING POLYNOMIAL USED.
C DTH       = PI/400 (INTERVAL OF THETA ADJUSTMENT)
C XSHIFT    = DIFFERENCE BETWEEN TWO RHO (X) VALUES
C -----
```

```
C
C Read in the table of intensity values (NUMVAL values) and set degree of interpolating
C polynomial to be used.
C
WRITE (6,*) 'ENTER NUMBER OF VALUES IN DATA FILE',
```

```

&      '(199?):'
READ (5,*) NUMVAL
WRITE (6,*) ''
CALL GETABL
WRITE (6,*) 'Data read in....'
WRITE (6,*) 'Enter degree of interpolating poly.(1-9):'
READ (5,*) IDEG
C
DRH=XSHIFT
PI=3.14159265358979D0
PI06=PI*(12.0D0*DRH)
DTH=7.85398163398D-3
DTH3=DTH/3.D0
RH=0.D0
C
C NOW CALCULATE THE QUANTITY IN SQUARE BRACKETS IN EQUATION 2
C INTEGRATE USING SIMPSON'S RULE FROM 0 TO PI/2.
C
DO 2 J=1,NUMVAL+1
  IF ((J.EQ.(NUMVAL+1)).AND.((RH+DRH).GT.1.D0)) THEN
    RH=1.D0
    U=0.D0
  ELSE
    RH=RH+DRH
    U=1.D0-RH*RH
  END IF
  SUM=0.D0
  TH3=0.D0
  DO 1 I=1,100
    TH1=TH3
    TH2=TH1+DTH
    TH3=TH2+DTH
    S1=DSIN(TH1)
    S2=DSIN(TH2)
    S3=DSIN(TH3)
    ARG1=DSQRT(1.D0-U*S1*S1)
    ARG2=DSQRT(1.D0-U*S2*S2)
    ARG3=DSQRT(1.D0-U*S3*S3)
    F1=ENN(ARG1)*S1
    F2=ENN(ARG2)*S2
    F3=ENN(ARG3)*S3
    SUM=SUM+(F1+4.D0*F2+F3)*DTH3
  1  CONTINUE
  Z(J)=DSQRT(U)*SUM
  2  CONTINUE
C
C Generate Titles for Output
C
WRITE (6,5)
WRITE (8,5)
5  FORMAT(5X,'RHO',15X,'n(RHO)',/,5X,'---',15X,6('-'),/)

```

C
 C FINALLY, TO FIND N(RHO) USE A DIFFERENCE EQUATION IN
 C APPROXIMATING THE DERIVATIVE.

C
 DO 4 J=3,NUMVAL-1
 XJ=J
 RH=DRH*XJ
 ENRH=(Z(J+2)-Z(J-2)-8.D0*(Z(J+1)-Z(J-1)))/(PI06*RH)
 WRITE (6,3) RH,ENRH
 WRITE (8,3) RH,ENRH
 4 CONTINUE
 3 FORMAT(' ,F10.5,5X,G18.12)
 STOP
 END

C-----
 C SUBROUTINE GETABL:
 C - This subroutine reads in the data (intensity measurements at various rho values) into
 C the arrays XARR and YARR.

C-----
 SUBROUTINE GETABL
 IMPLICIT REAL*8 (A-H,O-Z)
 CHARACTER*1 DUMMY
 INTEGER UNIT
 COMMON XARR(500),YARR(500),NUMVAL,IDEG,RLOWER,
 & UPPER,XSHIFT

UNIT=10
 RLOWER=999.9D9
 UPPER=-999.9D9

WRITE (6,*) 'HAVE THE DATA BEEN FILTERED? (Y OR N)'
 READ (5,15) DUMMY
 WRITE (6,*) ''

C
 C DON'T READ TITLE INFORMATION IN (SKIP OVER IT) IF DATA IS
 C FROM PROGRAM WSIMP

C
 IF (DUMMY.NE.'Y') THEN
 WRITE(6,*) 'IS THERE HEADER INFO? (Y/N)'
 UNIT=9
 READ(5,15) DUMMY
 WRITE(6,*) ''
 IF (DUMMY.EQ.'Y') THEN
 DO 5 I=1,6
 READ (UNIT,15) DUMMY
 5 CONTINUE
 15 FORMAT(A1)
 END IF
 END IF

C
 DO 10 I=1,NUMVAL

```

      READ (UNIT,*) XARR(I),YARR(I)
      IF (XARR(I).LT.RLOWER) THEN
        RLOWER=XARR(I)
      END IF
      IF (XARR(I).GT.UPPER) THEN
        UPPER=XARR(I)
      END IF
10  CONTINUE
      XSHIFT=XARR(3)-XARR(2)
      RETURN
      END
C -----
C SUBROUTINE INTERP:
C - This subroutine performs interpolation on an array of data (equally spaced x values)
C since function values may be required at points other than those specified in the arrays.
C -----
      SUBROUTINE INTERP(X1,XN,H,N,Y,X,M,YOUT)
      IMPLICIT REAL*8 (A-H,O-Z)
      DIMENSION Y(N),D(10)
C
      FM=M+1
      J=(X-X1)/H-FM/2.D0+2.D0
      IF (X.LE.(X1+FM/2.D0*H)) THEN
        J=1
      END IF
      IF (X.GE.(XN-FM/2.D0*H)) THEN
        J=N-M
      END IF
      FJ=J
      X0=X1+(FJ-1.D0)*H
      Y0=Y(J)
      DO 10 I=1,M
        D(I)=Y(J+1)-Y(J)
        J=J+1
10  CONTINUE
      IF (M.GT.1) THEN
        DO 20 J=2,M
          DO 15 I=J,M
            K=M-I+J
            D(K)=D(K)-D(K-1)
15  CONTINUE
20  CONTINUE
      END IF
      S=(X-X0)/H
      YOUT=Y0
      FNUM=S
      DEN=1.D0
      DO 30 I=1,M
        FI=I
        YOUT=YOUT+FNUM/DEN*D(I)
        FNUM=FNUM*(S-FI)

```

```

      DEN=DEN*(FI+1.D0)
30  CONTINUE
      RETURN
      END

```

```

C -----
C FUNCTION ENN:
C - This function returns the value of n(rho) for a given rho.
C -----
      DOUBLE PRECISION FUNCTION ENN(RHO)
      IMPLICIT REAL*8 (A-H,O-Z)
      COMMON XARR(500),YARR(500),NUMVAL,IDEG,RLOWER,
      &      UPPER,XSHIFT
C
      CALL INTERP(RLOWER,UPPER,XSHIFT,NUMVAL,YARR,RHO,
      &      IDEG,YOUT)
      ENN=YOUT
      RETURN
      END

```

```

C -----
C Program MODEL:
C - This program models the Greenstein effect for the R-form branch lines of the
C CN(0,0) ultraviolet band. Different velocity profiles of the gas in the comet's coma are
C inserted into this program in order to see the resulting Greenstein effect.
C Written by Wayne Jaworski, September 1987.
C -----
C
C Variable Dictionary:
C
C - DOP      - the doppler shift for a given radial velocity;  $DOP = 1 + (v/c)$ .
C              Let  $\sigma =$  wavenumber of a line in doppler shifted reference
C              frame, let  $\sigma' =$  laboratory or theoretical wavenumber of a line.
C              Then,  $\sigma = \sigma' * DOP$ 
C - ELOVN    - L/N (radiance/column densities) -> this gives an indication of the
C              population in the upper N' state compared with the ground state N".
C - G        - constant of proportionality (eqn. 7, Aikman et. al. [hereafter ABT]
C              (1974))
C - NOLINE   - the number of R-branch lines to solve for (max = 30)
C - R        - the heliocentric distance of the comet (in a.u.)
C - RD       - the radial velocity of the comet (km/s)
C - RWAVE    - wavenumbers of R-form branch lines [R(1)-R(NOLINE)].
C - VLITE    - the velocity of light (km/s)
C - Y        - the distance from the comet nucleus in km of the current integration
C              point
C - YSTEP    - the step size in km across the coma
C - YUP      - the upper limit integration point from the nucleus in km
C -----

```

```

IMPLICIT REAL * 8 (A-H,O-Z)
REAL*8 LINES(30),RATIOS(200),JETSX(3000),JETSY(3000)
COMMON NOLINE

```

C First, read in all of the (x,y) coordinates corresponding to points located on a CN jet

```

DO 14 I=1,2795
  READ(15,*) JETSX(I),JETSY(I)
14 CONTINUE

```

C Next set all of the changeable parameters

```

YLOW=-1.85D5
Y=YLOW
YUP=1.86D5
YSTEP=3700.D0
NOLINE=30
G=3.701D-4
RD=26.37D0
R=1.40D0

VLITE=2.997293D5
R2=R*R

```

C Now solve the model for the Greenstein effect across the coma (from Y=YLOW km to
C YUP km)

```

J=0
30 CONTINUE
  J=J+1
  CALL SOLVE(R2,G,LINES,RD,VLITE,Y,JETSX,JETSY)
C  CALL NORMAL(LINES)
  RATIOS(J)=LINES(10)/LINES(13)
  Y=Y+YSTEP
  IF (Y.LE.YUP) GOTO 30

```

C Write out the R(9)/R(12) ratio to disk

```

WRITE(6,20)
DO 10 I=1,J
  WRITE(6,21) ((I-1)*YSTEP)+YLOW,RATIOS(I)
10 CONTINUE
20 FORMAT(' ',MODEL #9 :',',Distance from Nucleus ',
& (km)',5X,'R(9)/R(12)',/,26('*'),5X,10('*')//)
21 FORMAT(' ',8X,F10.1,10X,F10.4)

```

```

STOP
END

```

```

C -----
C Subroutine NORMAL:
C - This subroutine normalizes the line intensities to 100.
C -----
SUBROUTINE NORMAL(LINES)
IMPLICIT REAL*8 (A-H,O-Z)
REAL*8 LINES(30)
COMMON NOLINE

SUM=0.D0
DO 10 I=1,NOLINE
SUM=SUM+LINES(I)
10 CONTINUE
DO 20 I=1,NOLINE
LINES(I)=(LINES(I)/SUM)*1.0D2
20 CONTINUE
RETURN
END

C -----
C Subroutine SOLVE:
C - This subroutine returns the line intensities (not normalized) of the R-branch lines at
C the requested distance Y (in km) from the nucleus.
C -----
SUBROUTINE SOLVE(R2,G,LINES,RD,VLITE,Y,JETSX,JETSY)
IMPLICIT REAL*8 (A-H,O-Z)
REAL*8 LINES(30),LIMIT,F(700,30),TEMP(30),JETSX(3000),
& JETSY(3000)
INTEGER COUNT,ONJET
COMMON NOLINE

C
C First build table 'F' of Swings effect results at different distances X through coma. 'A' is
C the radius of the coma in km (200,000 km). 'DX' is the step size through the coma in
C km.
C
A=2.0D5
LIMIT=DSQRT(A*A-Y*Y)
X=-LIMIT
DX=900.D0
COUNT=0

9 CONTINUE
COUNT=COUNT+1
RHO=DSQRT(X*X+Y*Y)
CALL GETVEL(X,Y,A,V,COSXI,RHO,ONJET,JETSX,JETSY)
RADIAL=RD+V*COSXI
DOP=1.D0+RADIAL/VLITE
CALL SWINGS(DOP,R2,ELOVN,G,TEMP)
DO 10 I=1,NOLINE

C
C Note how density of CN through coma is used to weight the line intensities at a particular
C (x,y) coordinate

```

```

C
  IF (RHO.LE.731.5D0) THEN
    DENS=3.D0
  ELSE
    DENS=44406.757D0/(RHO**1.456)
  END IF
  IF (ONJET.GT.0) THEN
    DENS=DENS*500.D0/(IABS(ONJET-3)+1)
  END IF
  F(COUNT,I)=TEMP(I)*DENS
10  CONTINUE
    X=X+DX
  IF (X.LE.LIMIT) GOTO 9
C
C Now, integrate table of values in order to recover observed intensity profile of lines
C
  CALL SIMPS(F,COUNT,DX,LINES)
  RETURN
  END

```

```

C -----
C Subroutine GETVEL:
C - This subroutine determines the velocity profile to be modelled. Just change this
C subroutine to change the model!
C
C 'V' is the velocity of the coma gas particle (in km/s) relative to the nucleus of the comet.
C 'COSXI' determines the amount of 'V' contributing to the radial velocity of the particle
C w.r.t. the sun. 'EXTRA' is the velocity (km/s) to add to a gas particle if it lies on or near
C a gas jet. If (x,y) coordinate is on a jet then 'ONJET' returns a number >0 to the caller
C depending on how far away the point is from the jet. 'TOL' is the distance a particle can
C be from a jet and still be considered to be in that jet (in km).
C  $RHO \leq (JETSX^2 + JETSY^2)^{1/2}$ .
C -----

```

```

SUBROUTINE GETVEL(X,Y,A,V,COSXI,RHO,ONJET,JETSX,JETSY)
IMPLICIT REAL*8 (A-H,O-Z)
REAL*8 JETSX(3000),JETSY(3000)
INTEGER ONJET

```

C First determine the velocity 'V' of a gas particle

```

  V=1.D0
  ONJET=0
  TOL=RHO/15.D0
  CLOSE=999999.D0
  DO 100 I=1,2795
    DIST=DSQRT((X-JETSX(I))**2+(Y-JETSY(I))**2)
    IF ((DIST.LT.CLOSE) AND
& ((JETSX(I)**2+JETSY(I)**2).GE.RHO)) THEN
      CLOSE=DIST
    END IF
100 CONTINUE

```

```

IF (CLOSE.LE.TOL) THEN
  EXTRA=5.0D0/DEXP(CLOSE/TOL)
  V=V+EXTRA
  TEMP=(15.D0/EXTRA)-2.D0
  ONJET=INT(TEMP)
END IF

```

C Add solar wind effect (elastic collision effect) in determining 'COSXI'

```

SHOCK=15000.D0
IF (RHO.NE.0.D0) THEN
  BEND=DEXP(RHO/SHOCK)
  COSXI=(X+BEND)/RHO
ELSE
  COSXI=0.D0
END IF
RETURN
END

```

C -----

C Subroutine SIMPS:
C - This subroutine performs Simpson's rule integration of a function defined by a table
C of equispaced values.
C
C Parameters:
C
C F - array of values of the function
C N - number of points in table
C H - the uniform spacing between x values
C RESULT - estimate of the integral that is returned (ie. line intensities are returned [not
C normalized])
C -----

```

SUBROUTINE SIMPS(F,N,H,RESULT)
REAL*8 F(700,30),H,RESULT(30)
INTEGER N,NPANEL,NHALF,NBEGIN,NEND,I,J
COMMON NOLINE

```

C
C Check to see if number of panels is even. Number of panels is N-1
C

```

NPANEL=N-1
NHALF=NPANEL/2
NBEGIN=1
DO 10 I=1,NOLINE
  RESULT(I)=0.D0

```

10 CONTINUE
IF ((NPANEL-2*NHALF).NE.0)THEN

C
C Number of panels is odd. Use 3/8 rule on first three, 1/3 rule on rest
C

```

DO 20 I=1,NOLINE
  RESULT(I)=3.D0*H/8.D0*(F(1,I)+3.D0*F(2,I)+3.D0*

```

```

      &          F(3,I)+F(4,I))
20  CONTINUE
      NBEGIN=4
      IF (N.EQ.4) RETURN
      END IF
C
C Apply 1/3 rule - add in first, second and last values
C
      DO 30 I=1,NOLINE
        RESULT(I)=RESULT(I)+H/3.D0*(F(NBEGIN,I)+4.D0*
      &          F(NBEGIN+1,I)+F(N,I))
30  CONTINUE
      NBEGIN=NBEGIN+2
      IF (NBEGIN.EQ.N) RETURN
C
C The pattern after NBEGIN+2 is repetitive. Get NEND, the place to stop.
C
      NEND=N-2
      DO 40 I=NBEGIN,NEND,2
        DO 50 J=1,NOLINE
          RESULT(J)=RESULT(J)+H/3.D0*(2.D0*F(I,J)+4.D0*
      &          F(I+1,J))
50  CONTINUE
40  CONTINUE
      RETURN
      END
C -----
C Subroutine SWINGS:
C - This subroutine calculates the Swings effect by solving the necessary system of
C equations.
C
C Variable Dictionary:
C
C - RWAVE - see mainline dictionary.
C - ZZ - matrix of coefficients used in solving eqn.(8) of ABT (1974). The system to
C be solved is of the form AX=B, where the B's are all 0, the X's are the
C desired values of Xn",Xn"+1,etc. and the A's are the factors corresponding
C to Xn"-2,etc. from eqn.(8).
C ZZ is NOLINE x NOLINE in size. (initially all 0's)
C - ZU - correction term to solar radiation densities (U's) since the solar spectrum on
C disk lists intensities as seen from an observer at 1 a.u. away. ZU is
C proportional to 1/(square of heliocentric distance)
C - C1 - from eqn.(8)of ABT (1974). Coefficient of Xn"-2.
C  $C1 = ((N^2 * N^2 - N^2) / (4N^2 * N^2 - 8N^2 + 3)) * U_r(n^2 - 2)$ 
C - C2 - Coefficient of Xn". The terms of C2 are split up in the calculation into 3
C separate factors (F1,F2,and F3). So, C2 = -(F1+F2+F3)
C - C3 - Coefficient of Xn"+1.
C - C4 - Coefficient of Xn"+2. Note: ZZ looks like:
C          [ C3 C4 0 .. ]
C          [ C2 C3 C4 .. ]
C          [ 0 C2 C3 .. ]

```

```

C           [ C1 0  C2 .. ]
C           [ 0  C1  0 .. ] etc.
C - XN      - vector to be solved for, needed to calculate intensities (Yn's) using equation
C           (9) of ABT (1974).
C -----

```

```

SUBROUTINE SWINGS(DOP,R2,ELOVN,G,Y)
IMPLICIT REAL * 8 (A-H,O-Z)
COMMON NOLINE
DIMENSION ZZ(100,100),A(5,100),AL(3,100),IN(100),
& XN(100,1),Y(30),RWAVE(99),YNORM(99)
DATA ZZ/10000*0.D0/
DIMENSION C1(97),C2(99),C3(100),C4(99)

```

C Calculate wavenumbers of R(1) to R(NOLINE) lines.

```

DO 20 NP=1,NOLINE
  RWAVE(NP)=POLY(NP+1)
20 CONTINUE

```

C Now build the matrix of coefficients to use in solving for Xn's

```

ZU=(6.871D-4)/R2
ICOL = 0
DO 1 NROW=4,NOLINE+1
  N=NROW-1
  ICOL = ICOL + 1

```

C Doppler shift R(n"-2) line then get solar radiation density from disk corresponding to that
C wavenumber [Ur(n"-2)]

```

RNM2D=POLY(N-1)*DOP
Z=ZINTEN(RNM2D)
C1(NROW)=(N*N-N)/(3.D0-4.D0*N*(2.D0-N))*Z*ZU
ZZ(NROW,ICOL) = C1(NROW)
1 CONTINUE

ICOL = 0
DO 2 NROW=2,NOLINE+1
  N=NROW-1
  ICOL = ICOL + 1
  PND=POLY(-N)*DOP
  RND=POLY(N+1)*DOP
  ZP=ZINTEN(PND)
  ZR=ZINTEN(RND)
  F1=(N*N-N)/(4.D0*N*N-1.D0)*ZP*ZU
  F2=(2.D0+N*(3.D0+N))/(3.D0+4.D0*N*(2.D0+N))*ZR*ZU
  F3=(G*N**4)/(N+5.D-1)
  C2(NROW)=-(F1+F2+F3)
  ZZ(NROW,ICOL) = C2(NROW)
2 CONTINUE

```

```

ICOL = 0
DO 3 NROW=1,NOLINE+1
  N=NROW-1
  ICOL = ICOL + 1
  C3(NROW)=(G*(N+1.D0)**4)/(N+1.5D0)
  ZZ(NROW,ICOL) = C3(NROW)
3 CONTINUE

```

```

ICOL = 1
DO 4 NROW=1,NOLINE
  N=NROW-1
  ICOL = ICOL + 1
  PNP2D=POLY(-N-2)*DOP
  ZP2=ZINTEN(PNP2D)
  C4(NROW)=(2.D0+N*(3.D0+N))/(1.5D1+4.D0*N*(4.D0+N))
  & *ZP2*ZU
  ZZ(NROW,ICOL) = C4(NROW)
4 CONTINUE

```

C Now build Xn vector (mostly 0's) and solve system of equations

```

R0D=POLY(1)*DOP
ZR0=ZINTEN(R0D)
AK1=2.D0*ZR0*ZU/3.D0
AK3=-AK1
DO 99 I=1,NOLINE+1
  XN(I,1) = 0.D0
99 CONTINUE
XN(1,1) = AK1
XN(3,1) = AK3

```

C See NAG library documentation for the meaning of these following variables (used in C routines F01LBF and F04LDF)

```

N = NOLINE+1
M1 = 3
M2 = 1
IA = 5
IL = 3
IB = NOLINE+1

```

C Transfer band matrix from conventional storage as a full matrix into array A as required C by NAG routines

```

DO 40 J=1,N
  I1 = MAX0(J-M2,1)
  I2 = MIN0(J+M1,N)
  DO 88 I=I1,I2
    K = MIN0(M1-I+1,0) + J
    A(K,I) = ZZ(I,J)

```

```
88 CONTINUE
40 CONTINUE
```

C Use NAG library routines to solve the linear, homogeneous system of equations $Ax=B$.
C F01LBF decomposes the A matrix into 2 triangular matrices (required by F04LDF).

```
IFAIL = 1
CALL F01LBF(N,M1,M2,A,IA,AL,IL,IN,IV,IFAIL)
IF(IFAIL.NE.0)WRITE(6,*)IFAIL,IV
IF(IFAIL.NE.0)STOP 1
IR = 1
CALL F04LDF(N,M1,M2,IR,A,IA,AL,IL,IN,XN,IB,IFAIL)
IF(IFAIL.NE.0)WRITE(6,*)IFAIL
IF(IFAIL.NE.0)STOP 2
```

C Add up Xn's

```
XSUM=1.D0
DO 60 I=1,NOLINE+1
  XSUM=XSUM+XN(I,1)
60 CONTINUE
```

C Calculate Y1 separately

```
R0=POLY(1)
R0D=R0*DOP
UR0=ZINTEN(R0D)*ZU
BA1=BOVA(R0,2.D0)
P2=POLY(-2)
P2D=P2*DOP
UP2=ZINTEN(P2D)*ZU
BA2=BOVA(P2,1.D0)
Y(1)=UR0*BA1+UP2*XN(2,1)*BA2*4.D-1
```

C Calculate Eqn.(9) of ABT (1974)

```
DO 50 N=2,NOLINE
  FN1=N/(2.D0*N-1.D0)
  RNM1=POLY(N)
  RNM1D=RNM1*DOP
  UR=ZINTEN(RNM1D)*ZU
  BA1=BOVA(RNM1,1.D0)
  FN2=(N+1.D0)/(2.D0*N+3.D0)
  PNP1=POLY(-N-1)
  PNP1D=PNP1*DOP
  UP=ZINTEN(PNP1D)*ZU
  BA2=BOVA(PNP1,1.D0)
  Y(N)=FN1*UR*XN(N-1,1)*BA1+FN2*UP*XN(N+1,1)*BA2
50 CONTINUE
```

```
ELOVN=7.3279D-13*YSUM/XSUM
```

RETURN
END

C-----
C Function POLY:
C - This function returns the wavenumber for the passed m value.
C
C - Poly = ((A5 M + A4)M + A3)M + A2)M + A1
C = a1 + a2*m + a3*m^2 + a4*m^3 + a5*m^4
C
C - Recall that you can fit both P & R branches to the Fortrat parabola (band origin at
C m=0). For CN (0,0) band, get :
C
C sigma = sigma(0) + (Bo'+Bo'')m + (Bo'-Bo''-Do'+Do'')m*m - 2(Do'+Do'')m**3 -
C (Do'-Do'')m**4
C
C Where : (Variable dictionary)
C - POLY = sigma (wavenumber of line)
C - A(1) = sigma(0) (band origin = 25,797.839 [1/cm])
C - A(2) = (Bo'+Bo'')
C - A(3) = (Bo'-Bo''-Do'+Do'')
C - A(4) = -2(Do'+Do'')
C - A(5) = -(Do'-Do'')
C
C Rotational constants and centrifugal distortion constants for CN: (B-X transition)
C (Taken from Engleman, 1974)
C
C Bo' = 1.95874 [1/cm]
C Bo'' = 1.89113 [1/cm]
C Do' = 6.58d-6 [1/cm]
C Do'' = 6.41d-6 [1/cm]
C-----

REAL FUNCTION POLY*8(M)
IMPLICIT REAL * 8 (A-H,O-Z)
DIMENSION A(5)

A(1)=2.5797839D4
A(2)=3.84987D0
A(3)=6.760983D-2
A(4)=-2.598D-5
A(5)=-1.7D-7

POLY=A(5)
DO 7 K=1,4
POLY=POLY*M+A(5-K)

7 CONTINUE
RETURN
END

C -----
 C Function BOVA:
 C - This function returns B/A. The Einstein B coefficient for the (0,0) band of the CN
 C violet system is related to the Einstein A coefficient by:
 C $B/A = (\text{wavelength}^{**5})/(8*\text{pi}*h*c)$
 C -----

```
REAL FUNCTION BOVA*8(WAVNUM,STWTS)
BOVA=2.003D13*STWTS/(WAVNUM**5)
RETURN
END
```

C -----
 C Function ZINTEN:
 C - This function accesses the digital solar spectrum and returns the required intensity at
 C the desired wavenumber. Note that DATA statements are executed only the 1st time
 C through the subroutine!
 C -----

```
REAL FUNCTION ZINTEN*8(X)
REAL*8 X,XFIRST,XINCR,XLAST
REAL*8 XLEFT,XRIGHT,YLEFT,YRIGHT,DFLOAT
INTEGER*2 INTEN(12288)
LOGICAL FIRST
DATA FIRST/.TRUE./
DATA XFIRST/25625.968520D0/
DATA XINCR/.029792095D0/
DATA XLAST/25992.023989D0/
```

C The first time through this subroutine read the solar spectrum data into the array
 C 'INTEN'

```
IF (FIRST) THEN
  FIRST=.FALSE.
  JSTART=1
  DO 30 I=1,3
    JSTOP=JSTART+4095
    READ(1,20)(INTEN(J),J=JSTART,JSTOP)
20  FORMAT(32(128A2))
    JSTART=JSTART+4096
30  CONTINUE
  ENDIF

IF (X.GE.XFIRST) THEN
  IF (X.GT.XLAST) THEN
710  WRITE(6,710)X,XLAST
    &  FORMAT(' X VALUE ',F12.6,' IS GREATER THAN',
    &  ' LARGEST X VALUE ',F12.6)
    ZINTEN=-1.D0
  ELSE
    IP=IFIX(SNGL((X-XFIRST)/XINCR))
    XLEFT=XFIRST+DFLOAT(IP)*XINCR
```

```
    XRIGHT=XLEFT+XINCR
    IP=IP+1
    IVAL=INTEN(IP)
    YLEFT=DFLOAT(IVAL)
    IVAL=INTEN(IP+1)
    YRIGHT=DFLOAT(IVAL)
    ZINTEN=((X-XLEFT)/XINCR)*(YRIGHT-YLEFT)+YLEFT
ENDIF
ELSE
    WRITE(6,610)X,XFIRST
610  FORMAT(' X VALUE ',F12.6,' IS LESS THAN SMALLEST ',
&        'X VALUE ',F12.6)
    ZINTEN=-1.D0
ENDIF
RETURN
END
```

VITA

Surname: Jaworski **Given Names:** Wayne Anthony

Place of Birth: Winnipeg, MB **Date of Birth:** February 18, 1963

Educational Institutions Attended, with Dates of Entering and Leaving:

University of Manitoba, Winnipeg 1981 to 1985

University of Victoria, BC 1985 to 1988

Degrees, Diplomas, Etc., Awarded, with Dates and Names of Institutions:

B.Sc. (Major) 1985 University of Manitoba

Honours and Awards:

University of Manitoba Dean's Honor Roll, 1981/82, 1983/84, 1984/85

N.S.E.R.C. Summer Research Award, 1983, 1984, 1985

N.S.E.R.C. Post Graduate Scholarship, 1985-87

Publications:

Tatum, J.B., Jaworski, W.A. (1987) *JQSRT*, **38**, 319, "A Solution of Abel's Equation "

PARTIAL COPYRIGHT LICENSE

I hereby grant the right to lend my thesis or dissertation (the title of which is shown below) to users of the University of Victoria Library, and to make single copies only for such users or in response to a request of any other university, or similar institution, on its behalf or for one of its users. I further agree that permission for extensive copying of this thesis for scholarly purposes may be granted by me or a member of the University designated by me. It is understood that copying or publication of this thesis for financial gain shall not be allowed without my written permission.

Title of Thesis:

Analysis of the Swings Effect and
Greenstein Effect in Comet P/Halley

Author:


Wayne Anthony Jaworski

FEBRUARY 26 / 1988